

NOTE TO USERS

This reproduction is the best copy available.

UMI



DISSERTATION

ACTIN DYNAMICS IN SILICO, IN WAVES, AND IN RODS

Submitted by

Chi W. Pak

Graduate Degree Program in Cell and Molecular Biology

In partial fulfillment of the requirements

For the Degree of Doctor of Philosophy

Colorado State University

Fort Collins, CO

Fall 2009

UMI Number: 3401028

All rights reserved

INFORMATION TO ALL USERS

The quality of this reproduction is dependent upon the quality of the copy submitted.

In the unlikely event that the author did not send a complete manuscript and there are missing pages, these will be noted. Also, if material had to be removed, a note will indicate the deletion.



UMI 3401028

Copyright 2010 by ProQuest LLC.

All rights reserved. This edition of the work is protected against unauthorized copying under Title 17, United States Code.



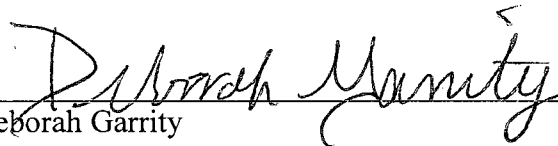
ProQuest LLC
789 East Eisenhower Parkway
P.O. Box 1346
Ann Arbor, MI 48106-1346

COLORADO STATE UNIVERSITY

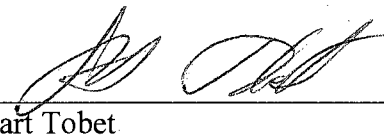
August 24, 2009

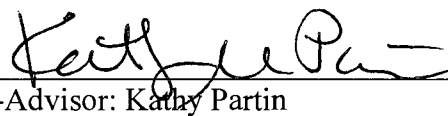
WE HEREBY RECOMMEND THAT THE DISSERTATION PREPARED
UNDER OUR SUPERVISION BY CHI W. PAK ENTITLED ACTIN DYNAMICS IN
SILICO, IN WAVES, AND IN RODS BE ACCEPTED AS FULFILLING IN PART
THE REQUIREMENTS FOR THE DEGREE OF DOCTOR OF PHILOSOPHY.

Committee on Graduate Work

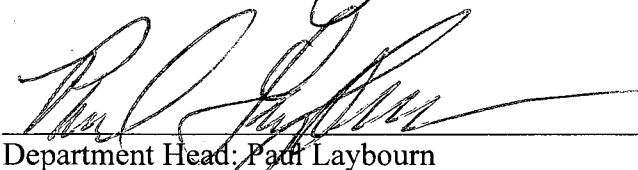

Deborah Garrity


Robert Handa


Stuart Tobet


Co-Advisor: Kathy Partin


Advisor: James Bamberg


Department Head: Paul Laybourn

ABSTRACT OF DISSERTATION

ACTIN DYNAMICS IN SILICO, IN WAVES, AND IN RODS

The current paradigm of actin dynamics and superorganization has advanced in the past decade from emerging technologies and perspectives, which include the discovery of actin nucleators, real time imaging of the dynamics of single filaments *in vitro*, and single molecule imaging of actin superstructures *in vivo*. These advances have influenced each of our studies on multiple levels, sometimes directly. A novel analysis of single actin filament dynamics revealed faster than expected dynamics during treadmilling but not during bulk polymerization. Using an exact stochastic simulation, we investigated whether filament-annealing and –fragmentation might account for faster than expected dynamics; their influence on actin dynamics had not been investigated before in a comprehensive model. Results from our work demonstrated that filament-annealing and –fragmentation alone cannot account for faster than expected dynamics during treadmilling. Thus, strictly through computational modeling, we are able to investigate various hypothetical models and offer insights into a process that cannot be achieved by experimentation.

A concept that has also gained support during the past decade has been the self-organizing nature of actin, which was demonstrated by the *Listeria* actin-comet-tail reconstitution assay. We have proposed that this is a fundamental property of all actin superstructures, whether they are assembled *in vitro* or *in vivo* or whether they are involved in development or disease. The concept of actin’s self-organization has influenced our study of neuronal waves, which are growth cone-like structures that travel

along neurites and which were hypothesized to transport actin to growth cones and support neuritogenesis. Using diffusional analysis, we were able to demonstrate that neuronal waves transport actin. Neuronal waves provide a unique mechanism for transporting actin in that the delivery of actin is dependent upon actin itself and its dynamics. In disease states, the self-organization of actin is often changed but not disrupted, sometimes resulting in the formation of orderly-structured aggregates of cofilin and actin known as cofilin-actin rods (or rods). Using glutamate excitotoxicity as a model system for the cofilin pathology observed in Alzheimer disease (AD), we have determined signaling mechanisms for cofilin-actin rod induction, which in young rat hippocampal neurons require AMPA receptors and are calcium-independent. In addition, cofilin-actin rod interactions with microtubule associated proteins, and associated changes to the microtubule cytoskeleton were studied for its potential relevance to the pathology of AD. Our results suggest that disruptions to the normal organization of actin and microtubules might underlie several pathological hallmarks of early AD.

Chi Won Pak
Graduate Program in Cell and Molecular Biology
Colorado State University
Fort Collins, CO 80523
Fall 2009

Acknowledgements

It takes a village to raise a graduate student.

There are a great many people I am indebted to, whom have in any capacity contributed to my development as a scientist and person. First and foremost, I would like to thank my parents, whom have sacrificed immeasurably so that I might achieve in my life what I only hope will make them proud. I am also grateful to my older brother, whom without, I would have been unable to complete my studies. For their support, I am grateful, proud and humbled.

Secondly, I would like to thank my advisor, Jim Bamburg, and his wife, Laurie Minamide, for their unfailing support of me even as I toiled at my research for many despairing years. I hope that I might exhibit a fraction of their integrity, thoughtfulness, and charity if ever I am in the same position.

I would also like to thank members of my committee, whom though not always in agreement with me, were always on my side, with my best interests in mind. Their patience is unheralded and their support appreciated.

I would also like to thank past and present members of the Bamburg lab, whom have shaped me in the most direct ways through their daily influence. These include (in no particular order): Alisa Shaw, O'Neil Wiggan, Rich Davis, Shay Perea-Boettcher, Joe Fass, Patrick Sarmiere, Lubna Tahtamouni, Kevin Flynn, Mike Maloney, Janel Funk, Hui Hung and countless others. Like children of war, we are forever bonded by our times shared together.

There are also many other people I have met throughout my graduate studies, through both fortunate and unfortunate circumstances, whom I would also like to acknowledge. These are (in no particular order): Judy Mufti, Erik Peterson, Albert Gonzales, Scott Bayer, Matt Stratton, Kristen Osterlund, Kyle Grode, Matthew Bedoukian, Kris Hite, Lukas Kapitein, Bechara Kachar, Douglas Weibel, Ineka Whiteman, Bonnie Marsick, and Joseph Burns.

To the countless others that deserve my thanks but were not mentioned, my deepest apologies.

TABLE OF CONTENTS

| | |
|---|------|
| Signature Page | ii |
| Abstract of Dissertation | iii |
| Acknowledgements | v |
| Table of Contents | vii |
| List of Figures | x |
| List of Abbreviations | xiii |
| | |
| Chapter One: Actin dynamics and superstructures | 1 |
| Self-Organization in Living Systems | 1 |
| Actin Dynamics In Vitro | 2 |
| Actin Dynamics In Vivo | 9 |
| Actin Superstructures | 15 |
| The States of Actin – Distinct Superstructures | 18 |
| | |
| Chapter Two: Stochastic simulation of actin dynamics reveals the role of annealing and fragmentation | 25 |
| Preface and Acknowledgement | 25 |
| A Primer on 1-Dimensional Diffusion | 26 |
| Abstract | 30 |
| Introduction | 31 |
| Methods | 35 |
| Results | 45 |
| Simulations of filament populations reveal minute details of actin dynamics | 45 |
| Higher fragmentation rates result in faster polymerization kinetics | 51 |
| Fragmentation and annealing events affect neither nucleotide profiles within filaments, nor barbed ends length excursions | 52 |
| Simulations yield high diffusivities only if large length changes and higher fragmentation rates are allowed | 58 |
| Length diffusivity dependence on actin concentration | 63 |
| Discussion | 64 |
| | |
| Chapter Three: Growth cone-like waves transport actin and promote axonogenesis and neurite branching | 73 |
| Preface and Acknowledgement | 73 |
| Abstract | 74 |
| Introduction | 75 |
| Materials and Methods | 77 |
| Neuronal Cell Culture | 77 |
| Adenoviral Infections | 77 |
| Immunocytochemistry | 78 |

| | |
|---|---------|
| Organotypic hippocampal slice culture | 79 |
| Live-cell microscopy | 79 |
| Morphological analysis of growth cones and waves | 81 |
| Results | 82 |
| Molecular composition and dynamics of waves | 82 |
| Wave frequency and impact on growth cones during axonogenesis | 85 |
| Waves and branching | 90 |
| Cofilin modulates the prevalence of waves | 91 |
| Inhibiting myosin or growth on laminin enhances axonogenesis, branching and waves | 91 |
| Waves increase growth cone size and dynamics | 98 |
| Waves transport actin | 101 |
| Waves occur in neurons within hippocampal slices | 107 |
| Discussion | 111 |
| What are waves? | 111 |
| Waves influence axon development | 113 |
| Waves and branching | 114 |
| Waves increase growth cone size and motility | 115 |
| Are waves a transport mechanism? | 116 |
| Waves occur in brain slices | 119 |
| Chapter Four: Glutamate-induced cofilin-actin rod formation requires AMPARs and is associated with a disruption of trafficking of APP-YFP-containing vesicles | 120 |
| Preface and Acknowledgements | 120 |
| Abstract | 120 |
| Introduction | 121 |
| Materials and Methods | 127 |
| Cell culture | 127 |
| Drug treatments | 128 |
| Immunofluorescence | 129 |
| Quantification of cofilin-actin rod formation | 130 |
| Transfections | 131 |
| Adenoviral infections | 132 |
| Ca ²⁺ imaging and analysis | 133 |
| APP-YFP imaging and analysis | 133 |
| Results | 133 |
| Glutamate induces cofilin-rods through dephosphorylation | 133 |
| Glutamate-induced cofilin-rod formation requires AMPA receptors | 134 |
| Ca ²⁺ and the Ca ²⁺ -dependent proteins, calcineurin or calpain, are not essential for AMPA-induced cofilin-rod formation | 140 |
| HMW MAP2s weakly co-localize with AMPA-induced rods | 143 |
| R21Q cofilin mutant exhibits reduced rod formation and actin | 144 |

| | |
|---|-----|
| binding | |
| R21Q cofilin mutant incorporates into rods formed from endogenous cofilin but forms less spontaneous rods induced by overexpression than WT cofilin | 147 |
| Neither WT MAP2c nor its phosphorylation mutants co-localize with rods in ATP-depleted A431 cells | 152 |
| The presence of cofilin-actin rods is associated with a loss of trafficking of APP-YFP-containing vesicles | 153 |
| The reversal of AMPA-induced rods is associated with the recovery of trafficking of APP-YFP-containing vesicles | 159 |
| AMPA induces the formation of rod-shaped cofilin aggregates in the CA3 region of organotypic hippocampal slices | 159 |
| Discussion | 162 |
| Chapter Five: General Discussion and Future Directions | 167 |
| Discussion | 167 |
| Future Directions | 169 |
| Reference List | 172 |

LIST OF FIGURES

| | | |
|-------------|---|-----|
| Figure 1.1 | General reaction-equations for actin polymerization | 4 |
| Figure 1.2 | Steady-state actin dynamics | 8 |
| Figure 1.3 | Distinct mechanisms of actin nucleators | 12 |
| Figure 1.4 | The geometry of superstructure strata is determined by the organizational plane of actin nucleators | 20 |
| Figure 1.5 | Distinct but spatially overlapping actin superstructures of lamella and lamellipodia | 24 |
| Figure 2.1 | Random frog-hopping in 1-dimension | 28 |
| Figure 2.2 | Reactions of actin dynamics implemented in our simulation | 37 |
| Figure 2.3 | Validation of annealing and fragmentation versus published experimental data | 42 |
| Figure 2.4 | Polymerization kinetics modeled using stochastic simulation | 47 |
| Figure 2.5 | Steady state length distributions of simulated actin filaments | 50 |
| Figure 2.6 | Simulated polymerization curves for various fragmentation rates | 54 |
| Figure 2.7 | Nucleotide states of simulated actin filaments at steady-state | 57 |
| Figure 2.8 | Lengths of excursions (contiguous loss or gain of subunits) at the barbed ends of filaments | 60 |
| Figure 2.9 | Length diffusivities calculated from simulations using various random-fragmentation rates | 62 |
| Figure 2.10 | Length diffusivity versus free actin concentration | 66 |
| Figure 2.11 | Effects of assuming instantaneous nucleotide exchange on G-actin monomers | 70 |
| Figure 3.1 | Waves have growth cone-like characteristics and propagate along the lengths of neurites | 84 |
| Figure 3.2 | Proteins associated with axon growth localize to waves | 87 |
| Figure 3.3 | Waves are associated with axonogenesis | 89 |
| Figure 3.4 | Cofilin activity may be involved in wave propagation | 93 |
| Figure 3.5 | Inhibition of myosin II enhances axonogenesis, neurite branching and increases the prevalence of wave-like structures | 95 |
| Figure 3.6 | Inhibition of myosin II influences wave dynamics | 97 |
| Figure 3.7 | Waves increase growth cone size and dynamics | 100 |
| Figure 3.8 | Waves transport actin | 103 |
| Figure 3.9 | Fluorescence loss from photo-converted Dendra-Actin suggests that actin diffuses rapidly in non-wave regions of the neurite shaft but remains associated with waves for longer times | 106 |
| Figure 3.10 | Waves occur in Thy1-YFP labeled neurons in hippocampal slices | 110 |
| Figure 4.1 | Glutamate excitotoxicity induce cofilin-actin rods | 136 |
| Figure 4.2 | Glutamate-induced rod formation is AMPAR-dependent | 139 |
| Figure 4.3 | Ca ²⁺ or the Ca ²⁺ -dependent proteins, calcineurin or calpain, are not essential for AMPA-induced rod formation | 142 |

| | | |
|-------------|---|-----|
| Figure 4.4 | Heavy molecular-weight (HMW) isoforms of MAP2 weakly co-localize with rods | 146 |
| Figure 4.5 | The R21Q cofilin mutant exhibits reduced actin binding and rod formation | 149 |
| Figure 4.6 | The R21Q cofilin mutant incorporates into endogenous cofilin-actin rods but forms less spontaneous rods than WT-cofilin | 151 |
| Figure 4.7 | Neither WT MAP2c nor its phosphorylation-mutants co-localize with rods in ATP depleted A431 cells | 155 |
| Figure 4.8 | The presence of cofilin-actin rods is associated with a loss of trafficking of APP-YFP-containing vesicles | 158 |
| Figure 4.9 | Reversal of AMPA-induced cofilin-rods is associated with the recovery of APP-YFP-containing vesicle transport | 161 |
| Figure 4.10 | AMPA treatment induces rods in the CA3 region of rat hippocampal slices | 164 |

LIST OF TABLES

| | | |
|-----------|---|----|
| Table 2.1 | Rate constants and reactions used in our simulation | 40 |
|-----------|---|----|

TABLE OF ABBREVIATIONS

| | |
|---------------------------|---|
| 1-D | 1-dimensional |
| 12E8 | monoclonal antibody that recognize phospho-epitopes of tau |
| A β ₁₋₄₂ | 42 amino acid amyloid beta peptide |
| AD | Alzheimer disease |
| ADF | actin depolymerizing factor |
| ADP | adenosine diphosphate |
| ADP·P _i | adenosine diphosphate non-covalently bound to inorganic phosphate |
| ALLN | Ac-Leu-Leu-Nle-H |
| AMPA | α -amino-3-hydroxy-5-methyl-4-isoxazolepropionic acid |
| AP5 | (2R)-amino-5-phosphonovaleric acid |
| ApoE | apolipoprotein E |
| APP | amyloid precursor protein |
| Arp2/3 | Actin related protein 2/3 |
| ATP | adenosine triphosphate |
| CA | Cornu Ammonis |
| CAMKII | calcium/calmodulin dependent protein kinase II |
| CCD | charge coupled device |
| Cdk | cyclin dependent kinase |
| CRMP2 | collapsin response mediator protein |
| CsA | cyclosporin A |
| D | diffusion coefficient |
| DHPG | (S)-3,5-Dihydroxyphenylglycine |
| DIC | differential interference contrast |
| DMSO | dimethylsulfoxide |
| DNA | deoxyribonucleic acid |
| DNQX | 6,7-dinitroquinoxaline-2,3-dione |
| DS | Down syndrome |
| EB1 | microtubule end-binding protein |
| EGTA | ethylene glycol tetraacetic acid |
| EM-CCD | electron multiplying charge coupled device |
| ERM | ezrin/radixin/moesin |
| F-actin | filamentous actin |
| FKBP | FK506 binding protein |
| FSM | fluorescent speckle microscopy |
| FTD | frontotemporal dementia |
| G-actin | globular actin |
| GAP43 | growth associated protein 43 |
| GFP | green fluorescent protein |
| GSK | glycogen synthase kinase |
| HEK | human embryonic kidney |
| HMW | high molecular weight or heavy molecular weight |
| JMY | junction mediating and regulatory protein |
| JNK | Jun NH ₂ -terminal kinase |
| LIM | lin11, isl-1, and mec-3 |

| | |
|------------------|---|
| LMW | low molecular weight |
| LTD | long term depression |
| LTP | long term potentiation |
| K_D | dissociation constant |
| MAP | microtubule associated protein |
| MCPG | α -methyl-4-carboxyphenylglycine |
| mDia | mammalian diaphanous |
| mGluR | metabotropic glutamate receptor |
| mRFP | monomeric red fluorescent protein |
| MyoIB | myosin IB |
| NA | numerical aperture |
| NFT | neurofibrillary tangle |
| NMDA | N-methyl-D-aspartate |
| NMR | nuclear magnetic resonance |
| NLS | nuclear localization signal |
| OG | Oregon Green |
| paGFP | photoactivatable green fluorescent protein |
| pcDendra | green-to-red photoconvertible Dendra fluorescent protein |
| PIP ₂ | phosphatidyl inositol 4,5-bisphosphate |
| PrPc | cellular prion protein |
| RNA | ribonucleic acid |
| RT | room temperature |
| SDS-PAGE | sodium dodecyl sulfate polyacrylamide gel electrophoresis |
| skTM | skeletal muscle tropomyosin |
| Thy1 | thymocyte differentiation antigen 1 |
| TIRF | total internal reflection microscopy |
| TI-VAMP | tetanus-insensitive vesicle-associated membrane protein |
| TMR | tetramethylrhodamine |
| UV | ultraviolet |
| VASP | vasodilator stimulated phosphoprotein |
| WASP | Wiskott-Aldrich syndrome protein |
| WAVE | WASP family verprolin homologous protein |
| WT | wild type |
| YFP | yellow fluorescent protein |

Chapter 1

Actin Dynamics and Superstructures

Preface and Acknowledgements

Portions of this chapter have been adapted from a manuscript published in Nature Reviews: Neuroscience (Pak *et al.*, 2008). The order and list of authors include: Chi W. Pak (CWP), Kevin C. Flynn (KCF), and James R. Bamberg (JRB). The manuscript was written by CWP and JRB and figures were contributed by CWP and KCF.

Self-Organization in Living Systems

Living systems are dynamically self-organizing, requiring the assembly of higher-order complexes from the basic building blocks of life: DNA, RNA, protein, and lipids. Some of these nano-scale complexes are merely structural assemblies (nano-structures), like scaffolding for a building; whereas, others are bona fide machines (nano-machines), able to spin, clamp, pinch, push or pull at the nanometer scale. For these nano-assemblies, how their constituent proteins are organized is as paramount to their function as is their dynamics, the *raison d'etre* to the saying: *form follows function*. For this reason, researchers have sought to study these complexes in an environment freed from the complexities of the cell (cell-free). Some of the first biological nano-machines to be studied in this manner were the cytoskeletal proteins, which include actin, intermediate filaments, and microtubules. The cytoskeletal proteins are capable of self-organizing into individual filaments, able to reach lengths sometimes 20,000 times their diameter, as well as organizing into higher-order assemblies involving interactions between multiple

individual filaments. As higher-order assemblies, the cytoskeletal proteins can function both as a nano-scaffold and as a nano-machine.

The conflation of actin as a scaffold and machine permit its broad involvement in diverse cell functions including cell adhesion and motility (Le Clainche and Carlier, 2008), cytokinesis (Barr and Gruneberg, 2007), transcriptional regulation (Hofmann, 2009), endocytosis (Girao *et al.*, 2008), intracellular trafficking (Lanzetti, 2007), and the formation of specialized cellular structures such as microvilli. Bacterial and viral exploitation of actin for infection (Theriot, 1995), propagation (Theriot, 1995), and motility in host cells (Gouin *et al.*, 2005; Carlier *et al.*, 2003; Cudmore *et al.*, 1997) also underscores its near-ubiquitous functions. An understanding of how actin can participate in these diverse functions begins with an understanding of its assembly as the mantra above suggests. Therefore, we will begin by discussing how actin structures are generated, first as filaments and then as higher-order assemblies.

Actin Dynamics In Vitro

Actin is a 43 kD protein, which can spontaneously self-assemble into polarized bi-helical filament-polymers *in vitro* (Pollard, 1986). Actin self-assembly is induced optimally by physiological salt concentrations (~140 mM); at salt concentrations below about 5 mM, actin remains monomeric (Pollard, 1986). At its simplest, actin's self-assembly can be described by the following reactions in Figure 1.1.

These reaction-equations describe actin's assembly into higher-order polymers (filaments) of different subunit-numbers ((1), dimer; (2), trimer; etc). In general, these

Figure 1.1. General Reaction-Equations for Actin Polymerization.

Equation (1). Dimer formation. Thermodynamically, monomeric actin is highly favored.

Equation (2). Trimer formation (nucleation). Dimeric actin is highly favored thermodynamically.

Equation (3). Tetramer formation. The kinetics of subunit addition and loss are nearly equal, although this ultimately depends on the free actin-monomer concentration.

Equation (4). Generalized reaction for subunit addition and loss to an actin polymer containing N subunits.

Equation (5). Once an actin filament reaches subunit number > 3 , subunit addition and loss (or filament end-dynamics) are described by the same kinetics.



reactions can be summarized by equation (4), which states that addition of an actin subunit, A, to an actin filament of N subunits, NA , results in a filament of $(N+1)$ subunits, $(N+1)A$. Though reaction-equation (4) can capture the qualitative nature of actin assembly, differences in the quantitative aspect of these reactions give ‘shape’ to the kinetics of actin polymerization.

Actin polymerization can be divided into three phases: lag, growth, and steady-state (Pollard, 1986). The lag phase occurs because the formation of an actin trimer, which functions as a seed or “nucleus” for polymer growth, is thermodynamically unfavorable (Pollard, 1986). The K_D for dimer and trimer-formation, reaction (1) and (2) respectively, are 4.56 M and 596 μM . To emphasize the relative impotence of actin nucleation, for an initial monomer-actin concentration of 1 μM , 187 pM of trimers are formed (~ 1 trimer for every 10,000 monomers present). However, once a nucleus is formed, actin subunits may assemble to either end of the nascent filament much more favorably, with kinetics described in reaction (4).

It should be noted, that after a filament reaches a threshold subunit-number >3 (a nucleus), its assembly/disassembly kinetics remains the same. During this phase, *filament-number* not *filament-subunit-number* determines the rate of polymer-assembly. Thus, subunit-number may be disregarded and the filament may be treated as a single species as in equation (5).

Also, although actin subunits incorporate on to either end of the filament at a rate that is dependent on the monomeric actin concentration, the rates of growth at either end of the filament are different. These differences exist in part because of inherent asymmetry, or polarity, of the filament ends. Initially based on a ‘string of arrowheads’

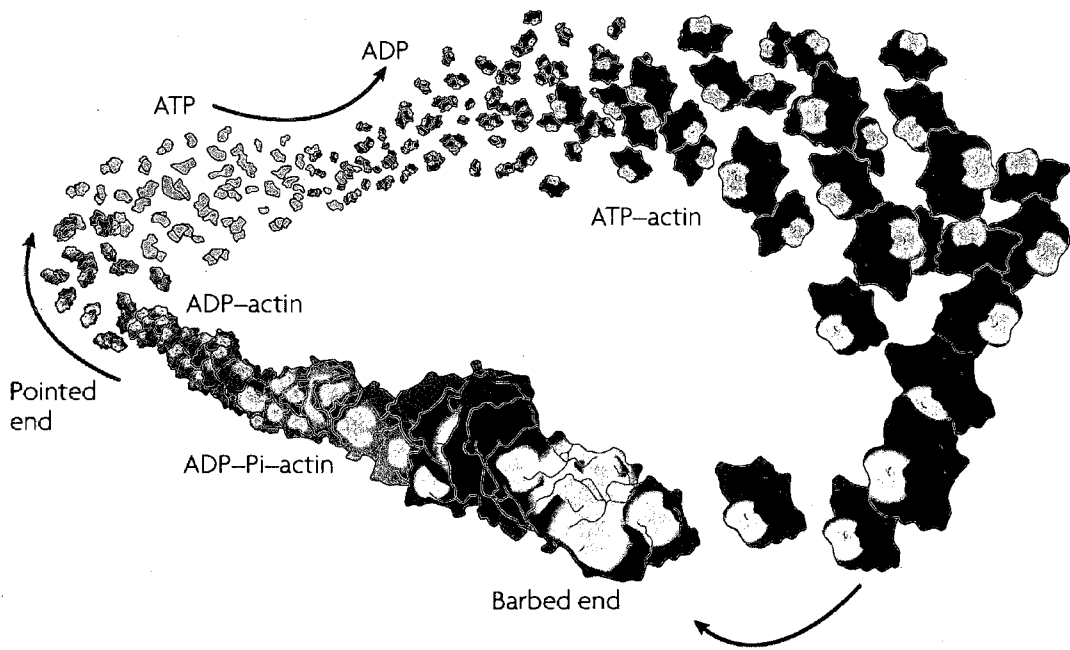
decoration pattern of actin filaments obtained with proteolytic fragments of myosin, the rapidly growing end was named the barbed end and the slower-growing end as the pointed end (Pollard and Mooseker, 1981). However, structural asymmetry is only one reason for the polarization of the filament. The hydrolysis of ATP within actin filaments also contributes.

Actin subunits, both as monomers and within filaments, are non-covalently associated with an adenine nucleotide to form a nucleotide-actin complex (Figure 1.2). *In vitro*, ATP-actin complexes are preferentially added to the barbed end of actin filaments, a process which is even more heavily favored in cells (Engel *et al.*, 1977). Rapidly after subunit incorporation, the non-covalently bound ATP is hydrolysed into ADP·P_i whereas subsequent release of the γ -P_i occurs much more slowly (Carlier, 1990). ATP hydrolysis occurs on average ~1-2 seconds after incorporation. γ -P_i release occurs on average ~350 seconds after hydrolysis. Practically, however, both processes occur stochastically for each subunit. Thus, even when the monomer pool initially consists only of ATP-actin complexes, an actin filament can eventually consist of three types of actin-nucleotide complexes: ATP-actin, ADP·P_i-actin, and ADP-actin (Figure 1.2).

As the mass of actin polymers grows and the mass of actin monomers shrinks, growth of the filaments begin to slow and reaches steady-state. By definition, the average length of all filaments remains constant during steady-state. However, even during steady-state, true equilibrium is never reached because actin subunit addition and loss can still occur, resulting in a phenomenon known as treadmilling (Cleveland, 1982; Neuhaus *et al.*, 1983). Thus, the lengths of individual filaments may still change. Fundamentally, treadmilling occurs because the two ends of an actin filament maintain different minimal

Figure 1.2. Steady-state actin dynamics.

Actin subunits, whether in filaments or as a monomer, are non-covalently bound to an adenine nucleotide. Free ATP-actin preferentially adds on to the barbed end of actin filaments at steady-state. After subunit incorporation, ATP undergoes rapid γ -P_i hydrolysis, resulting in ADP·P_i-actin complexes. With slower kinetics, the γ -P_i is subsequently released, resulting in ADP-actin complexes enriched near the pointed end of actin filaments. ADP-actin is lost from the filament at the pointed end and is recharged to ATP-actin through nucleotide exchange with free ATP. At steady-state, balance of subunit addition and loss results in no net change in actin filament length.



monomer concentrations for assembly, which are referred to as the ‘critical’ concentrations (Wegner, 1982). When the free actin monomer concentration lies intermediate to the two different critical concentrations, net assembly occurs at the barbed end and net disassembly occurs at the pointed end, resulting in the apparent movement or ‘treadmilling’ of individual subunits through a filament of relatively constant length.

Though the basic processes of *in vitro* actin polymerization provide a template for discussing actin dynamics within cells, the reality is that *in vivo* actin dynamics is to *in vitro* actin dynamics what chess is to checkers. The nearly 150 distinct actin-binding proteins that have been identified *in vivo* impart degrees of subtlety and complexity to the process of generating and maintaining actin structures (De La Cruz, 2001). In the next section, we will discuss their influence on actin dynamics.

Actin Dynamics *In Vivo*

Though actin binding proteins are capable of modulating any and all of the basic processes of *in vitro* actin polymerization discussed above, for the purpose of our discussion, only six different functional categories of actin-binding proteins will be mentioned: monomer-binding or filament-capping proteins, nucleating proteins (nucleators), tethering proteins, cross-linking proteins, and remodeling proteins.

Monomer-binding proteins. Most monomer-binding proteins limit actin assembly *in vivo*; otherwise, actin filaments would form un-regulated throughout the cell. As their name suggests, monomer-binding proteins, such as thymosin- β or calbindin, sequester and handcuff actin monomers from spontaneously assembling into filaments (Paunola *et*

al., 2002). However, it should be noted that some monomer-binding proteins, instead of limiting actin assembly, actually promote actin-assembly, such as profilin (Goldschmidt-Clemont *et al.*, 1992), and the difference can be due to a single amino acid (Hertzog *et al.*, 2004).

Filament-capping proteins: Filament-capping proteins operate by the inverse principle, physically obstructing filament ends to prevent their continued growth (Carlier and Pantaloni, 1997). Filament-capping proteins can be specific for either the barbed- or pointed-end of a filament; thus they are also able to control the directionality of growth.

Actin nucleators. To date, four bona fide actin nucleators have been identified: Arp2/3 complex (Mullins *et al.*, 1997), formins (such as mDia) (Pruyne *et al.*, 2002), Spir (or Spire) (Quinlan *et al.*, 2005), and JMY (Zuchero *et al.*, 2009). In general, these actin nucleators are intrinsically inactive, requiring upstream signaling molecules for their activation (Takenawa and Suetsugu, 2007; Faix and Grosse, 2006; Goley and Welch, 2006; Bamberg, 1999). *In vivo*, this effectively limits actin nucleation to membranes. Amazingly, each of these classes of actin nucleators uses a distinct strategy to stabilize an actin nucleus (Figure 1.3). For instance, formins stabilize a lateral actin-dimer (Faix and Grosse, 2006); whereas, Spir proteins stabilize a longitudinal tetramer (Kerckhoff, 2006). JMY, which is not shown in Figure 1.3, is unique in that it uses both Arp2/3-like and Spir-like mechanisms for nucleating actin (Zuchero *et al.*, 2009). One other actin-binding protein, cofilin, which is canonically classified as an actin-depolymerizing protein, has also been shown to nucleate actin-assembly *in vitro* (Andrianantoandro and Pollard, 2006); however, its ability to initiate *de novo* actin filaments, particularly *in vivo*, still

Figure 1.3. Distinct mechanisms of actin nucleators.

The Arp2/3 complex. The first actin nucleator to be discovered was the Arp2/3 complex (see figure, part a), a macromolecular complex comprised of seven protein subunits. The complex structurally mimics a lateral actin dimer (yellow components of the figure) and is thought to require a pre-existing ‘mother’ filament from which a new ‘daughter’ filament can be initiated. By this method of growth, the Arp2/3 complex assists in the formation of branched actin superstructures. In migrating non-neuronal cells, the Arp2/3 complex assembles the highly branched actin superstructure of the lamellipodium at the leading edge (also known as the dendritic array).

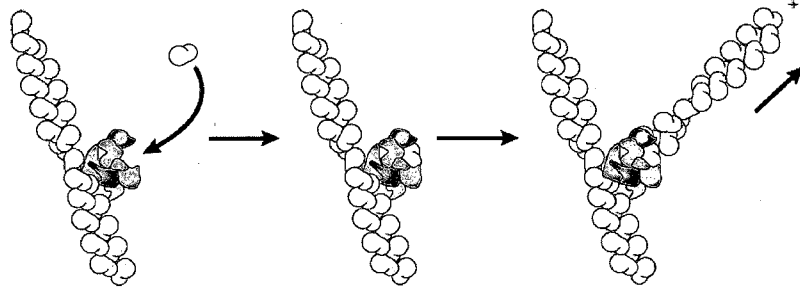
Formin proteins. Formins comprise a second class of actin nucleator (see figure, part b) and function as hinged dimers that bind two actin monomers. Unlike the Arp2/3 complex, formins follow the barbed ends of filaments (+ ends in the figure) during growth. In addition to stabilizing actin dimers, formins can also bind profilin–actin complexes, which accelerate monomer addition at the barbed end; thus, the formins are particularly implicated in the assembly of linearly bundled filaments.

Spir proteins. The Spir proteins (see figure, part c), which were originally discovered as the protein product of the *D. melanogaster* Spire gene, nucleate actin by a fundamentally different mechanism. Spir proteins can bind to four actin monomers to form a longitudinal tetramer that, when combined with another longitudinal tetramer, forms an octamer nucleus. Like the Arp2/3 complex, Spir proteins remain associated with the pointed ends of filaments. Overexpressed Spir proteins in mammalian cells co-localized with membranes of the Golgi apparatus and the exocyst. These findings suggest that Spir proteins are most likely to be involved in vesicle trafficking, rather than in leading-edge motility.

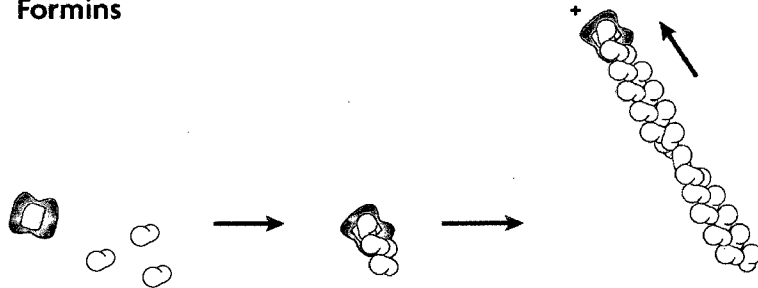
Cofilin. Despite its generic categorization as an actin-severing protein, cofilin can also stimulate actin assembly (see figure, part d), although the exact mechanism by which this occurs is currently ambiguous. Initially cofilin was thought to indirectly support actin assembly by generating free (uncaptured) barbed ends through its ability to sever actin filaments. However, more recent evidence indicates that cofilin might also directly stimulate actin assembly; cofilin can nucleate actin filaments *de novo* (although this ability is dependent on a high concentration ratio of cofilin to actin. There is also some evidence that cofilin might nucleate actin filaments *de novo* in migrating cells.

Stimulation of adenocarcinoma cells by epidermal growth factor triggers rapid actin polymerization (within 60 seconds) at the leading edge, which is dependent on cofilin activity. Inhibiting phospholipase-C (PLC) activation also blocks actin polymerization, and through its ability to cleave phosphatidylinositol-4,5-bisphosphate, active PLC might release a sufficient concentration of membrane-bound cofilin to favour actin nucleation. However, it cannot yet be determined which mechanism is used.

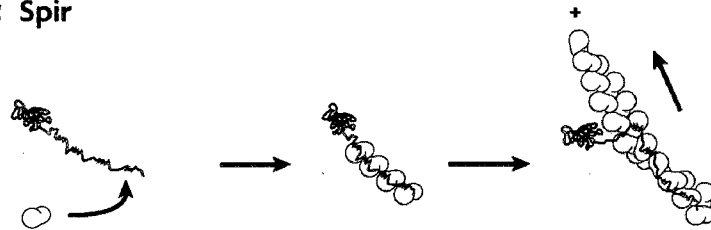
a Arp2/3



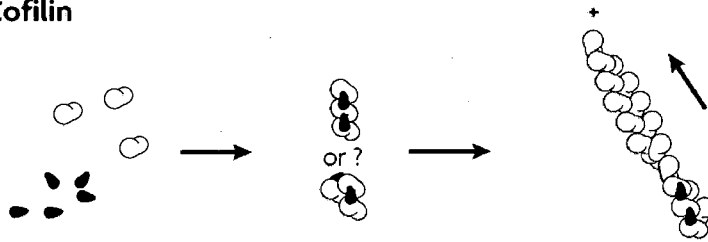
b Formins



c Spir



d Cofilin



remains a question because the effects of filament severing (see *Remodeling Proteins* for explanation) cannot be distinguished from *de novo* nucleation.

Tethering proteins. Rapidly after the nucleation of actin filaments, tethering proteins, such as members of the ezrin/radixin/moesin (ERM) protein family, link some of these actin filaments to the membrane (Polesello and Payre, 2004). Tethering proteins are just as important to the formation of actin superstructures as actin nucleators. However, a paradox of these proteins is that by tethering actin filaments to the membrane, they are also capping the filament end. The ERM proteins, therefore, cycle between tethering and untethering with a population of actin filaments. Since only some filaments are transiently tethered, the actin population is still capable of growing. A surprising example of this was demonstrated with the Wiskott-Aldrich syndrome proteins (WASP), which can capture actin-filament barbed ends but only after binding an actin monomer; in this case, a WASP-bound actin monomer functions as a bridging molecule (Co *et al.*, 2007). However, physical capture of filament ends does not always interfere with barbed end growth. For instance, the actin nucleator, formin, can simultaneously capture the barbed end of a single actin filament and facilitate its growth through 'leaky' insertion of a new actin subunit (Kovar *et al.*, 2006).

Cross-linking proteins. Cross-linking proteins control higher-order structuring by regulating interactions between individual actin filaments (Sato *et al.*, 1987; Gardel *et al.*, 2004). For instance, sparse and orthogonal cross-links between filaments can result in a mesh-like 'gel' of filaments with the cross-linker behaving like a joint for the filaments. Higher-ordering structuring of individual filaments is necessary for actin to perform mechanical work because of the poor stiffness of a single actin filament, which cannot

bear large stress loads without bending (Isambert *et al.*, 1995). The ability to bear large stresses without bending is described by the gels' viscoelasticity, which can vary by several orders of magnitude depending on differences in the density and net polarity of filaments within the gel (Wachsstock *et al.*, 1994; Gardel *et al.*, 2004). Thus, it is equally important to understand how actin filaments are organized in a population. Actin bundles can be formed by tighter and more frequent cross-links between filaments that can lead to a linear bundling of filaments. Bundling effectively increases actin's stiffness and persistence length by up to 600-fold *in vitro* (Claessens *et al.*, 2006). Similar to actin gels, whether filaments are oriented in parallel or anti-parallel directions can influence how the bundles deform, and the stiffness of an actin bundle can vary considerably depending on the actin-binding protein used, even if the same number of filaments is bundled. It should also be noted that an actin-binding protein can form either a gel or a bundle depending on its concentration ratio or its affinity to actin *in vitro* (Wachsstock *et al.*, 1994). It is therefore conceivable that gels and bundles *in vivo* can be dynamically interconverted simply by changing these parameters.

Remodeling proteins. Remodeling proteins disassemble actin filaments to permit the re-assembly of actin subunits into other superstructures. Disassembly can occur either by increasing the off-rate of individual actin subunits (pointed-end turnover) or by severing filaments into smaller-length fragments. Severing a filament has the potential effect of doubling the dissociation rate, since the number of filament-ends determines the average apparent off-rate, though ultimately this depends on the free actin-monomer concentration as well. The ADF/cofilin family of proteins directly disassembles actin filaments through their binding, which enhances either severing of the filament or the

turnover of pointed-end subunits (Carlier *et al.*, 1997; Bamburg, 1999). Their binding stabilizes a twisted conformation of the filament that normally occurs when ADP-actin subunits dominate (Galkin *et al.*, 2003). The ADF/cofilin proteins can also depolymerize filaments by sequestering actin monomers in a 1:1 stoichiometry (Paavilainen *et al.*, 2004), which effectively reduces the free actin monomer concentration available for assembly. The villin family of proteins, which contain gelsolin, fragmin, adseverin, among others, can also sever filaments, although, unlike the ADF/cofilin proteins, villin proteins can also cap the resulting barbed ends of filaments (Silacci *et al.*, 2004). Indeed, some members of the villin protein family, such as CapG, are only able to cap filaments and lack severing activity (Southwick and DiNubile, 1986). Villin proteins are also directly activated by Ca^{2+} -binding, which relieves auto-inhibition of its catalytic domain (Silacci *et al.*, 2004); therefore, their role in enhancing actin remodeling may be restricted to specific Ca^{2+} -dependent events.

Because the depolymerization and severing of filaments are important for the recycling of actin subunits, villin and ADF/cofilin proteins can paradoxically facilitate actin assembly. During growth epochs, severing of filaments indirectly increases the overall assembly rate by effectively doubling the filament-end concentration. However, cofilin may also facilitate actin assembly directly by nucleating actin when present at a high concentration relative to actin, though the structural mechanism for this is unknown. Nucleation-promoting activity has also been hypothesized for gelsolin, since it can bind to two actin subunits, but this has not been investigated.

Actin Superstructures

Actin superstructures are also self-organizing, a property that was elegantly demonstrated by the cell-free reconstitution of *Listeria monocytogenes* comet-tails but that was recognized in principle much earlier (Loisel *et al.*, 1999; Cameron *et al.*, 1999; Hill and Kirschner, 1982). This assay was seminal because it directly proved that a dynamic, force-producing actin-based machine could self-assemble from a mixture of actin monomers and a defined ensemble of actin-binding proteins without the need for external signaling or motor proteins. It also demonstrated that the generation of actin superstructures could be considered effectively as a two-step process. After overcoming the limiting barrier of *de novo* filament assembly (nucleation), the resulting organization of a growing population of filaments into a superstructure is driven by the milieu of actin-binding proteins that are present and active.

To understand how actin superstructures are spontaneously organized into complex architectures, the rules that govern actin binding must be considered. The most direct regulation of actin binding results from the protein's structure, which for some actin-binding proteins allows them to distinguish between sub-regions on a single actin superstructure, even at the level of a single actin filament. This discrimination is possible not only because of structural polarization but also because the time-course for ATP hydrolysis and γ -P_i release provides a molecular time-stamp for subunits within a filament (Carlier, 1990), a clue to the subunit's age. Owing to this, the filament can be heuristically divided into different strata based on the enrichment of specific actin-nucleotide complexes: ATP-actin, ADP·P_i-actin, and ADP-actin. In a filament that has reached steady-state growth, these three strata are maintained in a quasi-equilibrium state that also results in changes in the local topology of the filament. Ultimately, these strata

provide a multi-compartmental molecular scaffold for actin-binding proteins.

Reciprocally, actin-binding proteins as a group have evolved to exploit the intrinsic heterogeneity of an actin filament, and some can bind with considerable specificity and affinity to a specific stratum along the filament. For instance, coronin 1B was recently reported to have a 47-fold greater affinity for ATP-actin or ADP·P_i-actin subunits than for ADP-actin subunits; it therefore binds near the barbed ends (Cai *et al.*, 2007).

Likewise, Mena, a member of the Ena/VASP protein family, and cortactin are targeted to the front of the leading edge actin-based protrusions, presumably because of their high affinity for filament barbed ends (Loureiro *et al.*, 2002). Disruption of the F-actin-binding regions in coronin 1B, cortactin and Mena prevents their enrichment to the front of the leading-edge (Loureiro *et al.*, 2002). By contrast, cofilin binds with higher affinity to ADP-actin subunits in filaments than to ATP-actin or ADP·P_i-actin subunits; it is therefore enriched at the pointed ends of filaments (Bamburg, 1999).

The differential binding of certain actin-binding proteins to a stratum on a single filament reveals to some degree how superstructures can spontaneously self-organize. In migrating cells, actin-filament assembly is tightly restricted to a thin spatial plane at the leading edge of actin-protrusions within cells, and subunits that are incorporated at the same time make up a temporally linked network. That is, immediately following their birth into a common actin superstructure, ‘sister’ actin subunits move away from the leading edge at similar rates and ‘age’ on similar timescales. As a result, actin-binding proteins that show preferential binding to certain actin-nucleotide complexes or local topologies also organize into stratified layers within a superstructure.

The molecular stratification of nearly all actin superstructures underscores the importance of the spatial organization of actin nucleators, which largely determines the vector of filament growth (Figure 1.4). The growth of filaments is approximately perpendicular to and away from the ‘organizational plane’ (Figure 1.4). In the case of a spherical polystyrene bead used in the *L. monocytogenes* comet-tail assay, the initial result is a ‘cloud’ of actin filaments (van Oudenaarden and Theriot, 1999). In the case of leading-edge of actin-based protrusions, which is generally shaped like a thumbnail’s edge, actin superstructures are organized into a crescent. Though in reality, the assembly of *in vivo* actin superstructures is more complicated than described, the conceptual principles mentioned above still apply to provide a framework for understanding the generation of actin superstructures both within and outside of cells.

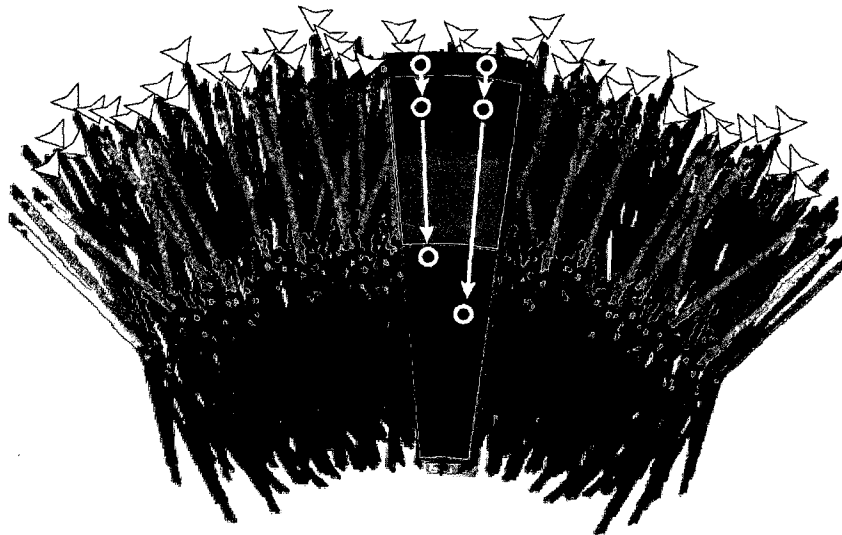
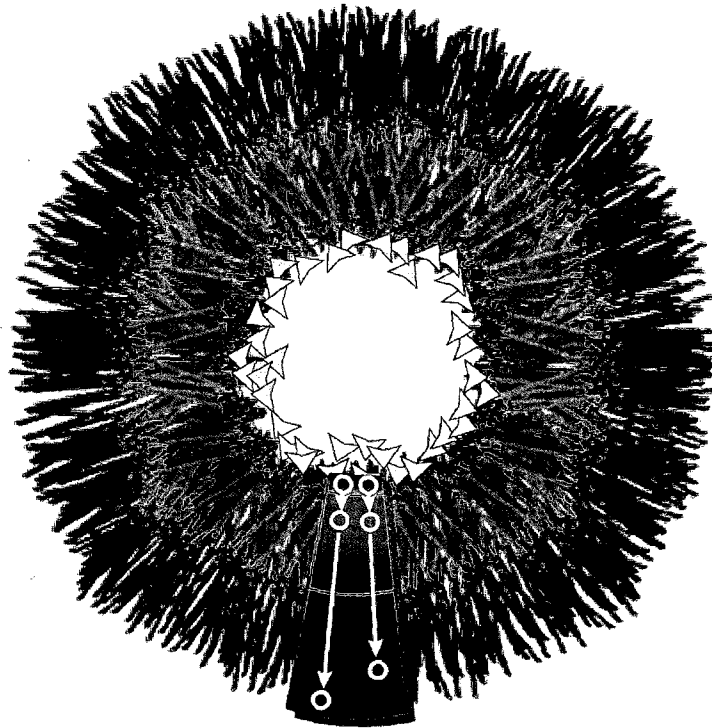
Ultimately, the ensemble activities of specific actin-nucleators and accessory actin-binding proteins establish a ‘program’ that determines the final nature of the actin superstructure. For instance, an actin-network can be gel-like or linearly-bundled depending on the actin-nucleator used. Also, the addition or subtraction of a single actin-binding protein to a program of actin-binding proteins can modify not only the overall architecture of the superstructure but also its behavior, for instance, its force-production. Though easier to recognize *in vitro*, programs of actin-binding proteins are also present *in vivo*.

The States of Actin – Distinct Superstructures

Actin superstructures have historically been regarded as spatially segregated entities because their classification has relied solely on fixed architectural characteristics,

Figure 1.4. The geometry of superstructure strata is determined by the organizational plane of actin nucleators.

Conceptual representations of actin superstructures that might result from the actions of actin nucleators that have been localized to surfaces with unique geometries (organizational planes). Two principles of actin-superstructure organization are demonstrated. First, the organization and orientation of actin nucleators determine the direction of filament growth. Second, average times for ATP hydrolysis and Pi release result in the molecular stratification of superstructures based on the enrichment of specific actin-nucleotide complexes (ATP-actin (shown in blue), ADP·Pi-actin (shown in green), or ADP-actin (shown in maroon), despite ATP hydrolysis and Pi release being stochastic for each subunit. (top panel) A cross-section of a bead that has been homogeneously coated with actin nucleators (represented by the yellow arrowheads) that are orientated radially outward; consequently, actin filaments also grow radially outward (represented by the white arrows), forming a 'cloud'-shaped actin superstructure. (bottom panel) A concave surface coated with actin nucleators (yellow arrowheads) results in actin filaments that grow perpendicular to the surface.



making the discrimination of overlapping but dynamically distinct superstructures nearly impossible. This technical barrier has been overcome with the advent of a live-cell imaging technique known as fluorescent speckle microscopy (FSM), which was pioneered in non-neuronal cells for the study of cytoskeletal dynamics (Waterman-Storer *et al.*, 1998). FSM is unique in that it can reveal the movements and lifetimes of individual subunits incorporated into actin superstructures. At the leading edge of newt lung and potoroo kidney epithelial cells, FSM revealed two distinct populations of actin speckles, which had different lifetimes and rates of retrograde-movement (Ponti *et al.*, 2004). From these observations it was reasoned that the leading edge in these cells was comprised of two distinct superstructures that make up the cellular protrusions of the lamellipodium and the lamellum, respectively (Gupton *et al.*, 2005; Iwasa and Mullins, 2007; Delorme *et al.*, 2007).

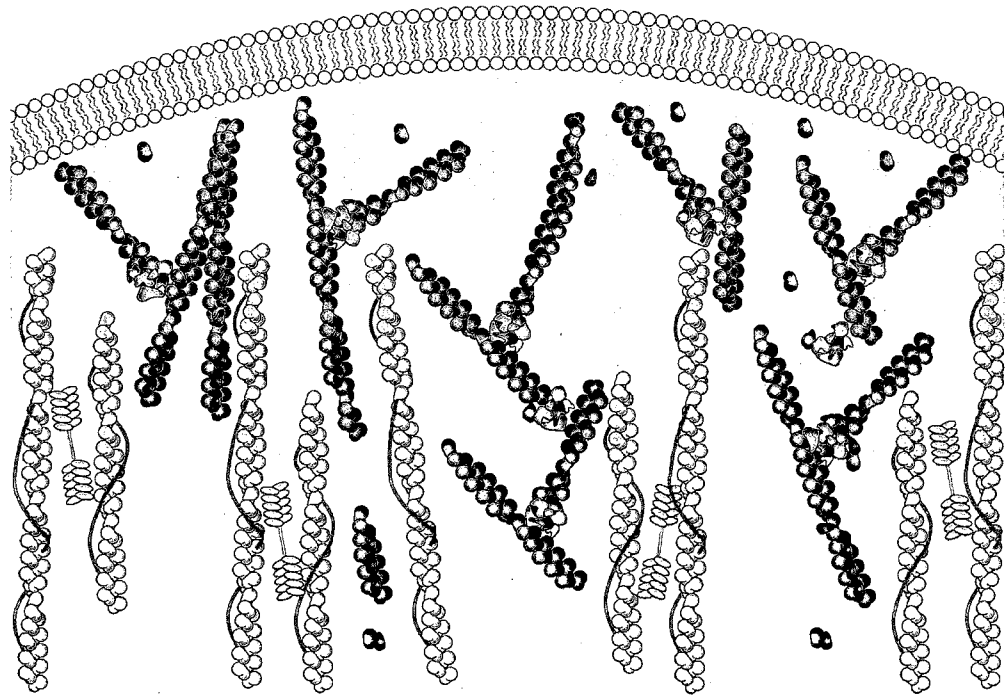
Although the complexities of generating and maintaining spatially overlapping but distinct superstructures have limited their study, the tropomyosin proteins have been shown to play a crucial role in this process. Tropomyosin proteins can preclude or facilitate the binding of other actin-binding proteins to filaments, thereby regulating the content of a filament's actin-binding-protein 'shell'. Tropomyosin proteins are alpha-helical coiled-coil proteins that bind cooperatively in a head-to-tail manner along actin filaments (Gunning *et al.*, 2005). Tropomyosin isoforms arise from four different mammalian genes, each of which might use different promoters. In addition, tropomyosin transcripts undergo alternative splicing, contributing even further to their diversity and potentially giving rise to more than 40 different isoforms in total (Gunning *et al.*, 2005). These isoforms can be generally classified as high-molecular-weight (HMW) or low-

molecular-weight (LMW). Different tropomyosin isoforms can either antagonize or synergize the binding and activities of other actin binding proteins (Bryce *et al.*, 2003). In fact, the selective localization of HMW tropomyosins to the lamella and their exclusion from the lamellipodium defines these structures (Figure 1.5). Myosin II motors are recruited to the lamella by actin filaments bound to HMW tropomyosins, whereas cofilin competes with HMW tropomyosins for binding filaments in the lamellipodium (DesMarais *et al.*, 2002).

Differences in superstructure organization can have profound physiological effects. For instance, when the lamellipodium of potoroo cells is experimentally disrupted by micro-injecting skeletal muscle tropomyosins (skTM), the treated cells migrate at a faster rate (~ two-fold faster) and with greater persistence (~ two-fold greater) than untreated cells (Gupton *et al.*, 2005). This demonstrates that the lamellum, which is largely unaffected by skTM treatment, is architecturally and mechanically unique from the lamellipodium, which was already suggested by kinematic analysis using FSM. This example exemplifies not only the potential experimental gains of manipulating actin's self-organization but also of its physiological consequences. This paradigm of thinking establishes the basis for the projects presented within this thesis.

Figure 1.5. Distinct but spatially overlapping actin superstructures of lamellae and lamellipodia.

In some migrating cells, actin filaments at the leading edge are organized into either the cofilin-rich, highly branched superstructure of the lamellipodium (red filaments) or the tropomyosin-rich, less-branched superstructure of the lamellum (green filaments). The lamellipodium extends only 1–2 μm beneath the leading-edge membrane, where the filaments are severed or disassembled into fragments and monomers. The less-branched superstructure of the lamellum extends further (3–5 μm) beneath the leading-edge membrane (only the overlapping region is shown). Tethering of the filaments to the membrane is not shown. Filaments that comprise the lamellipodium recruit cofilin (navy blue), which competes for binding with the high molecular-weight (HMW) tropomyosin isoforms (brown lines). Owing to HMW tropomyosin binding in the lamellum, bipolar myosins (tan) are also recruited to this superstructure.



Chapter 2

Stochastic simulation of actin dynamics reveals the role of annealing and fragmentation

Preface and Acknowledgement

Work in this chapter was published in the *Journal of Theoretical Biology* (Fass *et al.*, 2008). The order and list of the authors include: Joseph Fass (JF), Chi Pak (CP), James R. Bamburg (JRB) and Alex Mogilner (AM). My contribution to this project involved developing code for the simulations, which was initially done in Matlab and later transferred to the programming language, C++. Nearly all of the data structures, the implementation of simulation-events, and initial simulation-runs were accomplished here at CSU, before Joseph Fass moved to Alex Mogilner's lab at UC Davis, where he completed the project and manuscript. Since our publication, other groups have used stochastic simulations using a similar algorithm to investigate other actin-related processes, including the influence of actin-binding proteins on actin dynamics.

This work was supported by National Science Foundation grant DMS-0715729 to AM and Predoctoral Fellowship DGE-0234615 to CP, and by National Institutes of Health grants NS43115 to JF, GM35126 and NS40371 to JB, and GLUE grant "Cell Migration Consortium" (NIGMS U54 GM64346) to AM. We are grateful to members of the Bamburg lab for their suggestions and discussions, including Alisa Shaw, Laurie Minamide, Kevin Flynn, Lubna Tahtamouni, O'Neil Wiggan, Mike Maloney, Janel Funk, and Patrick Sarmiere.

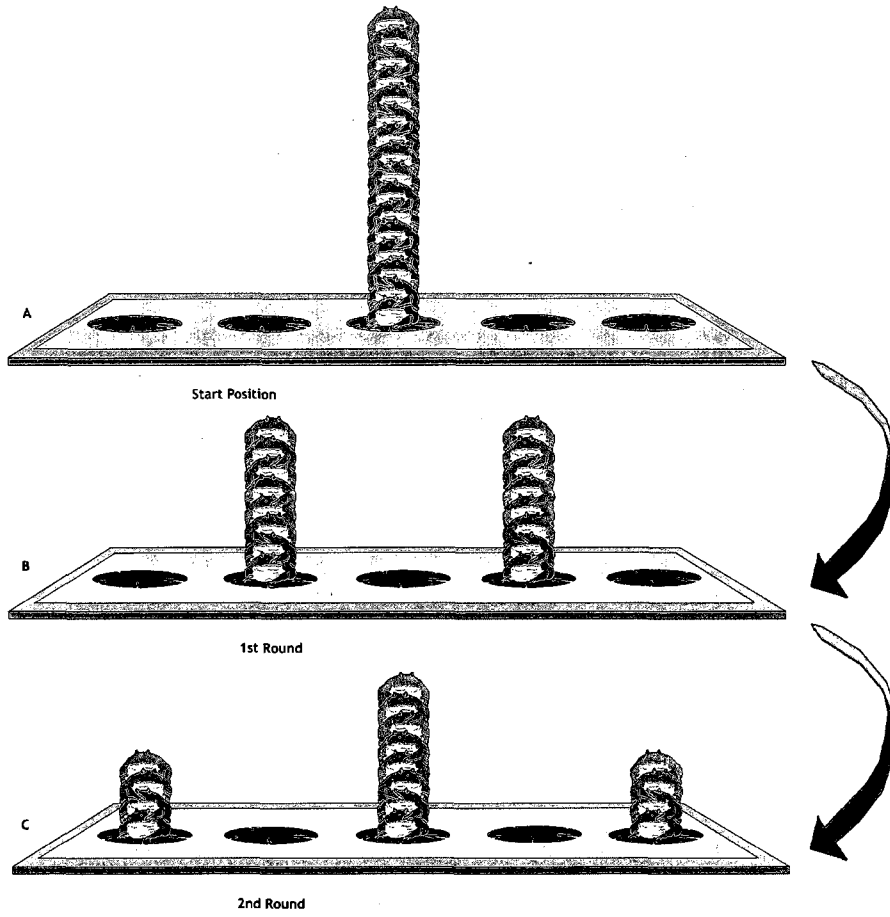
A Primer on 1-Dimensional Diffusion

The purpose of this primer is to demonstrate how actin treadmilling can be analyzed using 1-D diffusional analysis, as this will be essential to understanding the work presented in this chapter. Simple-diffusion describes the random and independent movement of $<$ micron-sized objects that arises from thermal energy; however, diffusional analysis need not be applied only to situations that explicitly involve movement, and can be a useful method of analysis for other systems. Diffusional analysis, as it is applied to movement, is used to quantitatively describe the spatial distribution of a group of objects over time. In an idealized case, the spatial distribution is binomial, which is a classic statistical distribution describing the frequency and probability of multiple binary events. In the next few paragraphs, we will use a simple thought experiment to examine how the spatial distribution of objects undergoing simple-diffusion in 1-dimension is described by a binomial-distribution.

To begin our thought experiment, imagine 16 frogs stacked in a tall column on a lily pad (Figure 2.1A). Each frog is forced to hop but only once during a round and are only strong enough to hop to an immediately-adjacent lily pad, many of which are laid out along one axis. Frogs may hop in either direction (left or right) of their random choosing. In our thought experiment, we are interested in the relative spatial distribution of the frogs after each round of their random-hops. After the first round of random hopping, approximately half of the frogs have chosen to jump left and the other half right (Figure 2.1B). As a group, they are split evenly between the left-of-center and right-of-center lily pads. This is analogous to flipping 16 coins; half the coins should fall heads. Thus, each frog is determining the outcome of a binary choice when they hop, much like

Figure 2.1. Random frog-hopping in 1-dimension.

1-dimensional random frog-hopping is described by a binomial distribution. (A.) 16 frogs are stacked on the center lily pad to begin. (B.) After the first round of random hopping, half of the frogs have jumped to the left-of-center lily pad and the other half of frogs to the right-of-center lily pad. The frogs are evenly distributed about the center lily pad. (C.) After the second round of hopping, 4 frogs are on the left-most lily pad, 8 frogs are back on the center lily pad, and 4 frogs are on the right-most lily pad. The mean distribution of frogs is still evenly distributed about the center lily pad (net displacement = 0) but with each successive round, the frogs, by percentage, continue to hop away from the center lily pad.



flipping an imaginary coin. In the second round, frogs are faced with the same choice, hop left or hop right. We will now only consider frogs that are on the left-of-center lily pad, on which there are approximately 8 frogs. To hop two lily pads left of the original-center, a frog must hop left twice in a row. This is analogous to flipping a coin heads twice in a row, which has a 25% chance of occurring, or the multiplicative product of the probabilities for each independent trial (50% x 50%). However, the other frogs will have hopped back to the center lily pad; thus having hopped left once and then right once. When frogs on the right-of-center lily pad are also considered, the overall relative distribution of frogs after the second round of hopping is 25% left, 50% center, and 25% right (Figure 2.1C). What should be evident from this brief thought experiment is that random frog-hopping, which is analogous to random molecule-movement, follows a binomial (or binary) process.

Thus, it is possible to determine whether a molecule moves by random-walk (diffusion) based on properties of its spatial distribution over time. First, the average displacement of molecules, that is, the average net distance molecules have moved away from the center, is always zero for 1-D diffusive processes. Because 1-D diffusion is directionally unbiased, the percentage of molecules that have moved right is the same percentage of molecules that have moved left. Second, the variance of the distribution, or how spread-out the molecules are, varies linearly with time. The exact relationship is described by the equation below, where $\langle x^2 \rangle$ is the variance of the distribution, D is the diffusion-coefficient and t is time: $\langle x^2 \rangle = 2 D t$. In simple terms, the diffusion-coefficient can be regarded as the average 'step-size' of a molecule. Larger steps permit a molecule to spread out faster.

When applying 1-D diffusional analysis to actin treadmilling, the movement of individual actin molecules is not explicitly considered; instead, relative length-changes in actin filaments (filament length-changes) are considered. Since only *relative* changes in filament length are considered, it is relatively unimportant to consider the number and absolute lengths of filaments; therefore, 1-D diffusional analysis can be performed irrespective of the initial actin polymerization conditions. Filament length-changes during treadmilling are amenable to diffusional analysis because the statistics of filament length-changes satisfies the two criteria described above: 1. net length-changes equal zero and 2. the variance of length-changes scales linearly with time. By definition, actin filament length-changes satisfy the first criterion. Because treadmilling occurs at steady-state, the mass of polymers and monomers remains constant during this phase; therefore, no net change in filament lengths is possible. The second criterion is less obvious to determine but was first demonstrated by Fujiwara *et al.* To determine this, the variance of the distribution of filament-length changes ($\langle L^2 \rangle$) is plotted relative to the difference in time between when length-measurements are taken ($\Delta\tau$). A linear relationship describes simple-diffusion; a non-linear relationship describes anomalous diffusion. Using this method of analysis, Fujiwara *et al.* were able to demonstrate that filament length-changes follow a simple-diffusion model.

Abstract

Recent observations of F-actin dynamics call for theoretical models to interpret and understand the quantitative data. A number of existing models rely on simplifications and do not take into account F-actin fragmentation and annealing. We use Gillespie's

algorithm for stochastic simulations of the F-actin dynamics including fragmentation and annealing. The simulations vividly illustrate that fragmentation and annealing have little influence on the shape of the polymerization curve and on nucleotide profiles within filaments but drastically affect the F-actin length distribution, making it exponential. We find that recent surprising measurements of high length diffusivity at the critical concentration cannot be explained by fragmentation and annealing events unless both fragmentation rates and frequency of undetected fragmentation and annealing events are greater than previously thought. The simulations compare well with experimentally measured actin polymerization data and lend additional support to a number of existing theoretical models.

Introduction

The dynamics of actin filaments is central to many cellular behaviors, including cell migration and cytokinesis (Bray, 2001). Classic experimental and theoretical studies during the 1970's and '80's elucidated minute details of actin nucleation and the subsequent rapid elongation of actin filaments, and many relevant rates were measured directly and/or calculated (Oosawa and Asakura, 1975; Pollard, 1986; Wegner and Savko, 1982). Subsequently, the process of filament treadmilling – in which ATP-G-actin assembles at the growing barbed end, hydrolysis takes place in the middle of the filament, and ADP-G-actin dissociates from the shrinking pointed end – was predicted and observed (Pollard *et al.*, 2000). It has also become clear that treadmilling alone does not explain all observed actin turnover *in vivo*; rather, cells control the length distributions and dynamics of F-actin arrays via a host of actin accessory proteins such as

ADF/cofilin, profilin, capping proteins etc. (Pollard *et al.*, 2000). Many experimental and theoretical studies have examined the effects of the various actin binding proteins.

However, many questions about basic, unmodulated actin dynamics remain unanswered.

These include the nature and rates of γ -phosphate hydrolysis and release (Pieper and Wegner, 1996), the significance of different subunit conformations and orientations within the filament (Galkin *et al.*, 2003), and the prevalence and nature of end-to-end filament annealing (Andrianantoandro *et al.*, 2001; Howard, 2001), among others.

Recently, direct observations of actin filaments have become possible at timescales sufficient to address some of these issues. One characteristic of F-actin dynamics under current scrutiny is length diffusivity: a value related to the mean expected length change during a given time interval for a dynamic polymer. For a one-dimensional diffusion-like process of length change, $\langle \mathbf{x}^2 \rangle = 2 \mathbf{D} \mathbf{t}$, where \mathbf{x} is the length change, \mathbf{t} is time, and \mathbf{D} is diffusivity (Einstein, 1956). Thus, length diffusivity is calculated by plotting the mean squared length change – derived from a whole population of dynamic filaments – versus the time lag over which those changes are measured; for a diffusion-like process this produces a linear, increasing trend, and \mathbf{D} is half the slope. Two groups have recently used TIRF microscopy to observe the lengths of individual actin filaments (Fujiwara *et al.*, 2002; Kuhn and Pollard, 2005). In both cases, the calculated length diffusivity \mathbf{D} (~ 30 monomer²/sec) was over an order of magnitude greater than that expected for actin filaments at the critical concentration (~ 1 monomer²/sec).

Various mechanisms have been proposed to explain this unexpected result: (i) measurement error that increases during the course of observation, which could cause

artifacts increasing calculated diffusivity; (ii) “dynamic instability”-like behavior similar to that observed in microtubules (rescues and catastrophes occur when a terminal ATP-actin subunit(s) is added or lost followed by rapid growth or shortening of the barbed end, respectively); (iii) vectorial, rather than random, ATP hydrolysis in the filaments, (iv) pauses, preventing subunit loss or addition, that are either a natural yet heretofore unobserved behavior or arise from temporary attachments between filament ends and the glass coverslip; and (v) addition and loss of short fragments of F-actin, rather than individual monomers.

Of these mechanisms, the statistics of experimental errors are difficult to characterize, and further experiments that characterize or control for measurement errors would be helpful in testing the plausibility of mechanism (i). Fujiwara *et al.* (Fujiwara *et al.*, 2002) did not observe pauses (iv) in filament length histories, while Kuhn and Pollard did but discarded obvious pauses in the analysis of the length diffusivity (Kuhn and Pollard, 2005). Besides, the pauses would only increase the calculated length diffusivity for filaments undergoing net polymerization or depolymerization; both groups calculated unexpectedly high length diffusivities at or near the critical concentration (Fujiwara *et al.*, 2002; Kuhn and Pollard, 2005), where pauses should have little or no effect. Thus, undetected pauses are not likely to explain the length diffusivity observations.

The effective dynamic instability mechanism (ii) has been addressed by two recent theoretical studies, both of which examined the dependence of length diffusivity on G-actin concentration (Vavylonis *et al.*, 2005; Stukalin and Kolomeisky, 2006). By considering subunit addition and loss at barbed and pointed ends, and assuming random hydrolysis and slow phosphate release (consistent with rate constants in (Pollard *et al.*,

2000)), Vavylonis *et al.* showed that the length diffusivity should reach the levels observed via TIRF microscopy (~ 30 monomer²/sec) just below the critical concentration, then drop to $\sim 1-5$ monomer²/sec at and above the critical concentration (Vavylonis *et al.*, 2005). This behavior was attributed to mini-catastrophes/rescues, which are most prevalent just below the equilibrium concentration for ATP-actin at the barbed end. At such concentrations, “catastrophes” of consecutive ADP-actin losses and “rescues” of ATP-actin additions are both maximized. At concentrations very close to the critical concentration, however, treadmilling results in few ADP-actin subunits near the barbed end, and catastrophes decline. Stukalin and Kolomeisky, on the other hand, assumed a single vectorial hydrolysis and phosphate release step (iii), which they calculated would result in high diffusivity (~ 30 monomer²/sec) just above the critical concentration (Stukalin and Kolomeisky, 2006). This is due to the fact that vectorial hydrolysis “targets” ATP to ADP conversions to the barbed end, keeping the ATP cap small. However, they used a relatively large rate (0.3 s^{-1}) to describe the combined phenomena of vectorial hydrolysis and subsequent phosphate release. In addition, while still controversial, experimental evidence favors random hydrolysis over vectorial or non-random mechanisms (Pieper and Wegner, 1996).

There have been no detailed stochastic simulations of actin filament length that account for the processes of annealing and fragmentation, which change filaments’ lengths drastically and abruptly. Therefore, we introduced these phenomena into stochastic simulations of populations of actin filaments to test mechanism (v): that fragmentation and annealing complement subunit addition and loss to enhance length diffusivity. We found that at normal fragmentation rates the diffusivity at critical

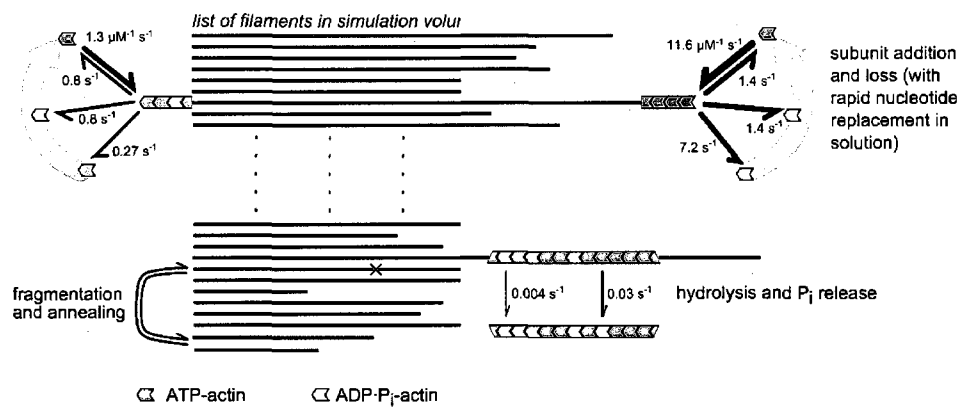
concentrations remained low, and only a combination of enhanced fragmentation rates and experimental errors greater than expected could increase the diffusivity to the observed level.

We also used the simulations to examine the effects of filament annealing and fragmentation on the nucleotide distribution within the filaments, polymerization kinetics and filament length distribution. Both the polymerization kinetics and nucleotide profiles were largely unaffected by the incorporation of annealing and fragmentation. The filament length distribution, on the other hand, changed drastically, from broad, flat and initial condition-dependent in the absence of annealing and fragmentation to a stable stationary exponential distribution (independent of initial conditions) in their presence, in agreement with previous experimental studies (Kas *et al.*, 1996; Sept *et al.*, 1999). Finally, our simulations support a number of existing simplified models of actin dynamics.

Methods

Monte Carlo simulations were performed using Gillespie's First Reaction algorithm (Gillespie, 1977; Gibson and Bruck, 2000). A random time interval was generated for each possible event in the reaction volume V : nucleation (subunit addition to a trimer); complete depolymerization of a filament (loss of a subunit from a tetramer); ATP-actin addition to a filament's barbed or pointed end; ATP-, ADP·P_i-, or ADP-actin loss from a barbed or pointed end; γ -phosphate hydrolysis; γ -phosphate release; filament-filament annealing; random fragmentation; stress-induced fragmentation (Figure 2.2). Actin dimer concentration was calculated assuming equilibrium with monomers, and then

Figure 2.2. Reactions of actin dynamics implemented in our simulation. Subunit addition and loss from the fast-growing barbed end (to the right) and slow-growing pointed end (to the left) are modeled, as well as γ -P_i hydrolysis and release from within each filament. Subunit recharging (replacing ATP for ADP or ADP·P_i) is assumed to occur instantaneously once a subunit is in solution. Two mechanisms of filament fragmentation (random and stress-induced) as well as end-to-end annealing (see text) are also modeled. Constants for all reactions are listed in Table 2.1.



trimer concentration was calculated assuming equilibrium with dimers. Rate constants from Brownian dynamic simulations were used for both calculations (Sept and McCammon, 2001). Table 2.1 shows the values and references for all rate constants used. All events were modeled as first order or pseudo-first order events, and time intervals generated according to the equation $t = -\ln(r) / k$, where r is a uniformly distributed random number on $(0, 1]$, and k is the first order or effective pseudo-first order rate constant. For N independent, identical events with the same rate constant k' , the effective rate constant $k = N \times k'$ was used. After time intervals for all possible events were generated, the event with the minimum time interval was then implemented, the current time of the simulation was updated by that time step, and then the whole process was repeated.

In order to save calculation time, we only generated one random time interval for annealing at each time step: $t = -\ln(r) / (N \times k_a)$, where k_a has units of seconds^{-1} and is the pseudo-first order annealing rate constant of the form $k_a = [N] \times (10/\text{sec}) / (1 + 0.01 \times \langle L \rangle)$, where $[N]$ is the number concentration of filaments and $\langle L \rangle$ is the mean filament length in subunits. This form for k_a was suggested by Andrianantoandro *et al.* (Andrianantoandro *et al.*, 2001). If the annealing time was the minimum time, we then chose a random barbed end and a random pointed end to anneal. Using this method for simulation of annealing, we were able to reproduce the experimental results of Andrianantoandro *et al.* (Andrianantoandro *et al.*, 2001) with very little error (Figure 2.3).

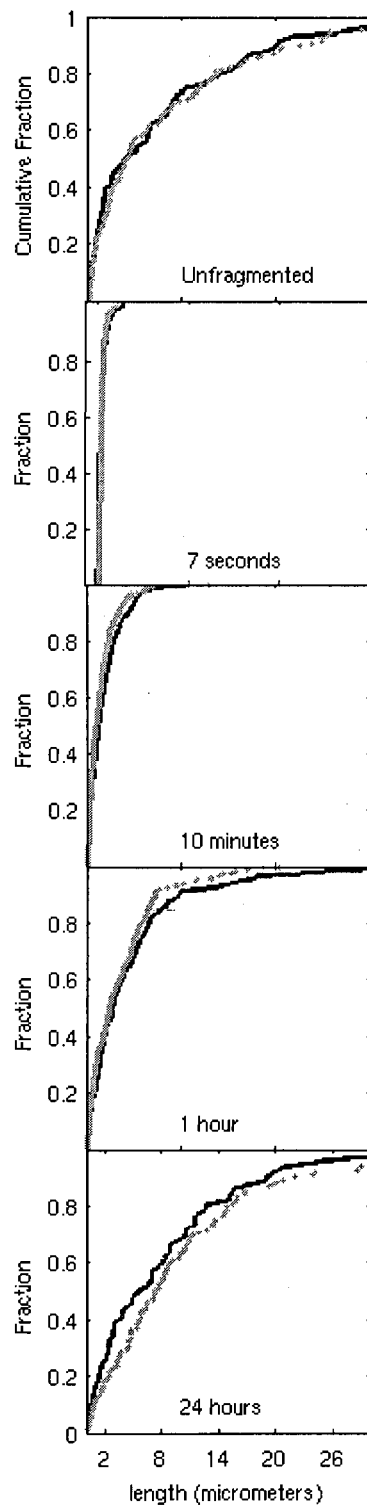
We simulated two pathways for fragmentation, using the random and stress-induced mechanisms described in Sept *et al.* (Sept *et al.*, 1999). For random

Table 2.1. Rate constants and reactions used in our simulation.

| Event | Rate Constant |
|---|---|
| <i>Nucleation steps</i> | |
| monomer to dimer | $35.7 \mu\text{M}^{-1} \text{s}^{-1}$ |
| dimer to monomer | $1.63 \text{e}8 \text{s}^{-1}$ |
| dimer to trimer | $2.18 \mu\text{M}^{-1} \text{s}^{-1}$ |
| trimer to dimer | $1.3 \text{e}3 \text{s}^{-1}$ |
| <i>Subunit addition/loss</i> | |
| ATP-actin addition at barbed end | $11.6 \mu\text{M}^{-1} \text{s}^{-1}$ |
| ATP-actin addition at pointed end | $1.3 \mu\text{M}^{-1} \text{s}^{-1}$ |
| ATP-actin loss from barbed end | 1.4s^{-1} |
| ADP·P _i actin loss from barbed end | 1.4s^{-1} |
| ADP-actin loss from barbed end | 7.2s^{-1} |
| ATP-actin loss from pointed end | 0.8s^{-1} |
| ADP·P _i actin loss from pointed end | 0.8s^{-1} |
| ADP-actin loss from pointed end | 0.27s^{-1} |
| Hydrolysis (ATP- to ADP·P _i -actin) | 0.3s^{-1} |
| Phosphate release (ADP·P _i to ADP-actin) | 0.004s^{-1} |
| <i>Fragmentation/Annealing</i> | |
| random fragmentation | $1.1 \text{e}3 \text{ subunits}^{-1} \text{s}^{-1}$ |
| stress-induced fragmentation | $1.8 \text{e}3 \text{ subunits}^{-2} \mu\text{M}^{-1} \text{s}^{-1}$ |
| annealing | $[10 + (1 + 0.01 \times \langle L \rangle)] \mu\text{M}^{-1} \text{s}^{-1}$ |

Figure 2.3. Validation of annealing and fragmentation versus published experimental data.

Our model, implemented as described in Methods, was used to simulate an experiment carried out in Andrianantoandro et al., 2001 (Andrianantoandro et al., 2001). Briefly, 0.5 μ M actin was polymerized in the presence of phalloidin to eliminate monomer addition and loss from filaments. The filaments were then mechanically sheared to an average length less than 0.5 micrometers, after which they were sampled, and the length distribution characterized by light microscopy, at various time points over 24 hours. We simulated the presence of phalloidin by reducing all subunit off-rates to zero, and mechanical shearing by increasing the random fragmentation rate constant by 10 orders of magnitude until the desired average length was achieved. Simulated distributions (*gray '+'*) matched the measured distributions closely (*black lines*; data provided by Ernesto Andrianantoandro).



fragmentation, a random time was generated for each filament using the rate constant $k_i = k_{fr} \times L_i$. For stress-induced fragmentation, a random time was generated for each filament using $k_i = k_{fs} \times \langle L \rangle^2 \times [N]$; k_{fr} and k_{fs} are listed for random and stress-induced fragmentation in Table 1. If either fragmentation mechanism had the minimum event time, a random site for fragmentation was chosen, with no biases, from every subunit-subunit bond in the appropriate filament.

The state (ATP-, ADP·Pi-, ADP-actin) and relative position of each subunit within each filament in the simulation volume was tracked. The positions and orientations of filaments within the volume were not simulated. Because the model was not spatial in nature, and filaments within the simulation volume were taken to be representative of an arbitrarily larger reaction volume, diffusive movement of filaments into and out of the volume were not considered. The size of the simulation volume was adjusted in order to keep the number of filaments within a chosen range (usually 300 to 600) as follows. If, due to nucleation or fragmentation events, the number of filaments increased beyond the chosen upper limit, the size of the simulation volume was decreased by one third, and each filament was given a 1 in 3 chance of being discarded. If, due to depolymerization or annealing, the number of filaments decreased beyond the chosen lower limit, the size of the simulation volume was increased by 50% and each filament was given a 1 in 2 chance of being duplicated and the duplicate then added to the list of filaments within the simulation volume. This alleviated the dilemma between choosing a large fixed simulation volume, which would allow initial nucleation over a reasonable timescale but cause very slow computation once many filaments had formed, and a small fixed simulation volume, which would run quickly later on at high filament number

concentrations, but in which nucleation would be poorly modeled as only one filament would represent the whole reaction volume at early times.

In order to simulate the experimental conditions in Fujiwara *et al.* we chose to start with a higher initial concentration of free actin than the 0.3 μM they used (for Mg-actin) (Fujiwara *et al.*, 2002), because in simulations 0.3 μM actin requires on the order of 24 hours to fully polymerize. This is due, most likely, to the presence of small numbers of proteins that modulate actin dynamics in experimental purifications. Instead, we started simulations at 3.0 μM , then after 5 minutes reset the concentration to 0.3 μM , and allowed it to change freely after that. This resulted in a rapid initial burst of nucleation which allowed the simulated concentration to reach the critical concentration ($\sim 0.14 \mu\text{M}$) in about an hour, much closer to the reported time of $\sim 20\text{-}25$ minutes (Fujiwara *et al.*, 2002).

Measurements were simulated by recording the lengths of all filaments in the simulation volume at one minute intervals after the critical concentration was attained. However, in order to adequately simulate the measurement process employed by Fujiwara *et al.* and Kuhn and Pollard, we needed to discard length histories in which obvious annealing events took place, as both groups did (Fujiwara *et al.*, 2002; Kuhn and Pollard, 2005). In addition, neither group observed fragmentation. This may have been because all filaments under observation were attached at one or several points to the glass coverslip, which may have stabilized them against fragmentation. Nevertheless, short segments at the ends of filaments could still have undergone fragmentation while escaping detection via time-lapse imaging. In order to account for both of these experimental phenomena, we used a parameter henceforth referred to as the “detectability

limit” in our analysis of filament length histories. The detectability limit represents a threshold length change such that either (i) an observer would have discarded the length history (in the case of annealing events), or (ii) the event would have been prevented by coverslip attachment (in the case of fragmentation events). While the length limits on these two phenomena could differ, we chose to introduce only one free length threshold parameter to our model.

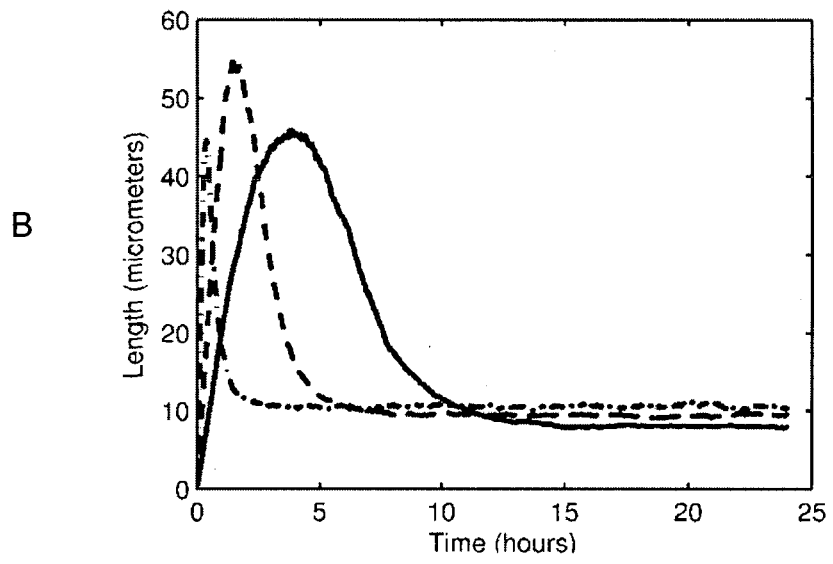
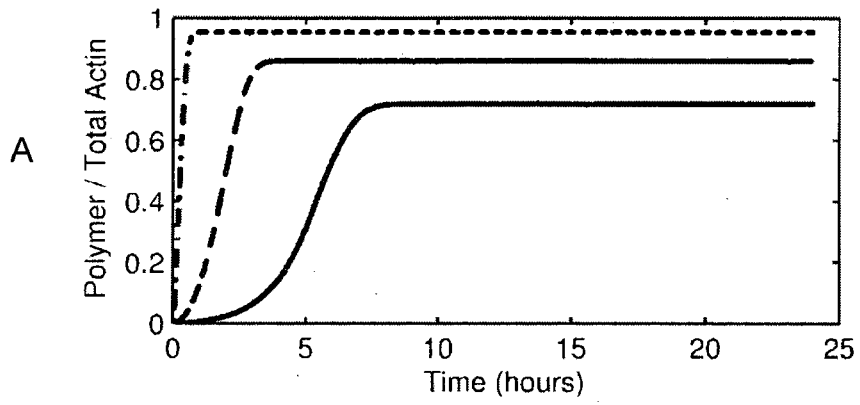
Rather than discard all the measurements in a length history, we simply broke a length history into two consecutive histories if an instantaneous (i.e. from one event to the next) length change greater than the detectability limit occurred. However, two consecutive measurements could still differ by an amount greater than the detectability limit due to several individual changes that are each less than the detectability limit, in addition to the contribution of subunit addition or loss. In addition, zero-mean Gaussian measurement error with a standard deviation of 0.54 μm , consistent with the error reported by Fujiwara *et al.* (Fujiwara *et al.*, 2002), was added to all recorded lengths, increasing the possibility that two consecutive measurements could differ by more than the detectability limit.

Results

Simulations of filament populations reveal minute details of actin dynamics.

Variable volume stochastic simulations of actin polymerization allow vivid illustration of the evolution of filament length distributions during polymerization. Figure 2.4 shows the polymerization kinetics (Figure 2.4A) and the average filament lengths (Figure 2.4B) over 24 hours for different initial free actin concentrations. Polymerization kinetics at

Figure 2.4. Polymerization kinetics modeled using stochastic simulation. Actin is polymerized for initial actin concentrations of 0.5 (*solid*), 1.0 (*dashed*), and 3.0 μM (*dash-dot*). Data is averaged from 5 simulations at each concentration. (A.) Time series for polymerized fraction using three initial actin concentrations. (B.) Average lengths for simulated populations, corresponding to simulations in *panel A*.

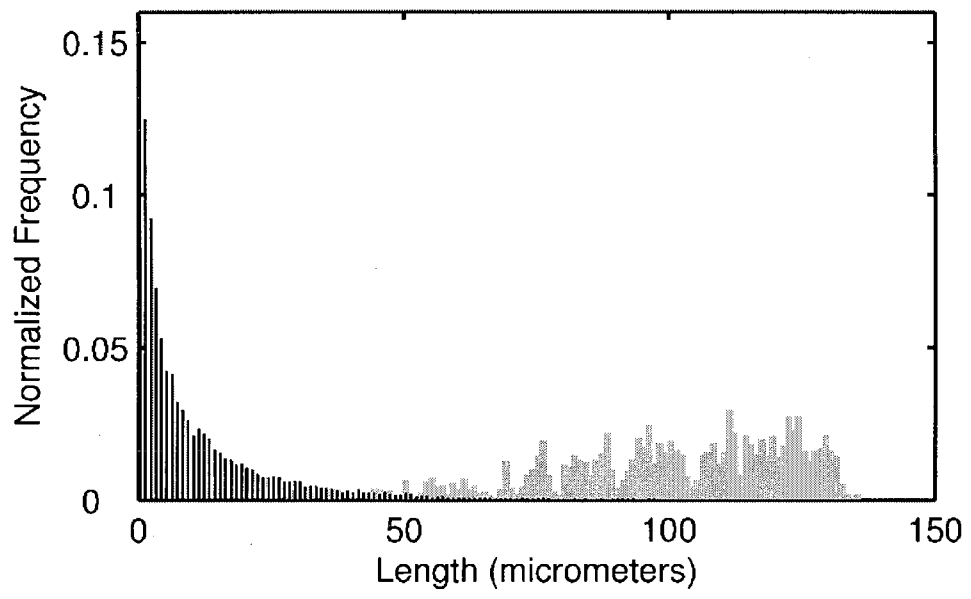


given rates of actin dynamics is insensitive to the the presence or absence of normal fragmentation/annealing. It is characterized by, first, an initial lag phase which can last for several hours for initial G-actin concentrations below 1 μM and is a decreasing function of this concentration. The amount of F-actin then increases linearly over a period of hours until saturation, at which G-actin reaches the critical concentration: $\sim 0.14 \mu\text{M}$. At actin concentrations in the range of 1 to 10 μM , the lag and growth phases decrease to minutes. The simulated features of the polymerization kinetics in the absence of the fragmentation/annealing are in qualitative agreement with earlier data and calculations (Cooper *et al.*, 1983; Tobacman and Korn, 1983).

Although polymerization curves produced by simulations with and without fragmentation and annealing are similar, the evolution of filament length distributions is quite different. Initially, prior to significant G-actin depletion, the nucleation and filament elongation rates are almost constant, so filaments appear and grow at constant rates resulting in roughly uniform length distribution, the upper limit of which grows linearly with time. Then, as G-actin is depleted, the nucleation rate, which is a high power of the G-actin concentration, drops rapidly. In the absence of fragmentation and annealing, the filaments continue to elongate for a while until the G-actin concentration decreases to the critical concentration, at which the length distribution evolves into a wide and irregular peak (Figure 2.5) dependent on the initial conditions and with an average length on the order of tens of microns, in qualitative agreement with experimental data (Kas *et al.*, 1996).

When fragmentation and annealing are accounted for, however, the evolution of the filament length distribution is markedly different. Fragmentation produces filament

Figure 2.5. Steady state length distributions of simulated actin filaments. Length distributions at steady state (~15-24 hours) are shown for simulations using 3.0 μM initial actin either with or without normal annealing and fragmentation (*black bars* and *gray bars*, respectively). Distributions were averaged from 50 time points taken at 10 minute intervals from ~15-24 hours.



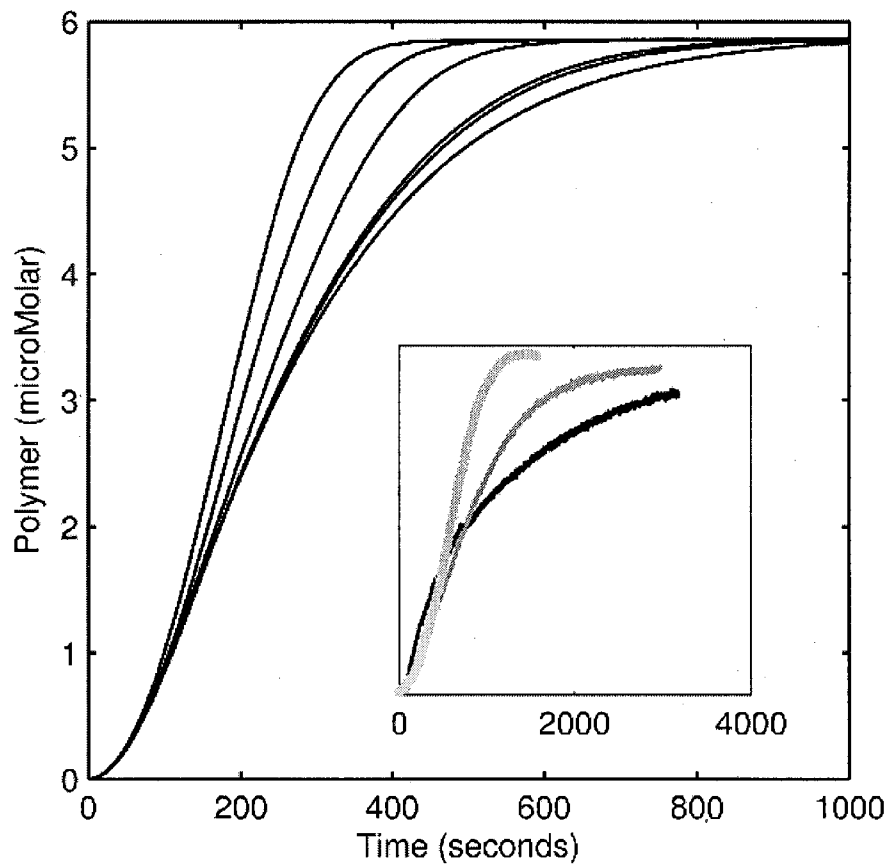
ends rapidly after very little nucleation and growth has occurred. This in turn depletes the G-actin concentration much more rapidly. Thus, the slowing of nucleation occurs almost simultaneously with the onset of significant fragmentation, after which the fragmentation rates increase to fairly constant levels. Annealing event rates increase as the number concentration of filaments increases. This progression depends on the initial free actin concentration, and is more rapid at higher concentrations. Fragmentation reduces the number of long filaments resulting first in a Poisson-like length distribution, and then, as the G-actin concentration reaches the critical concentration, in a stationary exponential distribution (Figure 2.5), in which the average filament length is determined by the balance of fragmentation and annealing and is $\sim 10 \mu\text{m}$ (Figure 2.4B), in qualitative agreement with earlier experiments and approximate calculations (Oosawa and Asakura, 1975; Sept *et al.*, 1999).

Higher fragmentation rates result in faster polymerization kinetics. Recent experimental approaches used labeled actin monomers to visualize filaments (Fujiwara *et al.*, 2002; Kuhn and Pollard, 2005), so there may have been an abnormal level of fragmentation in these studies. Indeed, neither the tetramethylrhodamine (TMR)- nor the Oregon Green (OG)-actin used in these studies can polymerize unless there are unlabeled G-actin monomers present with which they can copolymerize (Kuhn and Pollard, 2005; Kudryashov *et al.*, 2004). TMR-actin and unlabeled actin copolymers have been reported to polymerize faster than pure unlabeled actin, and copolymerization results in shorter filaments (Kudryashov *et al.*, 2004), both presumably due to increased fragmentation of F-actin. In order to simulate the presence of TMR- or OG-actin, we ran simulations in

which the random fragmentation rate constant was increased by factors of 5, 10, 50, 100, and 200, with an initial free actin concentration of 6 μM (to facilitate comparison to the results of Kudryashov *et al.* (Kudryashov *et al.*, 2004). The resulting polymerization time series (Figure 2.6) show that increasing the fragmentation rate advances the polymerization curve and increases the greatest observed polymerization rate. We used these simulations to roughly calibrate against the experimental observations in (Kudryashov *et al.*, 2004), where ~ 8 and $\sim 17\%$ TMR-actin polymerization were advanced with respect to that of pure unlabeled actin (Figure 2.6, inset) to roughly the same degree as simulated actin with 50-, 100-, or 200-fold increased random fragmentation. Note that TMR-labeled actin was also observed to delay the initial nucleation phase by several minutes, suggesting that TMR-actin also affects nucleation (Kudryashov *et al.*, 2004). We did not attempt to reproduce this effect of copolymerization.

Fragmentation and annealing events affect neither nucleotide profiles within filaments, nor barbed ends length excursions. The recently observed high F-actin length diffusivities (Fujiwara *et al.*, 2002; Kuhn and Pollard, 2005) could originate from length changes resulting directly from more frequent fragmentation and annealing events, or indirectly due to increased fragmentation exposing ADP-actin subunits (normally protected by the ATP-actin cap) allowing mini-catastrophes and -rescues of filament ends. In order to investigate the causes of the observed F-actin dynamics, we looked at the composition of the barbed-end terminal subunit(s) under various simulated conditions. First, we explored the dependence of the state of the barbed end-terminal

Figure 2.6. Simulated polymerization curves for various fragmentation rates. All polymerization simulations used 6 μM initial actin. Each curve used the random-fragmentation rate constant (see Table) multiplied by a factor of (from right to left) 1 \times , 5 \times , 10 \times , 50 \times , 100 \times , and 200 \times . *Inset:* Experimental polymerization curves for pure actin (*black*), 1:12 TMR-actin to unlabeled actin (8.3% labeled; *dark gray*), and 1:6 TMR- to unlabeled actin (16.6%; *light gray*). (x-axis is seconds; y-axis is absorbance; raw data for inset provided by Dmitri Kudryashov).



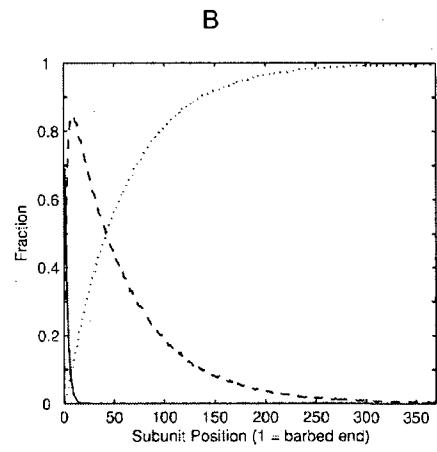
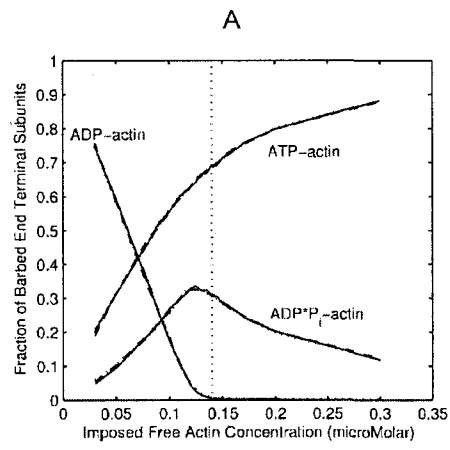
subunit on free actin concentration, by analyzing data from simulations in which constant concentrations ranging from 0.03 μM to 3.0 μM were imposed after a simulation reached the critical concentration. The fraction of terminal subunits in each state did not depend upon the presence of annealing and fragmentation, or a 50-fold increased fragmentation rate (Figure 2.7A). The exposure of ADP-actin at the first subunit is high at sub-critical concentrations, but decreases to almost zero at the critical concentration and above; at a concentration of 0.14 μM the barbed end terminal subunit was ATP-actin 69.1% of the time, ADP·P_i-actin 30.4% of the time, and ADP-actin 0.5% of the time, for simulations with 3.0 μM total actin.

Next, we looked at the composition of the first micrometer (370 subunits) at the barbed end during a period of 30 minutes after the critical concentration was reached (Figure 2.7B). In each of three cases (no annealing or fragmentation, normal fragmentation and annealing, and 50-fold increased fragmentation rate with normal annealing), the fractions of ATP-, ADP·P_i-, and ADP-actin at each position are plotted. The results show that the steady state nucleotide profiles of the first micrometer within filaments, as well as the state of the barbed end-terminal subunit, are unaffected by fragmentation and annealing. These profiles agree roughly with those predicted by Binschadler et al. (Figure 3A,B in Binschadler *et al.*, 2004; note that their parameter set is different than ours) lending further support to the approximate model in (Binschadler *et al.*, 2004).

Finally, we investigated length excursions of the barbed ends by tracking the persistence of subunit losses or gains. Only excursions that ended with a reversal, i.e. subunit addition event after a loss of a few subunits, were counted; excursions ended by

Figure 2.7. Nucleotide states of simulated actin filaments at steady-state.

(A.) State of barbed end terminal subunit under imposed free actin concentrations at steady state. Curves are shown for 5 simulations: one with no annealing or fragmentation (*solid line*), two with normal annealing and fragmentation (*dashed lines*), and two with 50× increased fragmentation rates (*dotted lines*). Vertical line (*dash-dot*) indicates critical concentration (0.14 μM). (B.) Nucleotide-states of the first 370 barbed end terminal subunits at steady state, for 3.0 μM total actin. The fraction of subunits in each nucleotide state averaged across all filaments tracked in the simulation volume. Shown are ATP- (*solid*), ADP·P_i- (*dashed*), and ADP-actin (*dotted*).



an annealing or complete depolymerization event were discarded.

The distribution of length excursions during a period of 30 minutes after the critical concentration was reached is shown for various fragmentation rates (Figure 2.8). The distribution shows that the excursion lengths are distributed exponentially, as is the 'memory-less' dynamic instability phenomenon described in microtubules, but on the average are only a few subunits long, unlike the dynamic instability. The difference between the distributions corresponding to simulations without fragmentation and annealing and various fold-increases in the normal fragmentation rate (up to 200-fold) is very small: the greatest difference, for the frequency of 1 subunit addition/loss, is $\sim 4\%$. The results illustrated in Figures 2.7 and 2.8 suggest that the addition and loss dynamics at the ends of filaments is not greatly altered by the inclusion of normal or even enhanced fragmentation and annealing in simulations.

Simulations yield high diffusivities only if large length changes and higher fragmentation rates are allowed. In order to calculate length diffusivity in a manner similar to the one used in (Fujiwara *et al.*, 2002), we examined simulated length histories in a 30 minute interval soon after the critical concentration was reached (~ 1 hour after simulations were begun). We processed simulation results using a range of detectability limits from $0.5 \mu\text{m}$ (close to the measurement error) to $2 \mu\text{m}$. This limit was, in our opinion, a maximum believable annealing or fragmentation event that could be missed by an experimenter between image acquisitions. Higher detectability limits resulted in higher calculated diffusivities (Figure 2.9). This is to be expected, because analysis of the same length histories with higher detectability limits means that fewer large annealing

Figure 2.8. Lengths of excursions (contiguous loss or gain of subunits) at the barbed ends of filaments. Excursions were measured by tracking the lengths of contiguous subunit losses or gains that were terminated by subunit gain or loss, respectively. Excursions terminated by annealing or complete depolymerization were not included in this analysis. Measurements were made during the period of 4000 to 5800 seconds, from simulations of 3.0 μM initial actin, beginning when the free actin concentration was close to the critical concentration (for the no fragmentation or annealing case) or had reached the critical concentration (all other cases). Curves are shown for no fragmentation or annealing (*solid, filled circles*) and 1 \times , 10 \times , 50 \times , 100 \times , and 200 \times fragmentation rates with normal annealing (*solid/open circles, dashed/closed, dashed/open, dotted/closed, dotted/open, respectively*). The maximum variation among these curves is for excursions of length -1 (3.6%) and +1 (4.1%). Also shown are two curves from simulations with normal annealing and fragmentation in which concentrations of 0.10 (*solid line, small gray circles*) and 0.14 μM (*dashed line, asterisks*) were imposed starting at 3600 seconds. In the simulations, the most frequent barbed end excursion lengths for imposed concentrations of 0.10 and 0.14 μM were between 1 to 4 subunits, and the most frequent excursion durations were between 0.6 and 0.9 seconds. Excursions at the pointed end were roughly the same magnitude, but slower (longer duration).

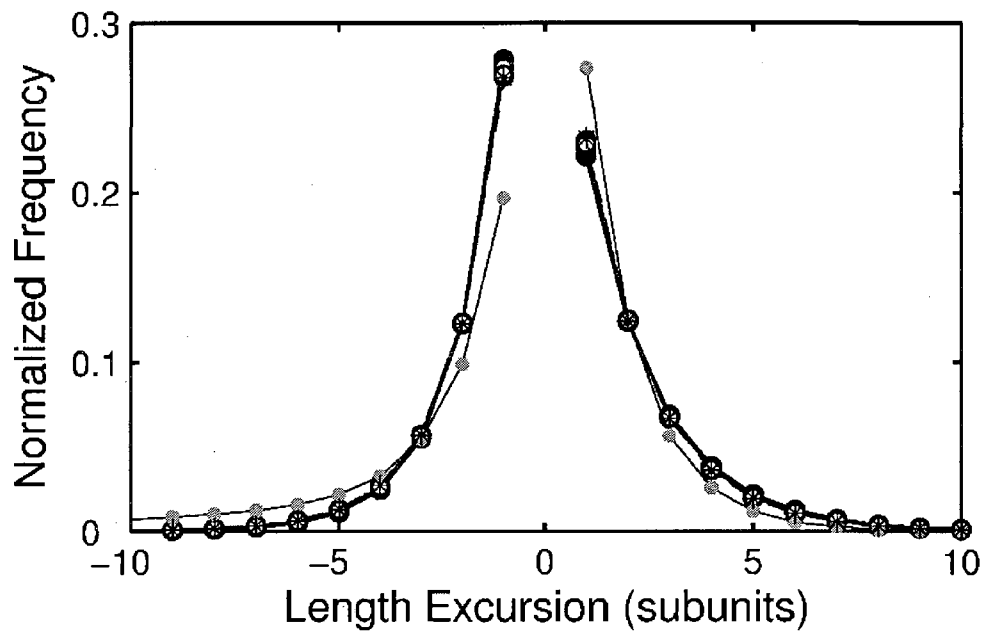
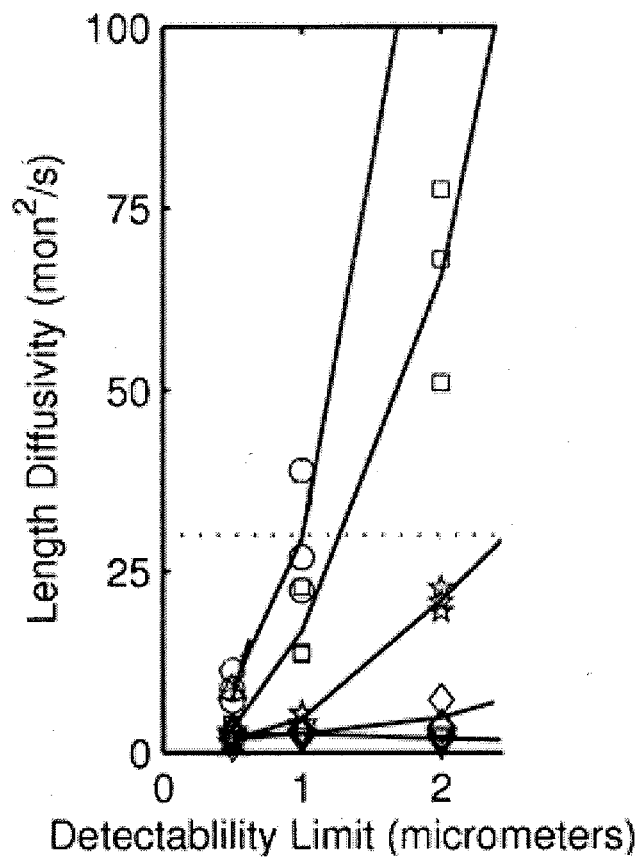


Figure 2.9. Length diffusivities calculated from simulations using various random-fragmentation rates (no fragmentation or annealing, downwards-pointing triangles; normal fragmentation and annealing, diamonds; and normal annealing with increased random fragmentation: 10×, *stars*; 50×, *squares*; 100×, *circles*), analyzed using detectability limits (see text) from 0.5 to 2 μm . Data from three simulation runs for each parameter set are shown (*open symbols*), along with average (*solid lines*).



and fragmentation events are excluded from the calculation of length diffusivity.

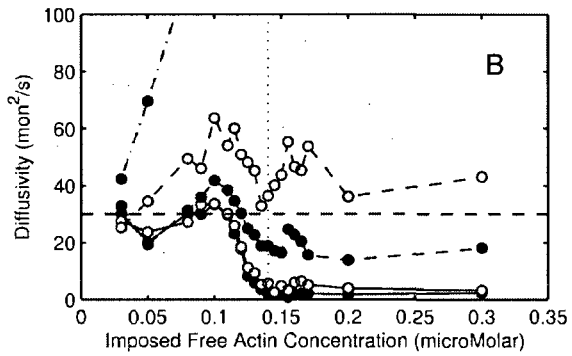
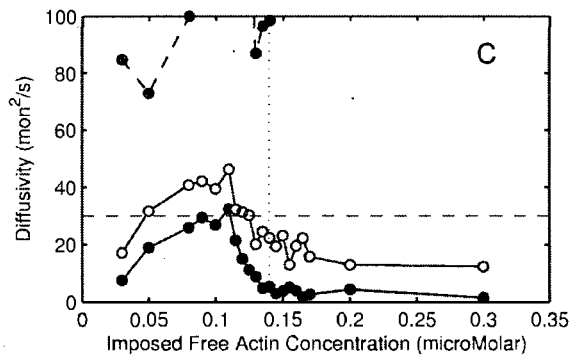
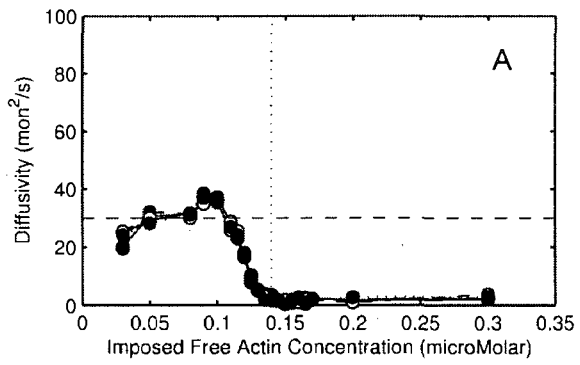
When no annealing or fragmentation was allowed, or at normal level of annealing and fragmentation, the detectability limit had almost no effect on low length diffusivity (Figure 2.9). Thus, normal levels of annealing and fragmentation would not likely account for the high length diffusivities observed experimentally. As argued above, 50- to 200-fold fragmentation rate increases possibly accompanied TMR- or OG-actin assembly in the experiments, so we calculated diffusivities from simulated length histories with increased fragmentation rates (Figure 2.9). High fragmentation rates did not greatly affect the calculated diffusivity at a detectability limit of 0.5 μm , but had large effects at higher detectability limits. The simulations, even at very high detectability limit of 2 μm , cannot explain measured diffusivities above 30 monomers²/s at normal, or ten-fold increased fragmentation rates. The minimum detectability limit which would have to be assumed in order to obtain measured diffusivities above 30 monomers²/s decreases with increasing fragmentation rate is $\sim 1.5 \mu\text{m}$ for 50 \times fragmentation, and $\sim 1 \mu\text{m}$ for 100 \times fragmentation. Thus, only rates of fragmentation increased two orders of magnitude (consistent with the fractions of labeled actin monomers used in both experimental studies) could have led to the high length diffusivities, if it is assumed that experimenters could have missed fragmentation or annealing events on the order of $\sim 1 - 1.5 \mu\text{m}$. We find this very believable because such fragments could appear in or disappear from the plane of focus quite easily between image acquisitions, and the resulting length changes would have been masked by measurement error on the order of 0.5 μm .

Length diffusivity dependence on actin concentration. Because Fujiwara *et al.* used 10% TMR-actin in their studies (Fujiwara *et al.*, 2000), we chose to focus on a 50-fold increase in fragmentation as most representative of the experimental conditions (Figure 2.6). We analyzed the dependence of diffusivity on detectability limit and fragmentation (no fragmentation or annealing, normal fragmentation and annealing, and 50-fold increased random fragmentation rate with normal annealing) at imposed concentrations from 0.03 μM to 0.3 μM (Figure 2.10). With no fragmentation or annealing, there is no dependence on the detectability limit, and diffusivity reaches a peak of 30-40 monomers²/s at around 0.1 μM , and drops back to 1-5 mon²/s at and above the critical concentration (Figure 2.10A). This result is in good agreement with the conclusions of Vavylonis *et al.* (Vavylonis *et al.*, 2005). At normal fragmentation and annealing rates, and 50-fold increased fragmentation rates, diffusivities increase with increasing detectability limits, but largely keep the same dependence on concentration (Figure 2.10B,C).

Discussion

Impressive recent gains in quantitative understanding of actin dynamics are due in no small measure to modeling efforts accompanying experimental studies (Pollard and Borisy, 2003). The most popular approach to modeling is to describe actin populations using differential equations (Pieper and Wegner, 1996; Sept *et al.*, 1999; Bindschadler *et al.*, 2004; Ermentrout and Edelstein-Keshet, 1998). Recently, this approach allowed the prediction of spatial distributions of the nucleotide profiles within filaments (Bindschadler *et al.*, 2004). Earlier, solutions of differential equations describing

Figure 2.10. Length diffusivity versus free actin concentration for 300-600 filament simulations with (A.) no annealing or fragmentation, (B.) normal annealing and fragmentation, and (C.) 50x fragmentation with normal annealing. Curves represent detectability limits of 0.5 μm (*solid, filled circles*), 1.0 μm (*solid, open circles*), 2.0 μm (*dashed, filled circles*).



polymerization and gelsolin-induced fragmentation, but not annealing (Ermentrout and Edelstein-Keshet, 1998), predicted transient peaks in filament length distributions and monotonically decreasing stationary length distributions. There is also rich literature on fragmentation/annealing modeling in non-actin systems (VanDongen and Ernst, 1984; Marques and Cates, 1994), in which both stationary polymer size distributions and temporal transients leading to these distributions were investigated. These efforts were forced to use approximations, and could only follow a finite number of descriptors of a population (e.g. mean and standard deviation of filament lengths). The danger of these approximations is that small changes in the model assumptions can have drastic consequences for the model results (Ermentrout and Edelstein-Keshet, 1998). Stochastic simulations (one of the first such efforts were Monte Carlo-type simulations (VanDongen and Ernst, 1984), on the other hand, can explicitly follow each filament and subunit in a population, but efforts in this area to date have excluded the important processes of fragmentation and annealing (Vavylonis *et al.*, 2005; Dufort and Lumsden, 1993) with the exception of several studies of the combined effects of severing, capping and branching on the critical concentration of actin (Carlsson, 2005; Carlsson, 2006).

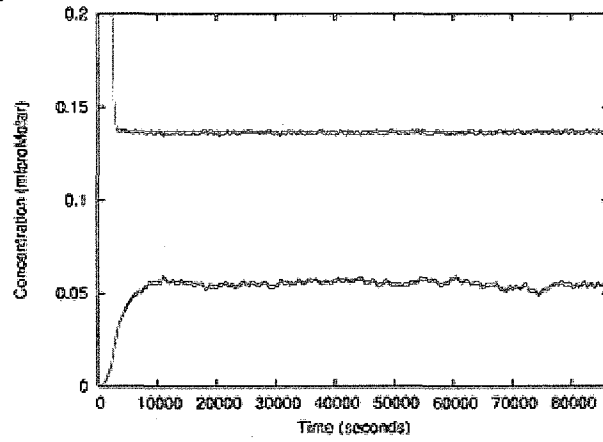
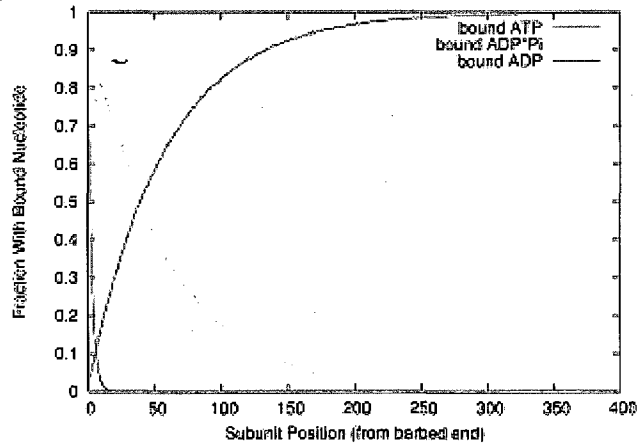
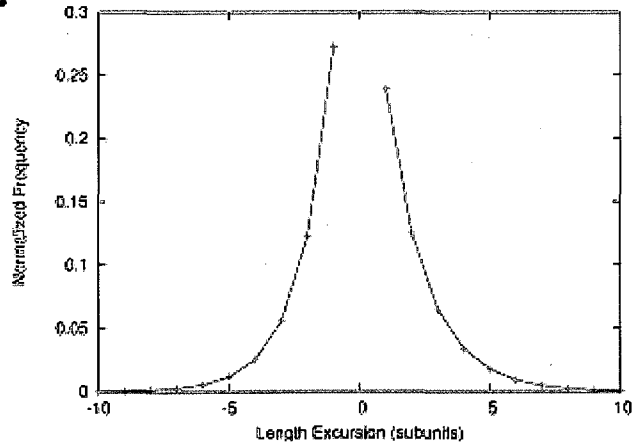
In this study, we used Gillespie's stochastic simulation algorithm in order to simulate F-actin dynamics, including the processes of fragmentation and annealing (Gillespie, 1977). We implemented recent models of fragmentation (Sept *et al.*, 1999) and annealing (Andrianantoandro *et al.*, 2001), in a variable volume stochastic simulation, which allowed rapid simulation of *in vitro* polymerization of purified actin. Nevertheless, several simplifying assumptions were made in order to yield reasonable computation times. The first of these was the assumption that ATP replaces ADP on G-

actin instantaneously; i.e. there is no ADP-G-actin. We were able to run simulations without this simplification, and found that although it affected the critical concentration somewhat, other aspects of filament dynamics and composition were almost completely unaffected (Figure 2.11). The second simplification was using average filament length to calculate fragmentation (random and stress induced) and annealing times. A more realistic approach might be to calculate separate times for each filament (for fragmentation) and pair of filaments (for annealing) based on their individual lengths (Hill, 1983). However, our model was able to closely reproduce data from experiments in which annealing and fragmentation were ostensibly the only events that could occur (Figure 2.3). Since there is no direct empirical data correlating the annealing or fragmentation of individual filaments to their lengths, we feel that our approach is as accurate as possible at this time. Nevertheless, future simulations that do not employ this simplification may be revealing.

One of the advantages of stochastic simulation of individual filaments is that it allows vivid illustration of transient actin dynamics. Our results for polymerization kinetics in the absence of fragmentation/annealing is in a very good qualitative agreement with earlier data and calculations (Cooper *et al.*, 1983; Tobacman and Korn, 1983). We predict that at low fragmentation rates the polymerization kinetics is not affected by fragmentation/annealing. However, at higher fragmentation rates, the polymerization curve is characterized by a more abrupt transition between the growth phase and saturation, in qualitative agreement with earlier studies (Wegner and Savko, 1982; Frieden and Goddette, 1983). Similarly, we observed that fragmentation and annealing have little influence on the nucleotide profiles within filaments, which are similar to those

Figure 2.11. Effects of assuming instantaneous nucleotide exchange on G-actin monomers.

In order to check this assumption, which was used for all results in the main body of the paper, we performed hybrid simulations of stochastic filament-related events (nucleation, subunit addition/loss, annealing, fragmentation) in parallel with numerical solution of differential equations describing nucleotide exchange (ATP for ADP) on G-actin, on novel model results. A rate constant of 0.009 s^{-1} for nucleotide exchange (ATP for ADP) on G-actin was used (5), and the time interval for calculation of concentration changes was 0.01 seconds. (A) Polymerization curve for a $3.0 \text{ }\mu\text{M}$ total actin simulation over 24 hours (86400 seconds); ATP-G-actin (*red line*) and ADP-G-actin (*green line*). The critical concentration was $\sim 0.138 \text{ }\mu\text{M}$, as opposed to $\sim 0.140 \text{ }\mu\text{M}$, and the time course of polymerization was qualitatively similar to those of simulations in which instantaneous exchange of ATP for ADP was assumed (see Figure 2.4A). With instantaneous exchange, ATP-G-actin decreased from 3.0 to less than $0.15 \text{ }\mu\text{M}$ in 51 ± 2 minutes, whereas with hybrid stochastic simulation of filament events and numerical solution of nucleotide turnover (this figure), ATP-G-actin decreased from 3.0 to less than $0.15 \text{ }\mu\text{M}$ in 47 ± 1 minute ($N = 3$ for each type of simulation, mean \pm sem). (B) Distribution of bound nucleotides in the barbed end terminal micrometer. These distributions closely match those from straight stochastic simulations (Figure 2.5B). (C) Length excursions at the barbed end between 4000 and 5800 seconds for $3.0 \text{ }\mu\text{M}$ total actin. The distribution of these growth (positive) and shrinking (negative) excursions appears no different from that for simulations without ADP-G-actin accounted for.

A**B****C**

predicted by a previous model (Bindschadler *et al.*, 2004) that used significant simplifications.

Without fragmentation and annealing, our simulations predict a broad and irregular distribution of filament lengths with an average length of tens of microns, which is in qualitative agreement with the experimental data (Kas *et al.*, 1996; Limozin *et al.*, 2003). Early evolution of the filaments' length distribution derived from our simulations agrees qualitatively with theoretical conclusions of Hu *et al.* (Hu *et al.*, 2006): after early nucleation and initial elongation phases, the length distribution undergoes effective 'diffusive' redistribution of subunits between the filaments for a few hours. The addition of annealing and fragmenting causes a drastic change in the F-actin length distribution, making it exponential, in agreement with earlier data and approximate calculations (Sept *et al.*, 1999). The reason for the exponential distribution at steady state is the balance between the fragmentation of longer filaments and annealing of shorter ones, resulting in a characteristic mean length that is largely independent of the monomer concentration. Our simulations predict a mean length of $\sim 10 \mu\text{m}$ that is very close to experimental observations (Sept *et al.*, 1999).

One of the motivations for this work was recent observation of high length diffusivities by Fujiwara *et al.* and Kuhn and Pollard, surprising because it suggested that accepted mechanisms of F-actin dynamics are incomplete (Fujiwara *et al.*, 2002; Kuhn and Pollard, 2005). Our results indicate that some combinations of high fragmentation rates (i.e. 50-fold higher or more, which is plausibly a consequence of the use of labeled actin) and high detectability limits (i.e. 1 - 1.5 μm , which is plausibly due to the limits of resolution and the lack of continuous image capture) may explain high observed F-actin

length diffusivity. The simulations show that these recent observations are not inconsistent with random hydrolysis and phosphate release and may be a direct result of annealing and fragmentation of short fragments, rather than enhanced exposure of ADP-actin in filaments.

The remaining issue, however, is why such high fragmentation rates were not observed directly in the experiments on length diffusivity, and how likely high detectability limits are. It is also not clear how likely the simultaneous occurrence and congruence of high fragmentation rates and high detectability limits is. Our simulations merely indicate quantitatively the conditions under which the experimental results could be explained by the combination of experimental error, fragmentation and annealing. If these conditions are not met, the search for the explanation would have to expand.

Further complexities in actin dynamics may also affect length diffusivity. For example, some evidence suggests that actin subunits undergo conformational changes over a period of minutes to hours following polymerization that increase the local stability of the filament (Orlova *et al.*, 2004). Such stabilization would bias fragmentation events towards the barbed end in polymerizing or treadmilling populations, thereby increasing the frequency of short (e.g. $< 1 \mu\text{m}$) length changes, which could also account for some portion of high observed length diffusivities. This example illustrates the utility of combining modeling and experimentation approaches, as future studies could predict the degree to which standard models of actin dynamics might be inaccurate, as the experimental data to both suggest and verify inaccuracies becomes available.

Chapter 3

Growth cone-like waves transport actin and promote axonogenesis and neurite branching

Preface and Acknowledgement

Work presented in this chapter was published in *Developmental Neurobiology* (Flynn *et al.*, 2009). The order and list of authors include: Kevin C. Flynn (KCF), Chi W. Pak (CWP), Alisa E. Shaw (AES), Frank Bradke (FB), and James R. Bamberg (JRB). My contributions to the publication demonstrated that waves represent a *bona fide* mechanism of actin transport, which was accomplished in part by determining quantitative differences in the fluorescence-decay profile and spatial distribution of photo-converted Dendra-actin in waves versus non-wave regions (neurites without a wave). Results from these two modes of analyses, which were derived from 1-D diffusional analysis, strongly suggest that actin is transported by simple-diffusion in non-wave regions. In contrast, actin is retained in waves and is translocated with the wave even as the wave moves. Altogether, our results suggest that waves are able to deliver a bolus of actin and other growth-promoting factors to the growth cone, and thereby stimulate pulsatile neurite outgrowth.

This work was supported by the National Institute of Health (NS40371, DK69408, (JRB), NS48660 (KCF), the Max Planck Society, and the Deutsche Forschungsgemeinschaft Grant SFB 391 (FB). We thank Barbara Bernstein and Laurie Minamide for technical assistance and helpful suggestions with experiments. We also extend gratitude to O'Neil Wiggan, Boyan Garvalov, Christian Gonzalez-Billault,

Michael Tamkun, Stuart Tobet, Kathryn Partin, Mike Maloney, Janel Funk, Richard Davis, Shay Perea-Boettcher, and Bechara Kachar for helpful discussions. The Thy1-YFP mice used in this study were kindly supplied by Kristy McClellan and Stuart Tobet.

Abstract

Axonogenesis involves a shift from uniform delivery of materials to all neurites to preferential delivery to the putative axon, supporting its more rapid extension. Waves, growth cone-like structures that propagate down the length of neurites, were shown previously to correlate with neurite growth in dissociated cultured hippocampal neurons. Waves are similar to growth cones in their structure, composition and dynamics. Here, we report that waves form in all undifferentiated neurites, but occur more frequently in the future axon during initial neuronal polarization. Moreover, wave frequency and their impact on neurite growth are altered in neurons treated with stimuli that enhance axonogenesis. Coincident with wave arrival, growth cones enlarge and undergo a marked increase in dynamics. Through their engorgement of filopodia along the neurite shaft, waves can induce de novo neurite branching. Actin in waves maintains much of its cohesiveness during transport whereas actin in non-wave regions of the neurite rapidly diffuses as measured by live cell imaging of photoactivated GFP-actin and photoconversion of Dendra-actin. Thus, waves represent an alternative axonal transport mechanism for actin. Waves also occur in neurons in organotypic hippocampal slices where they propagate along neurites in the dentate gyrus and the CA regions and induce branching. Taken together, our results indicate that waves are physiologically relevant

and contribute to axon growth and branching via the transport of actin and by increasing growth cone dynamics.

Introduction

After terminal differentiation, neurons form neurites which then grow, arborize, and respond to environmental cues to form complex synaptic connections. The extending neurites are initially similar, but then acquire different identities becoming either axons or dendrites during polarization, which is necessary to neuronal function. Cultured hippocampal neurons have served as a model for many aspects of development including axon specification and branching (Craig and Banker, 1994; da Silva and Dotti, 2002). Axon specification involves cytoskeletal reorganization (Witte and Bradke, 2008), as well as the regulation of intracellular transport (Horton and Ehlers, 2003). Prior to axon formation, in what are known as stage 2 hippocampal neurons, transport is relatively uniform in all processes. Later, during the stage 2-3 transition in which axon specification and growth occur, there is an asymmetric increase in anterograde transport into the presumptive axon (Bradke and Dotti, 1997). This increase in transport is reflected by an engorgement and increased dynamics of the growth cone of the emergent axon (Bradke and Dotti, 1997, 1999; Kunda *et al.*, 2001). Accumulating in the presumptive axon are proteins that impact the development of neuronal polarity including many cytoskeletal regulators (Shi *et al.*, 2003; Schwamborn and Puschel, 2004; Inagaki *et al.*, 2001; Garvalov *et al.*, 2007). A general increase in transport could contribute to the increased levels of these proteins in the axon; however, other mechanisms such as selective

degradation of proteins in minor processes (Schwamborn *et al.*, 2007) and selective association with axon-specific kinesin motors (Jacobson *et al.*, 2006) are also at work. In hippocampal neurons, axons as well as dendrites undergo periodic extension and retraction. Ruthel and Banker (1998, 1999) initially identified and characterized another periodic phenomenon that they called “waves” which could underlie, at least partially, the pulsatile outgrowth. Waves appear similar to growth cones, often originate at the soma, travel down the length of axons and dendrites, and are associated with spurts of outgrowth. Waves travel at a speed consistent with slow component b (SCb) of axonal transport ($\sim 3 \mu\text{m}/\text{min}$), which carries actin and actin associated proteins and which may be rate limiting for neurite growth (Wujek and Lasek, 1983; McQuarrie and Jacob, 1991). Thus waves may represent one mechanism to supply growth cones with actin as well as other growth promoting proteins.

Here we use live-cell imaging to characterize wave behavior and effects on neuronal development. We confirm that waves are indeed similar to growth cones. Waves occur in all processes in stage 2 neurons but become more frequent in presumptive axons during the stage 2-3 transition and their prevalence increases with treatments that enhance axonogenesis. Waves deliver actin and associated proteins to growth cones or to filopodia along the neurite shaft, which are often associated with neurite growth and filopodial engorgement to create neurite branches, respectively. Waves occur in organotypic hippocampal slices, demonstrating that they can contribute to growth in a relevant physiological setting. The implications from these results are that waves contribute to neuronal branching and axon growth.

Materials and Methods

Neuronal Cell Culture: Rat and mouse hippocampal neurons were dissected at day E18 and E16.5, respectively, and either used directly in experiments or frozen as previously described (Mattson and Kater, 1988; Garvalov *et al.*, 2007). Neurons were cultured on poly-d-lysine (Sigma) coated glass coverslips in either neurobasal (Gibco) supplemented with B-27 (Invitrogen, San Diego, CA) and glutamine (Minamide *et al.*, 2000) or in glial conditioned N2 medium as previously described (de Hoop, 1998). The myosin II inhibitor, blebbistatin (Sigma Aldrich) was dissolved in DMSO at 100 mM and applied to neuronal cultures at a final concentration of 2.5 μ M. For long-term cultures, blebbistatin was added to growth medium 16 h after plating through the termination of the experiment. In some experiments neurons were plated on mixed poly-d-lysine-laminin (10mg/ml) substrate.

Adenoviral Infections: Replication deficient adenoviruses were produced (Minamide *et al.*, 2003) for transgene expression in neuronal cultures essentially as described (Garvalov *et al.*, 2007). The viruses used in these studies include wild-type and nonphosphorylatable (active, S3A) human cofilin constructs fused to monomeric Red Fluorescent protein (mRFP; Campbell *et al.*, 2002). An adenovirus containing the neuron-specific enolase promoter (NSE; Forss-Petter *et al.*, 1990) driving cofilin expression was also used for live-cell imaging experiments. Beta-actin fused at its C-terminus to mRFP, GFP, a photo-activable (pa) GFP (kind gift of Jennifer Lippincott-

Schwartz, National Institute of Health) or the green-to-red photo-convertible(pc)-Dendra protein (kind gift of Michael Tamkun) were also used to visualize actin in live cells. Adenoviral mediated expression of hippocampal slice preparations were performed as previously. Slices were prepared for time-lapse imaging 2-4 days post-infection (see below).

Immunocytochemistry: Fixation, blocking and immunostaining were performed essentially as previously described (Garvalov *et al.*, 2007). All neurons were fixed 30 min at 37°C in 4% paraformaldehyde in cytoskeletal preservation buffer (10 mM MES pH 6.1, 138 mM KCl, 3 mM MgCl₂, 10 mM EGTA, and 0.32 M sucrose). After blocking, immunostaining was performed with the following primary antibodies: Tau1 (1:1000; Chemicon), β -tubulin (1:300; Sigma), Rap1 (1:250; BD Biosciences), Gap43 (1:300; De la Monte *et al.*, 1989), and cdc42 (1:250; Santa Cruz Biotech), total cofilin (MAb22; 14.8 μ g/ml, Abe *et al.*, 1989) and for phospho-cofilin (1.1 μ g/ml, Meberg *et al.*, 1998). IgG secondary antibodies (Molecular Probes, Eugene, Oregon) used were Fluorescein goat anti-mouse IgG, Texas Red goat anti-rabbit, Alexa 650 goat anti-mouse and Alexa 350 goat anti-mouse (all at 1:400). Texas Red- or Alexa 488-conjugated phalloidin (1:200) was used to visualize actin filaments. Coverslips were mounted with Prolong Anti-fade (Molecular Probes). Images were acquired with a Nikon (Tokyo, Japan) Diaphot inverted microscope using 20X air (0.75 NA), 40x oil (1.3 NA) and 60X oil (1.4 NA) objectives and a Coolsnap ES CCD camera (Roper Scientific, Tucson, AZ). Metamorph software (Universal Imaging, Westchester, PA) was used for image acquisition and analysis.

Organotypic hippocampal slice cultures: Organotypic hippocampal slice cultures were performed on postnatal day 0 to 5 Sprague-Dawley rat pups or Thy1-YFP mouse pups (line H; (Feng *et al.*, 2000); Jackson Laboratory) as previously described (Davis *et al.*, 2009). In some cases, small Dil crystals (Invitrogen-Molecular Probes) were placed in the hilus region of the dentate gyrus as described (Dailey *et al.*, 1994), resulting in labeling of cells in the dentate gyrus as well as mossy fiber tracts. Slices were incubated for 3-48 h at 35° C prior to fixation or live-cell microscopy.

Live-cell microscopy: Live-cell microscopy was performed on an Olympus IX81 microscope equipped with a Yokogawa CSU22 spinning disk confocal head, AOTF and an EM-CCD cascade II camera (Photometrics). Diode lasers with 473 nm and 561 nm peak wavelengths were used for GFP and RFP excitation, respectively. DIC images were captured with an HQII camera. The objectives used include: 10x (0.3 NA), 20x (0.17 NA) air objectives, 40X DIC (1.35 NA), and 60x (1.42 NA) oil objectives. Computer controlled acquisition was performed with Slidebook Software (Intelligent Imaging Innovations, Denver, CO). For some experiments a phase contrast objective on the heated stage of a Nikon Diaphot microscope equipped with a Metamorph controlled CCD camera was used.

Time-lapse imaging for analysis of wave effects on neuronal development was performed either in glass bottom T-25 flasks or 35 mm dishes (German glass coverslips sealed with aquarium sealant). E16.5 mouse hippocampal neurons were cultured in neurobasal medium and pH equilibrated in a 5% CO₂ incubator prior to imaging. The 35 mm dishes were used in a humidified, CO₂ regulated system at 37°C. For long-term

experiments, images were acquired every 2.5-5 min. For short-term experiments, images were acquired every 10 s. Fluorescence image acquisition parameters varied depending on the particular experiment and were empirically determined to balance signal intensity and minimize cellular toxicity. In some cases neutral density filters were used to decrease excitation energy.

Adenovirally expressed photo-activatable(pa)-GFP or photo-convertible(pc)-Dendra (Gurskaya *et al.*, 2006) fused to β -actin was activated 3 days postinfection with a computer-controlled Hg light source (405 nm) under control of the Mosaic Digital Diaphragm system (Photonics Instruments). For pa-GFP- β -actin, waves were identified using bright field optics and a selected region encompassing the wave was photo-activated for 1s. Confocal images at 473 nm excitation were then acquired at 30-60 s intervals. In neurons expressing Dendra- β -actin, waves were identified by green fluorescence (473 nm). A region of the neurite with or without a wave was targeted with the Mosaic FRAP-system and photo-converted (400 ms). Following photo-conversion, images were captured using 561 nm excitation (500 ms) at 5-, 20-, or 60-second intervals. Before photo-conversion, an image using 473 nm excitation was captured to show the region of the neuron targeted. Though the first frames of the 561 nm time-series are marked "0-sec post-conversion", it is actually delayed by ~10 s because of the operational delay in switching between imaging modes. Line-scans were made in Metamorph by manually drawing a one pixel-wide line (approximately 200 pixels long) through the targeted neurite and the intensity profiles were exported to Excel. Peak of fluorescence decay curves were made by manually drawing a one pixel-wide line that

spanned the length of the original targeted boxed region and the average intensity values were exported to Excel. Curve-fitting using an exponential equation was done in Excel. For live-cell imaging of hippocampal slices, an area of the membrane with one to three slices adhered was excised and placed slice-side down on a glass bottomed 35 mm dish. The slice was stabilized with a plasma clot made by mixing 20 μ l chicken plasma with 6 μ l thrombin. After clot formation, 400-500 μ l of slice medium was added, completely submerging the slices. Diode lasers (561 nm and 473 nm) were used for fluorescence imaging of DiI and Thy1-YFP labeled neurons, respectively. Growing neurites and dynamic growth cones were maintained in slices for >24 h. In some cases images were analyzed using Metamorph software.

Morphological analysis of growth cones and waves: Growth cone and wave dynamics were measured from time-lapse DIC images from which was calculated the change in area every ten seconds ($\Delta A/10s$) (Endo *et al.*, 2003) by superimposing adjacent images from an image stack using Metamorph software. The average change in area from a sequence of 10 images was used for each growth cone and wave. Growth cones were characterized as inactive (<12% $\Delta A/10s$) or active ($\geq 12\%$ $\Delta A/10s$).

Axons were defined as being $\geq 80\mu m$ in length and containing intermediate to high levels of Tau1 immunofluorescence (Schwamborn and Puschel, 2004; Jiang *et al.*, 2005). Neurites with an absence of Tau1 staining were not counted as axons regardless of length. Neurons were counted with multiple axons when they displayed two or more neurites $\geq 80\mu m$ in length that immunostained for Tau1. Waves were defined in fixed specimens as F-actin rich growth cone-like structures with filopodial and/or lamellipodial

features. From our live-cell imaging experiments we observed that the majority (>80%) of such structures were waves. Branches were defined as protrusions off of the primary neurite that were $\geq 20 \mu\text{m}$.

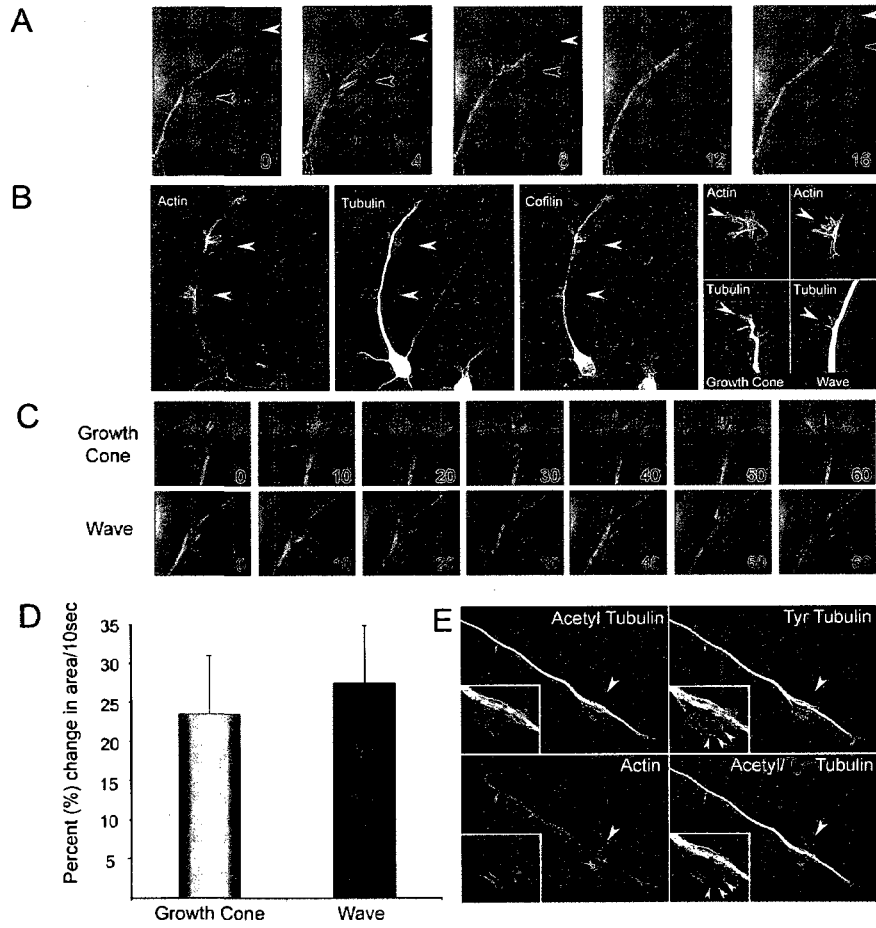
Axon formation is defined as the moment when one neurite reaches $\geq 80 \mu\text{m}$ in length and is at least twice as long as the next longest neurite. Measurements of wave frequency were taken over three four hour intervals: stage 2, stage 2-3 and stage 3. For the stage 2-3 transition the 4 h flanking (2 h before and 2 h after) axon formation was used for analysis. Neurite growth measurements after wave arrival were performed using Metamorph imaging software. Bursts of outgrowth were measured from the position of growth cone tips immediately before to 10 min following wave arrival.

Results

Molecular composition and dynamics of waves. We confirmed the observations of waves reported by Ruthel and Banker (1998, 1999) including their growth cone-like morphology, velocity, and effects on outgrowth when they arrived at the distal neurite (Figure 3.1). In cases where waves consolidate into the neurite shaft they were not associated with bursts of neurite growth. To further quantify the behavioral similarity between waves and growth cones, we compared their motility by live-cell DIC time-lapse imaging (Figure 3.1C, D). Total area changes per 10 s intervals are similar between growth cones and waves. We also examined waves for microtubule organization (Figure 3.1B) and for the presence of tyrosine-tubulin and acetylated-tubulin, which represent newly assembled microtubules and stable microtubules respectively (Figure 3.1E). The tips of the microtubules that splay out from the bundles in the neurite contain tyr-tubulin,

Figure 3.1. Waves have growth cone-like characteristics and propagate along the lengths of neurites.

(A.) DIC images of a wave (black arrowhead) advancing down a neurite shaft. Note that as the wave approaches the distal neurite, the growth cone (white arrowhead) retracts and then engorges and advances following wave arrival. Relative times in min are indicated in lower right corner. (B.) Fluorescent images of F-actin (phalloidin), tubulin, and cofilin in a hippocampal neuron with two waves (arrowheads). Note the high levels of F-actin and cofilin and the splaying of microtubules in the waves. Magnified views of a growth cone and a wave are shown in the right panel. Note the similar features including filopodia, lamellipodia and splaying microtubules. (C.) DIC time-lapse images (10 s intervals) of growth cone (top panel) and wave (bottom panel), which both contain dynamic filopodial and lamellipodial protrusions. Relative times are shown in seconds in the lower right of the images. (D.) Quantification of change in growth cone and wave area over ten second intervals ($\Delta A/10s$) indicates that growth cones and waves have similar dynamics. Growth cones show $23.5 \pm 7.5\%$ $\Delta A/10s$ and waves show $27.5 \pm 7.3\%$ $\Delta A/10s$ (non-significant difference (ns)). (E.) Wave (arrowhead) stained for acetylated and tyrosinated tubulin and phalloidin stainable F-actin. Insets show higher magnification of wave region. Color image is overlay of acetylated and tyrosinated tubulin.



demonstrating that they are actively growing, whereas the microtubules in the neurite shaft are predominantly acetylated (stable) microtubules.

In addition to actin, cortactin and GAP-43 previously shown to be in waves (Ruthel and Banker, 1998, 1999), we identified other normal constituents of growth cones including the Rho GTPases Rap1B, cdc42 and Rac1 (Kunda *et al.*, 2001; Schwamborn and Puschel, 2004), ADF/cofilin (Garvalov *et al.*, 2007), Arp3 (Strasser *et al.*, 2004), slingshot (Abe *et al.*, 2003), and LIM kinase 1 (Rosso *et al.*, 2004) (Figure 3.2). In addition, waves are enriched in tetanus insensitive vesicle associated protein (TI-VAMP)-containing vesicles, suggesting that waves are sites of membrane addition which may be crucial for neurite growth (Alberts *et al.*, 2006). Taken together, these data confirm that waves are growth cone-like structures in their composition, cytoskeletal organization and dynamics.

Wave frequency and impact on growth cones during axonogenesis. Waves have not been studied in relation to axonogenesis during the stage 2 to 3 transition (axonogenesis--see definition in materials and methods). By time lapse imaging of individual neurons maturing from stage 2 to stage 3, the neurite that develops into the axon can be identified. Movies can be examined at earlier stages to identify waves in all neurites, quantify their frequency, and determine how they impacted axon development. Although waves occur in multiple neurites in stage 2, they occur more frequently in the neurite that later develops into the axon (Figure 3.3B). However, at this developmental stage the impact of waves on transient neurite elongation is essentially the same for all minor processes (Figure 3.3B). During the stage 2-3 transition, wave frequency increases

Figure 3.2. Proteins associated with axon growth localize to waves. Immunofluorescence localization of positive regulators of axon growth to waves in cultured hippocampal neurons. Waves are indicated by a white arrowhead and distal neurite tips are indicated by a gray arrowhead. The ADF/cofilin regulatory proteins, slingshot phosphatase 1L (SSH) and Lim kinase 1 (LIMK), co-localize to waves (top row, left two panels). Growth-Associated Protein 43 (GAP 43) co-localizes with cofilin in waves (second row, left 2 panels) as does the Rho GTPase, Rap1 (third row, left 2 panels). Another Rho GTPase essential for normal axon formation, cdc42, co-localizes with actin in waves (bottom row). The actin regulatory proteins, Rac1, cortactin and Arp3 also localize to waves.

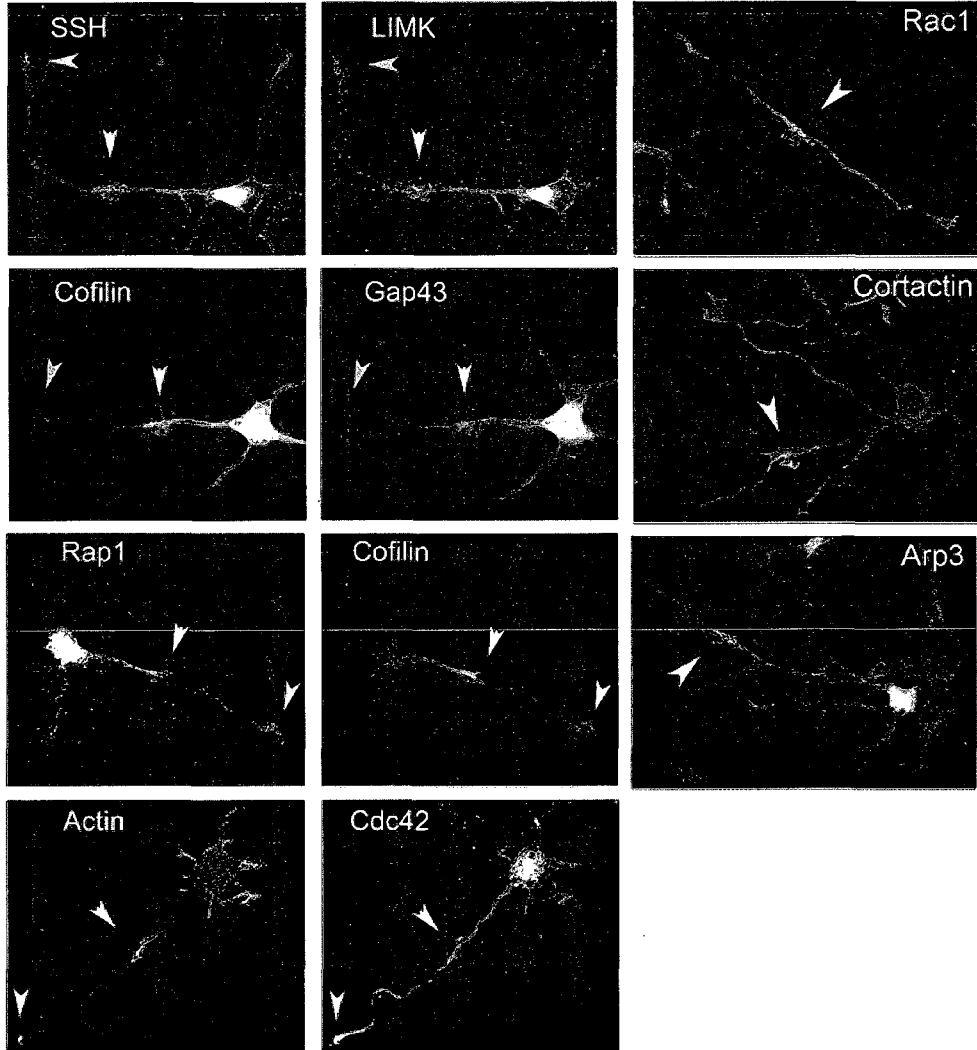
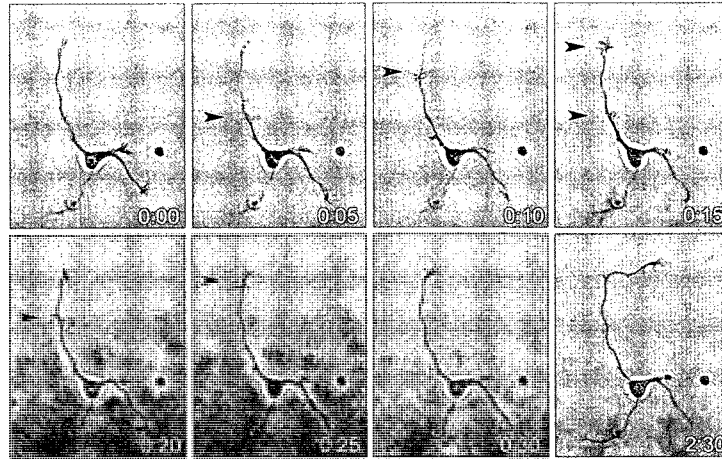


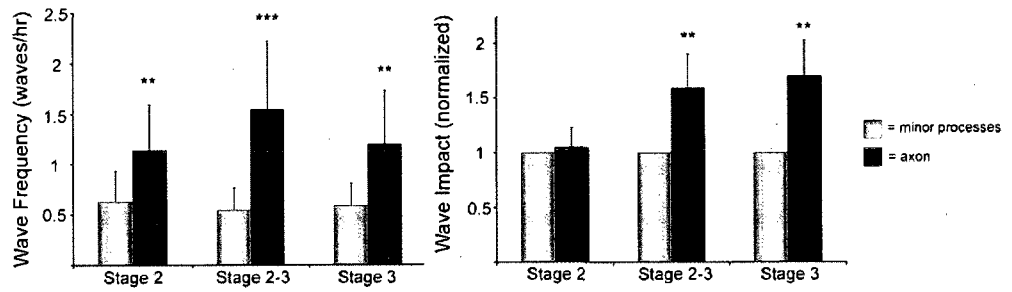
Figure 3.3. Waves are associated with axonogenesis.

(A.) Phase images of waves in stage 2-3 neurons. Multiple waves occur in the developing axon (arrowheads). Time shown is in h:min. (B.) Quantification of the frequency and impact of anterograde waves in neurites of stage 2, stage 2-3 and stage 3 neurons (see definition in methods) followed for 24-72 h. Wave frequency increases in the developing axon during the stage 2-3 transition. During stage 2, the neurite destined to become the axon averages 1.14 ± 0.45 waves/h and minor neurites average 0.63 ± 0.31 waves/h. During the stage 2-3 transition, the developing axon averages 1.55 ± 0.67 waves/h while the minor neurites average 0.55 ± 0.22 waves/h. During stage 3, the newly formed axon averages 1.2 ± 0.53 waves/h while the minor neurites average 0.59 ± 0.22 waves/h. Significance is indicated for axon compared to minor processes: ** $p < 0.01$; *** $p < 0.005$. (n= 10 neurons, Error bars = sd). The impact of waves to bursts of neurite outgrowth is different for developing axons and minor processes and varies at different stages. During the stage 2-3 transition the impact of waves on neurite growth is greater in the developing axon compared to the minor processes (1.5 ± 0.2 fold greater). During stage 3 the relative contribution of waves to neurite growth remains high in the axon compared to the minor processes (1.7 ± 0.3 fold greater). Significance is indicated for axon compared to minor processes: ** $p < 0.01$ (n=6 neurons, Error bars = sd). (C.) Neurite branch formation. The bottom row of images shows magnified views of the branch point in the images above. Time shown is min. A small filopodia protruding from the shaft before wave arrival (arrowhead, bottom row) undergoes engorgement upon wave arrival (0:05 min) inducing the subsequent elongation of a new branch.

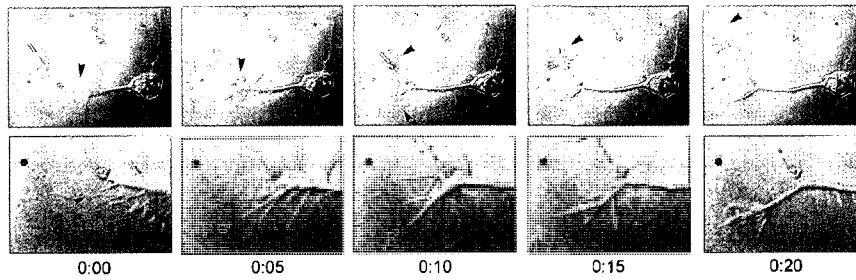
A



B



C



2.8 fold in the developing axon over that occurring in the minor neurites (Figure 3.3B). Furthermore, waves that arrive at the growth cones of the developing axon increase outgrowth by 1.5 fold that of the minor neurites. The frequency and impact of waves on axon outgrowth continues in young stage 3 neurons (Figure 3.3B). Most neurons (>80%) undergoing axonogenesis generate waves. To conclude, waves are more frequent in the developing axon and are associated with bursts of neurite outgrowth, perhaps providing an alternative mechanism for material delivery to the growth cone.

Waves and branching. A fundamental aspect of the wiring of the mammalian brain is neuronal branching, with individual neurons often making connections to multiple target cells. For example, *in vivo*, CA3 pyramidal neurons have axons that branch forming Schaffer collaterals that innervate the CA1 region as well as collaterals connecting with the dentate gyrus (Gomez-Di Cesare *et al.*, 1997). In our live-cell imaging experiments, we not only observed waves that can traverse existing neurite branches (Ruthel and Banker, 1999), but also observed waves initiating nascent neurite branches. In these cases, a wave arrives at a region of the neurite shaft where a filopodium protrudes and causes elongation and engorgement of this filopodium, giving rise to a new branch point (Figure 3.3C). These new branches are persistent and are maintained in culture for the time period of our observations (up to 24 hours). At other sites where waves terminate along the neurite shaft, we observed persistent increases of neurite caliber. The propagation of multiple waves in tandem also influences neurite branch formation and growth.

Cofilin modulates the prevalence of waves. We next examined the effects of cytoskeleton regulators on waves that are known to influence growth cone dynamics and axon growth. Cofilin positively regulates growth cone dynamics (Endo *et al.*, 2003) and has recently been shown to positively impact axon formation (Garvalov *et al.*, 2007). We found a high ratio of active cofilin in waves, similar to levels observed in the growth cones of developing axons (Figure 3.4A). Furthermore, an increased percentage of neurons over-expressing either wild-type or the non-phosphorylatable (S3A) active cofilin have wave-like structures compared to control neurons or those expressing the inactive (pseudophosphorylated) S3E mutant (Figure 3.4B, C).

Inhibiting myosin or growth on laminin enhances axonogenesis, branching and waves. Myosin II modulates growth cone motility and at least a portion of F-actin retrograde flow in neuronal growth cones (Bridgman *et al.*, 2001) and is antagonistic to neurite growth in dorsal root ganglion neurons (Gallo *et al.*, 2002) and axon formation in hippocampal neurons (Kim and Chang, 2004). Therefore, we examined the effects on wave formation of the specific myosin II inhibitor blebbistatin, which enhances neurite length and arborization in hippocampal neurons (Figure 3.5A). The addition of 2.5 μ M blebbistatin induces the formation of supernumerary axons (Figure 3.5B) and greatly enhances axon branching (Figure 3.5C). Neurons treated with blebbistatin showed a ~20% increase in the percent of neurons with wave-like structures (Figure 3.5D). Live-cell imaging experiments (Figure 3.6A) corroborated this finding, with wave frequency increasing 22% in the same neurons after blebbistatin addition (Figure 3.6B). Furthermore, the impact of waves on neurite growth is modulated with myosin inhibition.

Figure 3.4. Cofilin activity may be involved in wave propagation.

(A.) The ratio of total cofilin/phospho-cofilin (pseudocolor intensity profile) shows the relative distribution of dephosphorylated (putatively active) cofilin. Waves (arrowhead) have a high level of dephosphorylated cofilin, similar to that observed in the growth cone periphery. (B.) Hippocampal neurons expressing RFP (top row- control infected), Cofwt (second row) and CofA3 (third row). F-actin was stained with Alexa-phalloidin (green) and neurons expressing Cofwt and CofA3 were also stained for Tau1 (red). Note that the neurons expressing Cofwt and CofA3 have longer axons and more wave-like structures (arrowheads). (C.) Expression of either wild type (wt) or active (A3) cofilin, but not the inactive pseudophosphorylated (E3) cofilin enhances wave formation in neurons by $48.1 \pm 7.4\%$ ($*p < 0.05$) and $48.8 \pm 10.8\%$ (ns), respectively (n=3 separate experiments, >75 neurons for each condition).

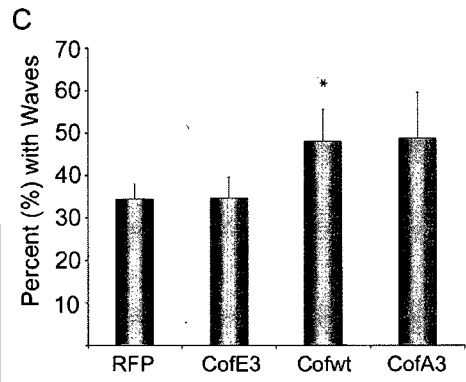
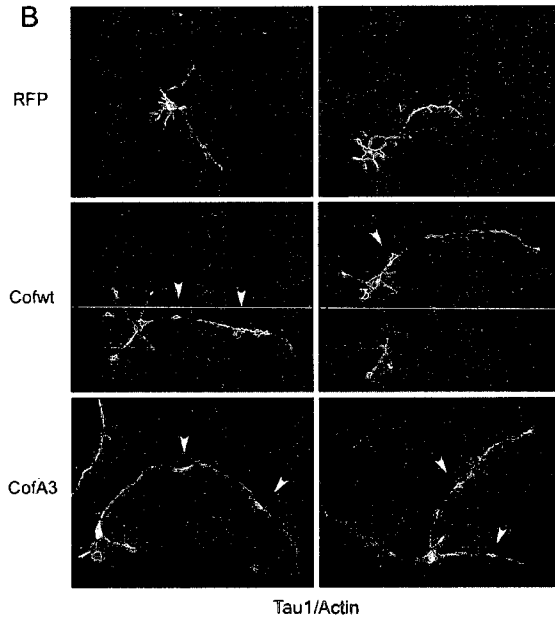
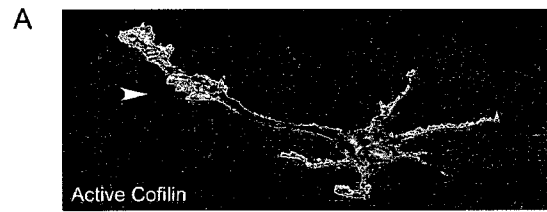


Figure 3.5. Inhibition of myosin II enhances axonogenesis, neurite branching and increases the prevalence of wave-like structures.

(A.) Control neurons (left) and those treated with the myosin II inhibitor blebbistatin (right) were stained for the axonal marker Tau1 (red) and for F-actin with Alexa-phalloidin. Blebbistatin-treated neurons have longer axons and more extensive neuritic arbors. Many blebbistatin-treated neurons have multiple long axons (right). Wave-like structures are highlighted by arrowheads. (B.) Quantification of neuronal polarity phenotypes under different culture conditions (n = 3 separate experiments, >125 neurons). Neurons treated with 2.5 μ M blebbistatin have 8.4 \pm 3.3% with no axon compared to 24.8 \pm 2.2% in controls (**p<0.005), 52.6 \pm 6.8% with one axon compared to 69.1 \pm 1.6% for controls, and 39.0 \pm 9.8% with multiple axons compared to 6.1 \pm 1.3% for controls (**p<0.01). (C.) Quantification of neurite branches. Control neurons average 0.48 \pm 0.1 branches/neuron whereas blebbistatin-treated neurons have an average of 1.56 \pm 0.45 branches/neuron (*p<0.05). D. Neurons exhibiting wavelike structures increase 1.46 fold when treated with blebbistatin (**p<0.01).

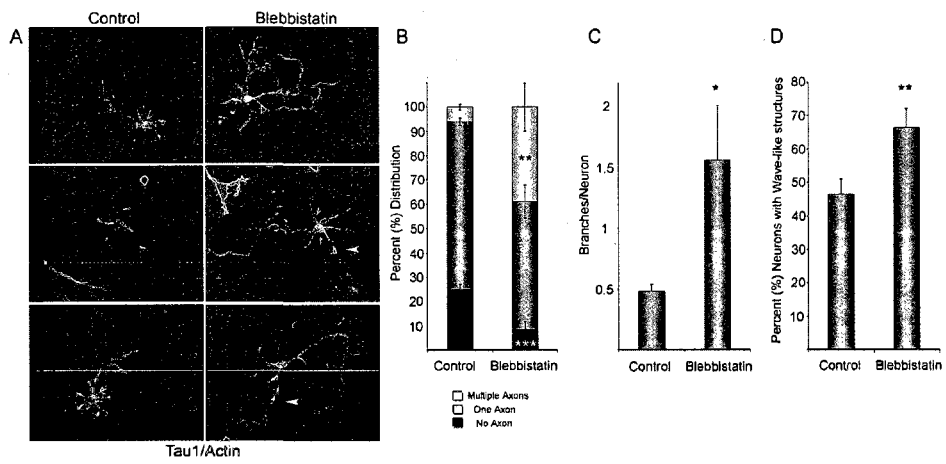
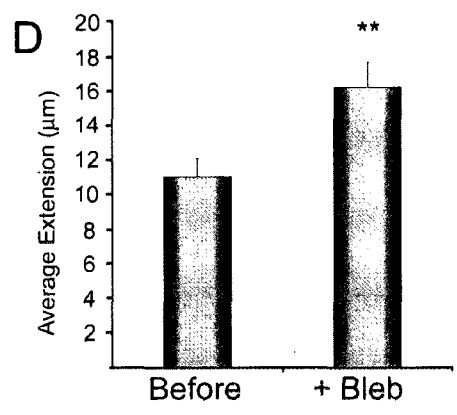
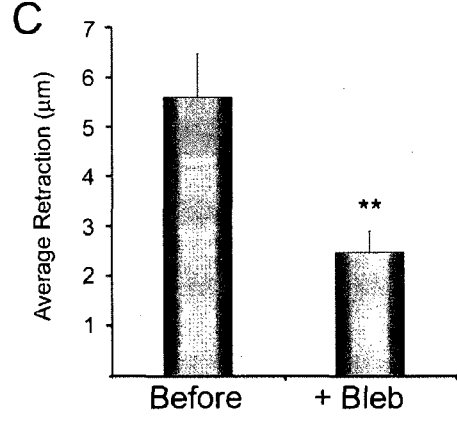
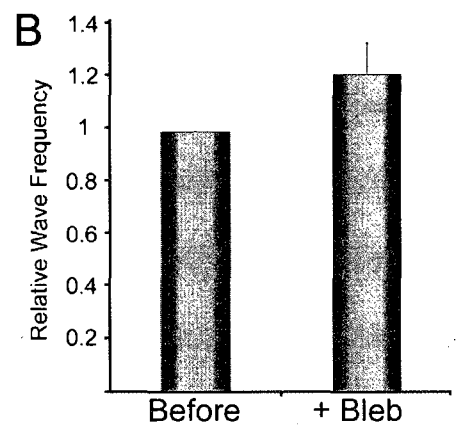
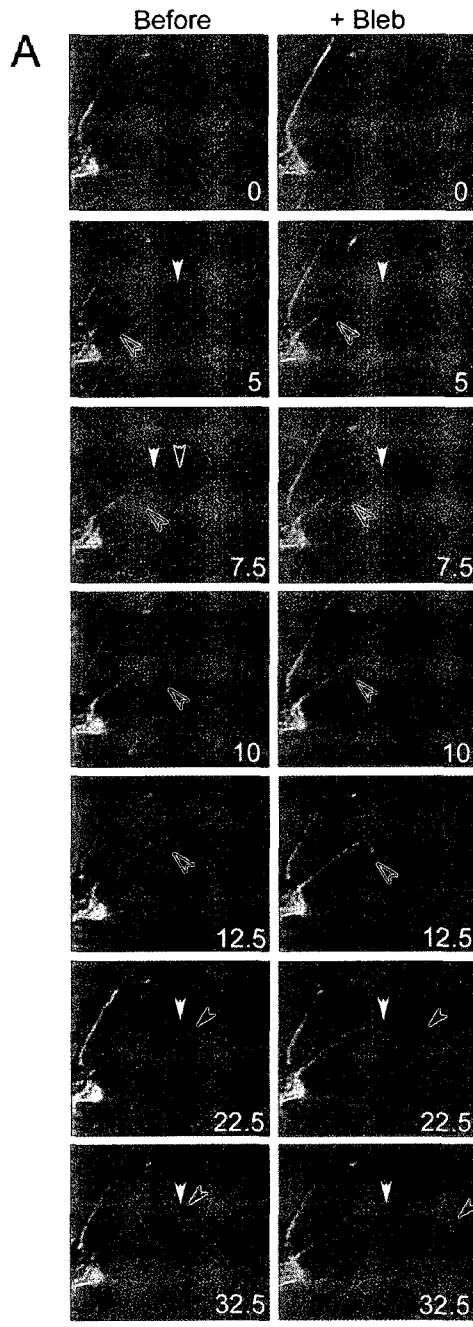


Figure 3.6. Inhibition of myosin II influences wave dynamics.

(A.) Images of a neuron before and after treatment with blebbistatin. Blebbistatin reduces the retraction of the neurite preceding wave arrival. Before blebbistatin addition, as waves (black hollow arrowhead) approach the neurite tip (white arrowhead) there is a retraction of the neurite, followed by a small outburst of growth. After blebbistatin addition, a wave propagating down the same neurite does not cause retraction preceding outgrowth and the subsequent burst in neurite outgrowth (solid black arrowhead) is greater and longer lasting. (B.) Myosin inhibition increases wave frequency $22.2 \pm 0.1\%$ ($n=27$ neurons, error bars= SEM). (C.) Myosin II inhibition decreases the average retraction distance induced by waves. Before wave arrival, control neurites retract $5.6 \pm 0.7 \mu\text{m}$ and blebbistatin-treated neurites retract $2.3 \pm 0.5 \mu\text{m}$ (** $p < 0.01$) (error bars = SEM). (D.) Myosin II inhibition increases wave impact on neurite growth. Upon wave arrival, control neurites extend an average of $9.9 \pm 0.2 \mu\text{m}$, whereas blebbistatin-treated neurites extend an average of $15.9 \pm 1.6 \mu\text{m}$ (** $p < 0.01$) ($n=13$ neurons, error bars = SEM).



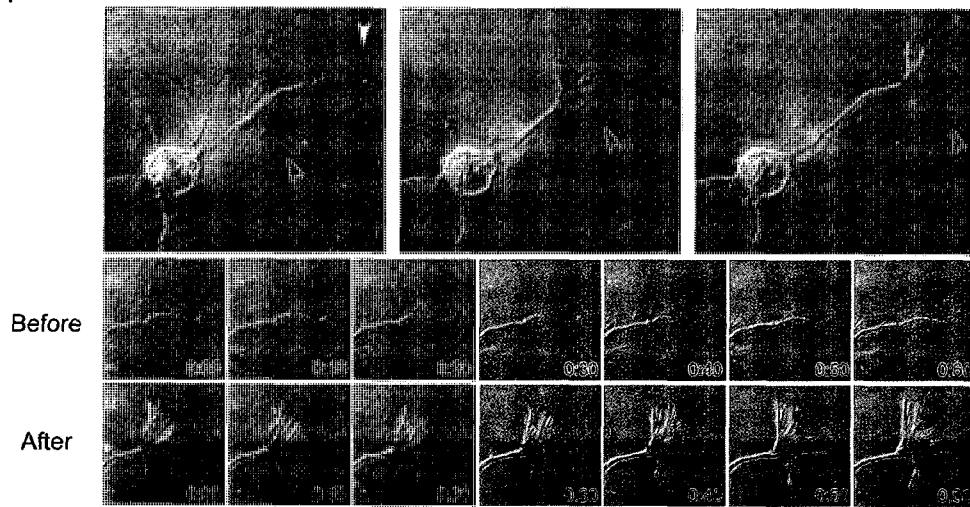
Preceding wave arrival at the growth cone, the neurite retracts several microns (Figure 3.6A, C). Treatment with blebbistatin reduces by over 2-fold the distance of retraction compared to untreated controls. The average magnitude of outgrowth following blebbistatin treatment also increased 1.5 fold relative to control neurons (Figure 3.6D). In the presence of blebbistatin, waves have increased filopodial dynamics and induce axonal branches more frequently than in control neurons.

Laminin increases axon growth in hippocampal neurons (Esch *et al.*, 1999) and can rescue neurite growth of cortical neurons lacking Ena/Vasp proteins (Dent *et al.*, 2007). Hippocampal neurons cultured on laminin display a significant increase in the percent of neurons extending one or more axons and have increased neurite branch density and more waves. Several instances of waves inducing axonal branches in neurons growing on laminin were observed. Taken together these data suggest that myosin II inhibition or growth on laminin enhances axon growth and branching, at least in part via increased wave activity.

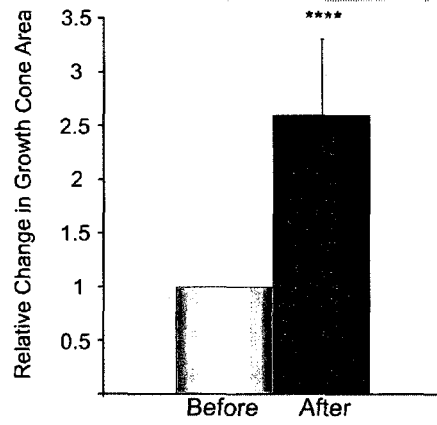
Waves increase growth cone size and dynamics. Preceding the rapid growth of the axon, the size and dynamics of the presumptive axon growth cone increases (Bradke and Dotti, 1997; Bradke and Dotti, 1999; Kunda *et al.*, 2001). Therefore, we sought to determine if wave arrival at the distal neurite increased growth cone size and dynamics. Short interval DIC time-lapse imaging revealed that wave arrival at the neurite tip (Figure 3.7A) increased growth cone size by 2.6 fold and growth cone dynamics by 2 fold (Figure 3.7B, C). Furthermore, we often observed collapsed, non-dynamic growth cones transform into large and extremely dynamic growth cones upon wave arrival (Figure

Figure 3.7. Waves increase growth cone size and dynamics. (A.) DIC images of a neuron with propagating wave (top row, arrowhead). Magnified view of time-lapse images of the same growth cone for 1 min before (top row) and 1 min after (bottom row) wave arrival. Time shown is in seconds. The growth cone enlarges and becomes more dynamic following wave arrival. (B.) Relative growth cone size increases 2.6 ± 0.7 fold after wave arrival ($n=18$, error bars=sd; **** $p<0.001$). (C.) Growth cone activity (relative change in area every ten seconds ($\Delta A/10s$) increases from $16.1 \pm 6.6\%$ $\Delta A/10s$ to $22.5 \pm 6.2\%$ $\Delta A/10s$ after wave arrival ($n = 15$, error bars=sd; **** $p<0.001$).

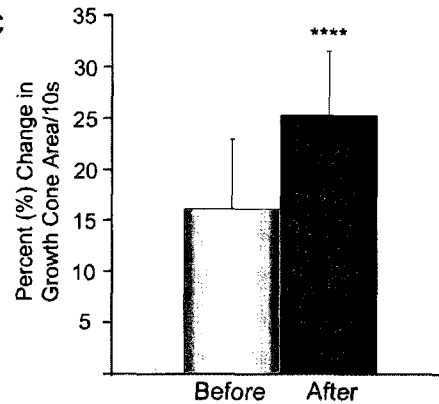
A



B



C

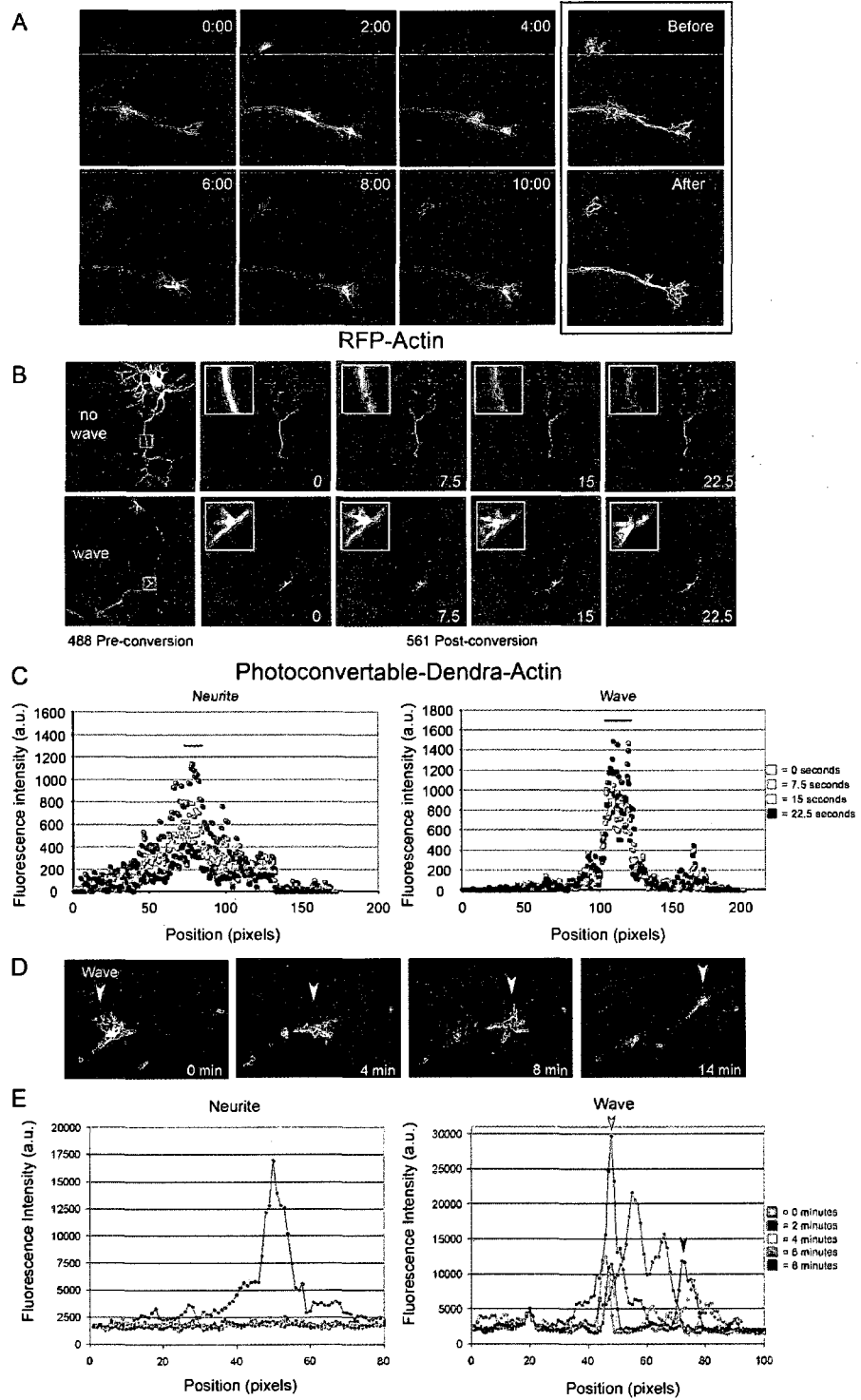


3.7A). Growth cones that were dynamic prior to wave arrival also underwent a moderate, albeit significant increase in dynamics. These data suggest that waves increase growth cone size and dynamics, two features correlated with axon specification.

Waves transport actin. To visualize actin in live-cell experiments, we utilized monomeric Red Fluorescent Protein (Campbell *et al.*, 2002) fused to actin (mRFP-actin). When expressed in hippocampal neurons mRFP-actin incorporates into the highly dynamic actin structures of growth cone filopodia and lamellipodia. In waves, mRFP-actin was dynamic and upon arrival at the growth cone it incorporated into actin structures within growth cones resulting in a net increase in their fluorescence intensity (Figure 3.8A). Because waves induce a rearrangement of cortical actin in the neurite, it is possible that actin in waves does not translocate along with the wave. To address this possibility, we utilized a photo-activatable GFP and a Green-to-Red photo-convertible Dendra (Gurskaya *et al.*, 2006) fused to β -actin (hereafter referred to as paGFP-actin and pcDendra-actin). For paGFP-actin, wave structures were identified by DIC imaging before photo-activating the GFP-actin in the wave and following it by time-lapse fluorescence imaging. At least a portion (about 50%) of the activated paGFP-actin traveled in a wave to the neurite tip over a distance of 25 μm . However, some fluorescent actin remains in the neurite and some diffuses into other regions of the cell. Interestingly, we observed in hippocampal neurons with short processes that some actin diffused rapidly, at rates resembling diffusion of dextrans of similar size to actin monomers measured in *Xenopus* neurites (Popov and Poo, 1992).

Figure 3.8. Waves transport actin.

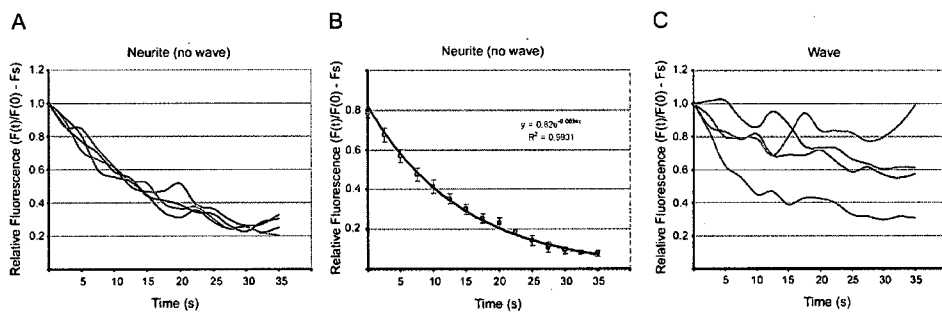
(A.) Fluorescence time-lapse images of a hippocampal neuron expressing RFP-actin. Time shown in min:s. The net fluorescence of RFP-actin in the growth cone increases following wave arrival as shown in pseudocolor images (hot scale) in right panels. (B.) Time-lapse images of hippocampal neurons expressing pcDendra-actin with no wave structures (top row) and within a wave (bottom row). The region photo-converted is within the highlighted box. Following photo-conversion, images were acquired at 561 nm excitation every 7.5 s. The fluorescence dissipates rapidly in a non-wave region but remains associated with the wave when photo-converted within a wave (insets). (C.) Line-scans of peak fluorescence intensity of pcDendra-actin following photo-conversion of a neurite with no wave (left) and of a wave (right). Photoconverted pcDendra-actin decays to <30% of the original peak intensity-value within 15 s in the non-wave region but remains high in the region of a wave (>90% of original peak intensity-value at 22.5 s). (D.) Fluorescence images (561 nm excitation) showing movement of pcDendra-actin in a wave as the wave moves down the neurite. (E.) Linescans of pcDendra-actin over longer periods than in *panel C*. Photo-converted Dendra-actin dissipates almost completely within 2 min (green symbols) in non-wave region of a neurite but >30% of the total original wave fluorescence (red) remains after 8 min (dark blue) by which time the wave has traveled ~15 μm . The fluorescence distribution changes over time due to the changes in wave shape.



To determine whether actin in waves behaved fundamentally differently from actin within non-wave regions, we utilized pcDendra-actin. It requires less energy for photoconversion to a usable signal than paGFP-actin, the red Dendra is quite stable for imaging, and neurons expressing Dendra-actin can be identified by their green fluorescence prior to photoconversion. By photo-converting a limited amount of pcDendra-actin within specific regions of the neurite, we showed that actin within non-wave regions diffuse rapidly and bi-directionally away from the original region of photoconversion, whereas, actin within waves remained associated with the wave over a longer period of time even while it migrates (non-diffusive) (Figure 3.8B, C). Diffusion of actin within non-wave regions is supported both by analysis of fluorescence decay, which demonstrates that the peak of photoconverted-actin decays exponentially (as expected of one-dimensional diffusion-based processes, $\tau = 0.06 \text{ s}^{-1}$) (Figure 3.9), and line-scan analysis, which demonstrates a Gaussian distribution of actin centered at the region-of-photoconversion (Figure 3.8C). It is of interest to note that within non-wave regions, the distribution of actin quickly broadens beyond the original width of the photoconversion region, which is noticeable even at the first frame of 561 nm imaging (Figure 3.8C). In addition, nearly 20% of the pc-actin does not diffuse away during the first 30 s, suggesting that a minor but more-stable pool of actin is also present (Figure 3.8D, E). Indeed, a mixed-model of two Gaussian distributions can be used to fit the actin-distribution (data not shown). In contrast, actin within waves is transported by a non-diffusive process. This is supported by the non-exponential decay-of-peak-fluorescence of actin within waves (Figure 3.9), and by line-scan analysis, which shows that peak-fluorescence is maintained over a longer time-period and that the distribution of

Figure 3.9. Fluorescence loss from photo-converted Dendra-Actin suggests that actin diffuses rapidly in non-wave regions of the neurite shaft but remains associated with waves for longer times.

Fluorescence loss of photo-converted Dendra-actin follows an exponential decay in non-wave regions of neurite as measured by line-scan analysis of each individual curve (A.) (n=4), and when combined and analyzed by best-fit to an exponential curve (B). The line represents the displayed equation (error bars = SEM). (C.) Fluorescence loss plotted against time in waves from four different neurons as measured by line-scan analysis. In three of the examples shown, the fluorescence is more stable over time and in the one example in which the fluorescence loss appears exponential (purple line), the wave collapsed and dissipated.



actin does not broaden beyond the original width of the photoconverted-region when the wave remains relatively stationary (Figure 3.8E).

We also sought to determine if actin remains cohesive within the wave as it travels over longer distances and over longer time frames. A portion of photo-converted actin remained within waves over several minutes (Figure 3.8D, E). However, the majority of the pc-actin fluorescence is lost and diffuses away from the wave as it travels over long distances. This indicates that the actin in waves is dynamic and interchanges with the freely diffusing actin subunits and cortical actin in neurite. In support of this, pc-actin from nearby regions in the neuron amalgamated into a nearby wave. In addition to delivering actin to the terminal tip of the neurite, we also observed waves delivering actin to shaft filopodia, which supported the rapid growth of the protrusion into a potential branch-point (data not shown).

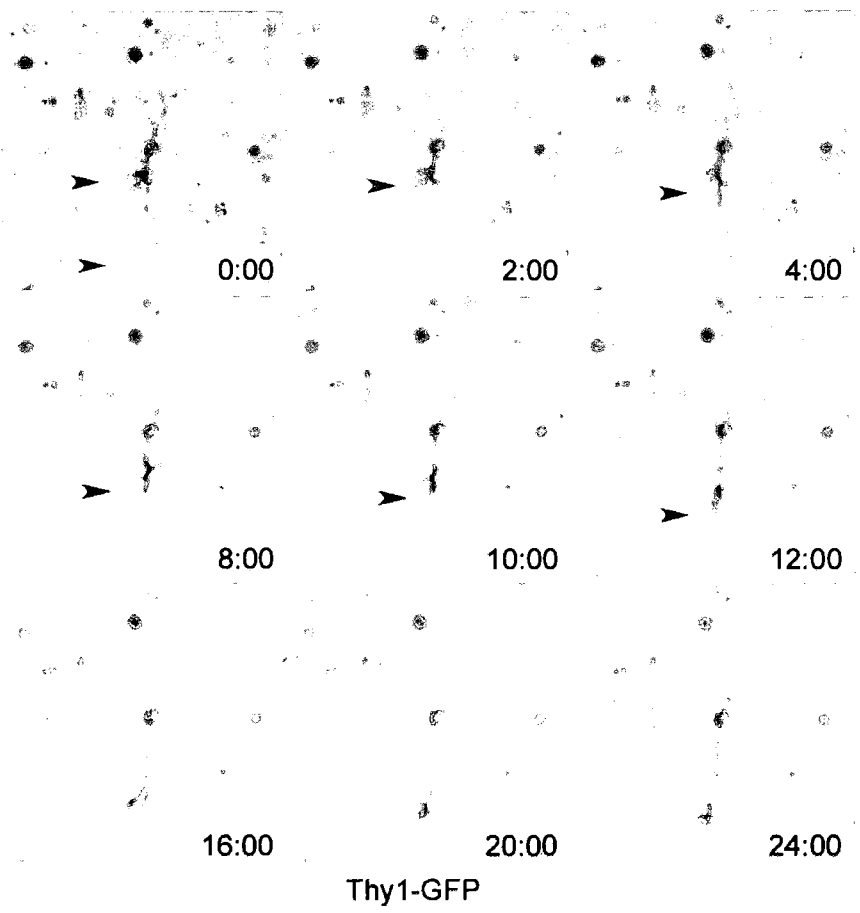
Other proteins found in waves are involved in axon growth (and neurite growth in general) and are likely also transported in waves. For example, as previously mentioned, ADF/cofilin proteins are known to influence neurite growth, growth cone dynamics, pathfinding and axon formation (Meberg and Bamberg, 2000; Kuhn *et al.*, 2000; Aizawa *et al.*, 2001; Endo *et al.*, 2003; Wen *et al.*, 2007; Garvalov *et al.*, 2007). Fluorescently labeled cofilin behaved similarly to mRFP-actin and was transported to growth cones in waves in cultured neurons (data not shown). In other cases, we observed a gradual increase in cofilin-GFP in growth cones (data not shown).

Waves occur in neurons within hippocampal slices. Although waves are prevalent in cultured neurons (Ruthel and Banker, 1998, 1999; Heidemann *et al.*, 2003; Rosso *et*

al., 2004; Toriyama *et al.*, 2006; Tursun *et al.*, 2005), it is possible they are an artifact of culturing neurons on a two-dimensional substrate. To determine if waves are physiologically relevant, we examined fixed and live hippocampal slices in which neurons were fluorescently labeled either with the lipophilic dye, DiI, or via the expression of Thy1-YFP (Feng *et al.*, 2000). Although we focused these studies on neurons in the dentate gyrus and the mossy fiber tract because previous work showed neurogenesis, neurite formation and outgrowth occur robustly in these regions early in postnatal development (Dailey *et al.*, 1994; Knoll *et al.*, 2006), other regions of the hippocampus including CA3 and CA1 as well as entorhinal cortex and cerebral cortex were also observed. Wave-like structures were seen in neurons from all of these regions, but waves were especially robust in the dentate gyrus from the Thy1-YFP transgenic mice as observed *in vivo* in fixed sections.

To confirm that these structures were waves, we performed 3-dimensional time-lapse confocal microscopy of individual neurons in organotypic hippocampal slices. We observed growth cone advance of DiI and Thy1-YFP labeled mossy fiber axons occurs at rates between $0.9\mu\text{m}/\text{min}$ and $2.5\mu\text{m}/\text{min}$ calculated from 2D projected image stacks. In these slice preparations we also observed waves in neurons in the dentate gyrus and CA3 regions of the hippocampus. In DiI labeled neurons, we observed waves traveling in 3-dimensions in the dentate gyrus. We also observed waves in Thy1-YFP neurons in CA regions of the hippocampus (Figure 3.10). In brain slices we also observed that wave arrival at the distal neurite increased growth cone size and advance (Figure 3.10), similar to observations in culture. Wave velocity in slices is similar to that measured in dissociated neuronal culture, ranging between $0.8\mu\text{m}$ and $5.6\mu\text{m}/\text{min}$ with an average of

Figure 3.10. Waves occur in Thy1-YFP labeled neurons in hippocampal slices. Inverted fluorescence time-lapse images of a YFP-expressing neuron near the CA3 region of a P1 hippocampal slice from the Thy1-YFP transgenic mouse line H (Feng *et al.*, 2000). Time shown is in min:s. Black arrowhead follows an anterograde wave which moves $\sim 30 \mu\text{m}$ at an average speed of $1.5 \mu\text{m}/\text{min}$ toward the tip (gray arrowhead in first panel). The images are maximum projections of 6, $1 \mu\text{m}$ steps of a Z series. The soma of this neuron is not within the field of view. This wave travels $\sim 30 \mu\text{m}$ in 20 min (average speed of $1.5 \mu\text{m}/\text{min}$). Upon reaching the distal neurite, the growth cone enlarges and the neurite extends (bottom row). Bar = $30 \mu\text{m}$



2.3 $\mu\text{m}/\text{min}$. This velocity is similar to that of rapid growth cone advance and within the range of slow axonal transport. In addition, neurons in slices expressing GFP-actin contained dynamic actin in waves that appeared similar to growth cones. In hippocampal slices, waves also induced neurite branching via the engorgement and extension of shaft filopodia.

Significantly, we rarely observed waves in long axons of the mossy fiber tract, demonstrating that waves occur preferentially early in neuronal development. This finding agrees with observations of Ruthel and Banker (1999) and our observations in dissociated neuronal culture where wave frequency was high in the first few days (0.25-3 div) as neurites rapidly extend, but decreased later in culture (4-5 days), when neurite growth has declined (data not shown).

Discussion

In the decade that has passed since they were first described (Ruthel and Banker, 1998, 1999), waves have received surprisingly little attention from the research community. Our work has expanded on the understanding of growth cone-like waves in axonogenesis, neurite branching and actin transport as well as confirming previous observations made on growth cone-like waves (Ruthel and Banker, 1998, 1999; Heidemann *et al.*, 2003; Rosso *et al.*, 2004; Toriyama *et al.*, 2006; Tursun *et al.*, 2005). Importantly, we also provide the first evidence that waves occur in *ex vivo* brain slices, suggesting a role during *in vivo* neuronal development.

What are waves? Previous studies showed that actively propagating waves behave similarly to growth cones in their rate of advance (1-6 $\mu\text{m}/\text{min}$) and in undergoing

arrest and collapse in the presence of cytochalasin and nocodazole, but not in the presence of Brefeldin A, suggesting both microtubules and actin, but not Golgi-derived vesicles, are necessary for their propagation (Ruthel and Banker, 1998; Bradke and Dotti, 2000; Ruthel and Hollenbeck, 2000). We identified in waves additional regulators of growth cone motility and actin dynamics, including cofilin, Lim kinase, Slingshot, Arp3, Rap1, Rac1 and cdc42 and showed that waves contain newly assembled microtubule ends containing tyrosine-tubulin but no acetylated tubulin. All of these components suggest that waves are truly growth-cone structures that migrate along the neurite shaft where acetylated (stable) microtubules predominate.

The formation of wave-like structures is not restricted to neurons and insight into their formation has come from studies with the slime mold *Dictyostelium* (Bretschneider *et al.*, 2009). *Dictyostelium* forms wave structures on the substrate attached membrane of the cell that propagate along the membrane using an actin treadmilling mechanism that contributes to membrane protrusion when the waves reach the cell perimeter, much like the burst in neurite extension we see when waves reach the growth cone. Actin waves in *Dictyostelium* are induced during recovery after washout of the actin sequestering compound, Latrunculin A, suggesting that they form spontaneously from the self-organization of the actin cytoskeleton. *Dictyostelium* waves are devoid of myosin II but contain a single headed myosin (MyoIB) at the wave front, Arp2/3 complex in a three dimensional network linked to MyoIB via the adapter protein CARMIL, and coronin at the rear of the wave in close apposition to the substratum (Bretschneider *et al.*, 2009). Occasionally these waves collapse or reverse direction, similar to what we observe for growth-cone like waves. A disruption in the localization or inactivation of some key self-

organizing component presumably underlies decreases in wave motility; in neurons this eventually leads to wave collapse into the neurite shaft, which we observed in some instances. This may be similar to growth cone collapse, which can be induced by changes in actin regulating proteins (Gallo and Letourneau, 2004).

Since Dictyostelium waves can be induced during recovery from actin disassembly by Latrunculin A, it is likely that localized disruption in actin organization at the neurite soma junction could be involved in wave formation in neurons. Because cofilin is a major component of growth cone-like waves, its activity at the neurite soma junction might be the wave initiator. Furthermore, during neuronal development much of the cofilin is transported from the soma to distal regions of the neurites and a decline in its concentration or activity in the soma could lead to the observed decrease in wave frequency as neurites elongate. Studies to examine these questions are in progress.

Waves influence axon development. Although waves occur indiscriminately in all of the minor processes of a stage 2 neuron, there is a >2 fold increase in wave frequency and a greater impact of waves on outgrowth in the presumptive axon during the stage 2-3 transition. This suggests that individual waves may have fundamental differences (all waves are not equal) or that the growth cones of different neurites have pre-existing differences producing varied responses upon wave arrival (all growth cones are not equal). Although we observed that waves are diverse in their size and advance rates, our results cannot rule out that inherent diversity of growth cones biases differential responses to wave arrival, especially considering that wave-induced changes in growth cone dynamics depended on the preexisting dynamic state of the growth cone. We also observed that abrupt, short-term increases in wave frequency provided greater impetus

for neurite extension than waves arriving in isolation. In one case we observed the arrival of 5 waves in rapid succession immediately preceding a burst of growth and the subsequent development of the axon.

The observation that waves occur more frequently and have greater impact on growth in the developing axon suggests that waves provide some impetus for axon differentiation. To further study the involvement of waves in axon development we looked at the influence of two factors that influence axonogenesis on wave frequency and impact. The myosin II inhibitor, blebbistatin, greatly enhances axon growth, and even increases the percent of neurons with supernumerary axons. Myosin II inhibition also increased wave frequency and augmented the impact of waves on neurite growth. Likewise, the extracellular matrix protein, laminin, a signal that promotes axon growth in hippocampal neurons, also enhanced wave frequency, supporting our hypothesis that waves enhance axon specification.

Waves and branching. Branched neurite networks are another important aspect of brain development *in vivo*. In developing cortical neurons, axonal branching can be inhibited by treatment with drugs that disrupt the dynamics of either microtubule or actin but at concentrations below those that affect axon outgrowth (Dent and Kalil, 2001). Similar treatments also impede wave propagation (Ruthel and Banker, 1999) suggesting a possible link between waves and branching. We have observed both the bifurcation of waves at a branch point supporting outgrowth of both branches and waves choosing one branch over the other enhancing elongation of only one branch. During *in vivo* development, axon outgrowth and branch extension occur independently such that branch

growth occurs while axons are stalled (O'Leary and Terashima, 1988; Luo and O'Leary, 2005).

Collateral branches can form along the axon shaft in response to positive extracellular signals (Tang and Kalil, 2005). We have observed waves inducing collateral branching from the neurite shaft by causing the engorgement of a stable shaft filopodium, resulting in its conversion to a new branch. Thus, waves can generate a new growth cone from the engorged filopodium by delivering actin and other molecules required for growth cone function. Waves may also direct the fusion of TI-VAMP vesicles at branch-points, providing membrane necessary for branch elongation and serve as sites for calcium transients that also are correlated with branch growth (Hutchins and Kalil, 2008). Other indirect evidence suggesting waves contribute to branch formation is the correlation between enhanced branching and wave frequency we observed following treatment of neurons with blebbistatin or laminin. Inhibiting myosin II activity may relax the rigid cortical F-actin allowing increased actin dynamics, filopodia formation, engorgement and branch formation. Laminin may also stabilize shaft filopodia increasing the opportunities for waves to induce a branch.

Waves increase growth cone size and motility. During axon formation, the growth cone of one of the multiple neurites enlarges and displays increased dynamics (Bradke and Dotti, 1997, 1999; Ruthel and Hollenbeck, 2001; Kunda *et al.*, 2001), which is associated with more rapid outgrowth (Gallo and Letourneau, 2004). This neurite undergoes rapid elongation forming the axon. We observed over a 2.5 fold increase in growth cone size and over a 1.6 fold increase in growth cone dynamics following wave arrival at the growth cone. Although wave arrival increased the dynamics of growth

cones that were previously active, waves had a much greater effect on growth cone activity when merging with less active growth cones. Thus, waves influence axon development by increasing growth cone size and dynamics, a prerequisite for axon specification. Theoretically, if size is the only thing that matters, wave arrival can deliver a bolus of material for the extension of about 20 μm of neurite shaft if growth cone area expands from 50 μm^2 to 150 μm^2 . This is based on our measurement where 10 μm of shaft < 50 μm^2 surface area and we commonly observed > 100 μm^2 increase in the size (area) of a growth cone following wave arrival.

Are waves a transport mechanism? Thirty years ago it was observed that neurofilament proteins, tubulin and actin synthesized in the soma traveled in the slow component of axonal transport in mature neurons (Black and Lasek, 1979) yet three decades later, exactly how these proteins are transported remains controversial. Most microtubules are relatively stationary in axons (Ma *et al.*, 2004) but in cultured neurons some short assembled microtubule pieces can move rapidly along the stationary microtubules in both directions. This movement has a bias toward the anterograde direction accounting for “slow” net transport rates (Wang and Brown, 2002), a similar mechanism to what was observed for movement of some neurofilaments in the “stop and go” hypothesis (Wang and Brown, 2001; Brown *et al.*, 2005). With this as a model, it has been suggested that actin is also transported in a filamentous form along microtubules (Baas and Buster, 2004) but direct evidence for this is lacking. Indeed, in chicken sciatic nerve actin is transported with proteins that are associated with unassembled or dynamic actin (Mills *et al.*, 1996). Furthermore, the strong bias for newly assembled tyrosinated microtubule subunits at the distal end of a growing axon supports microtubule assembly

at the distal tip. Taken together these results suggest that multiple mechanisms exist for transporting cytoskeletal proteins down axons.

Here we directly observed the anterograde movement of fluorescently labeled actin in waves. Because we could not rule out the possibility that as waves move forward they cause a reorganization of the cortical actin in the neurite shaft and result in no net translocation of actin, we used photo-activatable (pa)GFP-actin and photo-convertible (pc)Dendra-actin, which were only photo-activated/converted within the wave, to ascertain if actin was traveling with the wave. We observed a portion of this actin reaches the growth cone after traveling down the neurite shaft at a rate consistent with slow transport. However, not all of the actin arrived at the neurite tip. Indeed, we often observed that pcDendra-actin in a wave could incorporate into filopodia along the neurite, while the wave continued, suggesting that some subunits from the dynamic actin in the wave exchange with more stationary actin structures while others are recycled back into actin filaments in the advancing wave. This is reminiscent of the situation within growth cones. When paGFP-actin or pcDendra-actin in growth cones is photo-activated, the actin initially remains associated with dynamic filaments and most subunits released from treadmilling filaments get reincorporated but some subunits are lost by diffusion or exchange into other actin structures that remain behind and the fluorescence eventually declines. The tendency for actin to remain associated with the growth cone is positively correlated to its growth rate, which is related to the continuous reutilization of subunits in treadmilling filaments (Marsh and Letourneau, 1984; Letourneau *et al.*, 1987). If paGFP-actin is activated in growth cones where advance does not occur, fluorescence is found to dissipate rapidly and appear back in the soma within 5-10 min (unpublished

observations). Conversely, waves that contribute to greater neurite outgrowth may also deliver more actin and other important growth promoting factors. Although a portion of the actin remains associated with the wave as it moves, the actin composition in the wave does not need to remain unchanged as a wave travels forward in order for the wave to, in effect, "deliver" actin. In short neurites without waves, freely diffusing actin subunits can reach distal neurites relatively rapidly but it is unlikely to contribute to growth spurts or branch initiation. Conversely, waves can deliver to distal neurites or branch points a large bolus of actin and actin assembly regulatory molecules such as cofilin, previously identified to be transported with actin in slow axonal transport (Mills *et al.*, 1996) and important for neurite outgrowth, axon development, growth cone motility and pathfinding (Meberg and Bamberg, 2000; Abe *et al.*, 2003; Garvalov *et al.*, 2007; Wen *et al.*, 2007). Not only is cofilin transported with waves, but it is the dephosphorylated (active) form that is most prevalent, suggesting its role in wave motility is similar to its role in growth cones. Another axon-promoting molecule, shootin, was also recently shown to be transported in waves (Toriyama *et al.*, 2006). Thus, waves likely represent one mechanism for transporting large amounts of growth promoting molecules to growth cones, thereby stimulating axonogenesis.

Although an attractive hypothesis for mediating outgrowth spurts, waves are certainly not the only means for transport of these molecules. We have observed a number of neurons (~20%) that do not exhibit waves over a time-course of hours in culture, yet still have active neurite outgrowth and periodic fluctuations in growth cone size and motility. In addition, we have observed gradual accumulations of actin and cofilin in growth cones without any obvious wave transport. Thus actin transport, of

which waves are but one component, appears to occur through multiple redundant mechanisms. Waves are unique in that they can supply large amounts of materials directed to particular locations such as growth cones and branch points and can be employed during early neuronal development when rapid phases of neurite outgrowth and axonogenesis occur.

Waves occur in brain slices. Because previous studies have identified waves only in dissociated cultured neurons, their relevance to neuronal development *in vivo* is rightfully questioned. Thus we sought to determine if waves occur on neurons developing within *ex vivo* organotypic hippocampal slices, a more *in vivo*-like setting. Three different labeling methods were used to visualize waves in neurons within slices, membrane labeling with DiI or Thy1-YFP and adenoviral-mediated cytoplasmic expression of fluorescent proteins. We observed waves in developing neurons with each of these methods. We also observed wave-induced growth cone enlargement, neurite growth enhancement and the induction of new branch-points in slices, all similar to what we observed in dissociated neuronal cultures. Interestingly, we never observed long axons with active growth cones that also exhibited waves. This may suggest that waves are important only during the initial, rapid phase of neurite growth and axonogenesis; however it might also reflect the limited number of long axons we examined. In summary, waves appear to have important functions in neuronal development. Future work will further elucidate the molecular underpinnings of wave initiation and their role in other processes such as axon guidance and regeneration.

Chapter 4

Glutamate-induced cofilin-actin rod formation requires AMPARs and is associated with a disruption of trafficking of APP-YFP-containing vesicles

Preface and Acknowledgements

Work presented in this chapter will be prepared for publication. The order and list of authors, as it stands right now, will include: Chi W. Pak (CWP), Alisa E. Shaw (AES), Laurie S. Minamide (LSM), Richard C. Davis (RCD), and James R. Bamberg (JRB). Virtually all of the results presented in this chapter were completed by CWP, except for Figure 4.5, which was done entirely by AES. AES also first performed the mutagenesis screen to identify the R21Q cofilin mutant, although CWP conceived of its use it for live-cell imaging. LSM helped with neuronal dissections and RCD contributed conceptually to the work. The text and figures were prepared by CWP and edited by JRB.

This work was supported by the National Institute of Health (JRB). We would also like to acknowledge Bechara Kachar, Kathy Partin, Barbara Bernstein, Ian Marsden, O'Neil Wiggan, and Ineka Whiteman for their helpful discussions. The following viruses were cloned and amplified by the following people: (WT or R21Q cofilin mutant, AES), (EB1-GFP, AES or Lubna Tahtamouni), (APP-YFP, Mike Maloney). We also acknowledge their contributions to this work.

Abstract

AD pathology is characterized by disruptions to both the actin and microtubule cytoskeletons. Using glutamate excitotoxicity as model system for cofilin pathology in

AD, we have determined signaling mechanisms for glutamate-induced cofilin-actin rod formation in young hippocampal neurons. Our results demonstrate that glutamate-mediated rod formation depends on AMPA receptors but not on Ca^{2+} or the Ca^{2+} -dependent proteins, calcineurin and calpain. In addition, we have determined effects, which are associated with rod formation, on the co-localization of high molecular weight (HMW) isoforms of MAP2 with rods, microtubule dynamics, and trafficking of APP-YFP-containing vesicles. The presence of cofilin-rods is often though not always associated with increased HMW MAP2 staining in neurites. In some instances, HMW MAP2s also appear to co-localize with cofilin-rods. The presence of cofilin-rods is also associated with a general loss of trafficking of APP-YFP-containing vesicles. Our results suggest that the induction of cofilin-actin rods by glutamate excitotoxicity may contribute to AD pathology through a general disruption of MAP proteins and normal vesicle trafficking.

Introduction

Alzheimer disease (AD) is the leading cause of dementia, which generally manifests later in life and progresses interminably (Monien *et al.*, 2006). Dementia describes a general condition associated with a decline in cognitive abilities, including the loss of short- and long-term memory. Because other neurological diseases, such as frontotemporal dementia (FTD), may manifest with similar symptoms, a positive diagnosis of AD can only be made post-mortem (Monien *et al.*, 2000). Pathologically, AD is distinguished by the combined presence of extracellular amyloid plaques and intracellular neurofibrillary tangles (NFTs) (Hyman and Tanzi, 1992). Other neurological

diseases, such as FTD, may be characterized by the presence of either aggregation but not both (Kertesz, 2009). The only treatment available to AD patients is palliative and transient; the progression of dementia may be delayed but not prevented by treatment with cholinesterase inhibitors (Pepeu and Giovannini, 2009). Curative or preventative treatments of AD are still sought after despite considerable research in the field.

The constituent proteins of amyloid plaques and NFTs are amyloid beta₁₋₄₂ (Aβ₁₋₄₂) and the microtubule-associated protein (MAP) tau, respectively (Peskind, 1996). Aβ₁₋₄₂ is a 42 amino acid peptide generated by the sequential cleavage of its parent protein, amyloid precursor protein (APP), by the two protease complexes, β- and γ-secretase (Thinakaran and Koo, 2008). APP may also be processed through a non-amyloidogenic pathway by sequential α- and γ-secretase cleavage to produce the related but non-pathogenic, Aβ₁₋₄₀ (Thinakaran and Koo, 2008). Multiple lines of evidence incriminate Aβ₁₋₄₂ as the pathogenic molecule in AD. Perhaps most damning are naturally-occurring mutations in APP, APP-processing enzymes, or APP-clearance enzymes, which cause heritable early-onset manifestations of AD (Williamson *et al.*, 2009). These include at least 25 distinct mutations in APP, which affect its proteolytic cleavage, resulting in the increased production of Aβ₁₋₄₂ (Thinakaran and Koo, 2008). Mutations in presenilins, the catalytic subunit of the γ-secretase complex, and in apolipoprotein-E (Apo-E), which regulates Aβ₁₋₄₂ levels in the brain, result in increased Aβ₁₋₄₂ load and familial AD (Williamson *et al.*, 2009). Similarly, overexpression of APP also increases AD risk, which explains the co-incidence of AD in Down syndrome (DS) patients (Neve *et al.*, 2000). The APP allele is located on chromosome 21; thus DS patients carry three copies of the APP allele. Results from dissociated neurons and animal studies also demonstrate

that purified A β ₁₋₄₂ can disrupt synaptic plasticity and learning. A β ₁₋₄₂ enhances long-term depression (LTD) and precludes long-term potentiation (LTP) in rodent organotypic slices (Shankar *et al.*, 2008; Li *et al.*, 2009). Also, dimeric species of A β ₁₋₄₂, which were purified from the brains of AD patients post-mortem, could prevent learning in a passive avoidance task when injected into the rat hippocampus (Shankar *et al.*, 2008). However, it should be noted that A β ₁₋₄₂ load is not always correlated with cognitive deficiencies. Transgenic mice carrying an APP mutant that prevents its cleavage by caspases do not exhibit learning and memory deficits despite high A β ₁₋₄₂ production (Galvan *et al.*, 2006). Thus, intermediary proteins and processes are required to mediate A β ₁₋₄₂-toxicity. For instance, expression of the cellular prion protein, PrP(c), is required for A β ₁₋₄₂-dependent effects on LTP (Laurén *et al.*, 2009).

A β ₁₋₄₂-toxicity also depends on the expression of the microtubule-associated protein (MAP), tau (Rapoport *et al.*, 2002). Tau stabilizes microtubules and in mature neurons is axonally-restricted (Dehmelt and Halpain, 2005). Its aggregation into NFTs is initiated by its hyperphosphorylation, which reduces its ability to bind to microtubules (Johnson and Stoothoff, 2004). Multiple phosphorylation sites on tau have been identified, which are substrates for several kinases *in vitro* and *in vivo*, including JNK, CAMKII, cdk5 and GSK-3 β , among others (Churcher, 2006). Whereas tau-hyperphosphorylation is generally regarded as being deleterious, whether tau-aggregation is ultimately neuroprotective or neurodegenerative remains controversial (Bretteville and Planel, 2008). Nevertheless, the presence of NFTs is well-correlated with the severity of dementia (Giannakopoulos *et al.*, 1997; Braak and Braak, 1995), and several phospho-tau mutants, which were identified in FTD, are neurotoxic (Fulga *et al.*, 2007). Though how

exactly hyperphosphorylated tau contributes to the pathology of AD remains unclear, a surprising connection to actin was recently demonstrated (Fulga *et al.*, 2007).

The overexpression of phospho-tau mutants associated with FTD induces cofilin-actin rods (or rods) (Fulga *et al.*, 2007). Conversely, rods appear to be important for the aggregation of hyperphosphorylated tau, since 12E8-positive tau aggregates can be blocked by down-regulating cofilin (Whiteman *et al.*, 2009); 12E8 is a monoclonal antibody that recognizes two specific phospho-epitopes of tau (Litersky *et al.*, 1996). 12E8-positive tau aggregates also co-localize with cofilin-actin rods (Whiteman *et al.*, 2009).

The ADF/cofilin proteins are a conserved family of actin binding proteins expressed in all eukaryotes, from yeast to mammals (Bamburg *et al.*, 2009). In mammals, three isoforms of the ADF/cofilin proteins are present: ADF, cofilin-1, and cofilin-2. Both ADF and cofilin-1 are ubiquitously expressed; in neurons, cofilin-1 is expressed approximately 5-fold more than ADF. Cofilin-2 is alternatively spliced to give two variants, 2a and 2b. Cofilin-2b is the major variant of mRNA expressed and is found exclusively in muscle cells. Though cofilin-2a is expressed in some non-neuronal cells, it constitutes only a minor variant of the total cofilin-2 mRNA.

All of the ADF/cofilin proteins are regulated by various means, including phosphorylation, phospholipid-binding, nuclear shuttling, 14-3-3 binding, and pH. Many of these regulatory mechanisms may operate cooperatively; for example, the conserved phospho-residue (serine-3) is accessible even when PIP₂-bound (Gorbatyuk *et al.*, 2006). Therefore, multiple and possibly parallel mechanisms may be required to fully activate the ADF/cofilin proteins. ADF and cofilin share a common structural-fold (Federov *et*

et al., 1997), which allows them to bind to actin monomers and filaments; however, there are important physiological differences between them. Knockout of cofilin is embryonic-lethal (Gurniak *et al.*, 2005), whereas ADF-null (*corn-1*) mice survive to adulthood and are characterized mainly by blindness due to uncontrolled thickening of the cornea (Ikeda *et al.*, 2003).

Cofilin-actin rods are likely to play a principle role in the onset and progression of AD. This is supported not only by the identification of rods in human AD brain (Minamide *et al.*, 2000; Bamberg and Bloom, 2009), but oligomeric species of A β ₁₋₄₂ can induce rods in both dissociated neurons and in rodent hippocampal slices (Maloney *et al.*, 2005; Davis *et al.*, 2009). In hippocampal slices, A β ₁₋₄₂-induced rods are formed primarily in the dentate gyrus and hilus (mossy fibers) (Davis *et al.*, 2009). Cofilin-actin rods have also been hypothesized to locally disrupt the trafficking of APP-YFP-containing vesicles, which was suggested by the accumulation of APP and its cleavage products at the distal ends of rods (Maloney *et al.*, 2005). Even before amyloid plaques and NFTs are observed, vesicle trafficking defects have been documented (Terwel *et al.*, 2002; Stokin *et al.*, 2005), although underlying mechanisms have not been extensively investigated. In addition to tau, other microtubule associated proteins (MAPs) may also be disrupted and co-localize with rods, especially other MAPs that are known to bind to actin. For instance, high molecular-weight (HMW) isoforms of MAP2a and MAP2b, and the short isoform, MAP2c, bind directly to actin *in vitro* and localize to actin-rich regions in cells (Ozer and Halpain, 2000; Dehmelt and Halpain, 2005).

Therefore, it is of great interest to determine not only the signaling mechanisms for cofilin-actin rod formation, but also their relationship to the disruption of

microtubule-based proteins and processes. To investigate these aims, we have chosen to study the glutamate excitotoxicity model, which not only induces cofilin-actin rods rapidly (Minamide *et al.*, 2000), but was recently demonstrated to mediate, at least in part, A β_{1-42} toxicity (Li *et al.*, 2009). Glutamate excitotoxicity can also induce rods in hippocampal slices (Davis *et al.*, 2009), although this effect is likely confounded by homeostatic mechanisms that regulate extracellular glutamate concentration (Herman and Jahr, 2007).

The signaling requirements for cofilin-actin rod formation in neurons due to energy stress (ATP depletion) and in non-neuronal cells due to reactive-oxygen species (peroxide) have already been determined (Huang *et al.*, 2008; Kim *et al.*, 2009). In these previous studies, energy stress and reactive-oxygen species recruit two different cofilin-specific phosphatases, chronophin and slingshot, respectively, through distinct mechanisms. Dephosphorylation of cofilin at the conserved residue, serine-3, is essential for its binding to actin and required for rod formation (Minamide *et al.*, 2000). ATP depletion induces the release and activation of chronophin from Hsp90; chronophin can then dephosphorylate cofilin (Huang *et al.*, 2008). In response to peroxide-treatment, slingshot-1L is recruited instead (Kim *et al.*, 2009). The oxidation of 14-3-3 ζ by reactive oxygen produce by NADPH oxidase releases and activates slingshot-1L (Kim *et al.*, 2009). Thus, it is possible that glutamate excitotoxicity may recruit distinct and parallel signaling pathways.

Here we report the signaling requirements for glutamate-induced rod formation. Glutamate-induced rod formation in 6-7 div rat hippocampal neurons is AMPAR-dependent. (S)-AMPA treatment alone is sufficient to induce cofilin-rods, which can be

blocked by the AMPAR-antagonist, DNQX, but not by NMDA or metabotropic glutamate receptor antagonists. AMPA-induced cofilin-rod formation also does not require Ca^{2+} influx from extracellular sources and occurs in the presence of inhibitors of the proteins, calcineurin and calpain, which have been implicated in glutamate excitotoxicity and AD. In addition, we have determined the effect of AMPA-induced cofilin-rod formation on the distribution of the high molecular-weight (HMW) isoforms of MAP2a and MAP2b, microtubule dynamics, and APP-YFP-vesicle trafficking. HMW MAP2 isoforms are also disrupted by AMPA treatment, and in some cases, HMW MAP2-containing aggregates co-localized with cofilin-rods. The presence of rods is also correlated with a loss of trafficking of APP-YFP-containing vesicles; whereas, in neurons from the same AMPA-treated culture that did not form cofilin-rods, APP-YFP-containing vesicles remained dynamic. Altogether, our results support a general model whereby inter-dependent disruptions to actin- and microtubule-based systems mediate several pathologies observed in AD.

Materials and Methods

Cell Culture: Dissociated rat hippocampal neurons were dissected, frozen, and cultured as previously described (Minamide *et al.*, 2000). Briefly, hippocampi were dissected from embryonic day 18 (E18) rat embryos, dissociated using trypsin (Sigma, T4549) and trituration, and frozen at -80°C in 10% DMSO at a density of 1×10^6 cells/ml. For culturing, neurons were thawed and plated on to poly-D-lysine-coated drilled-out glass-bottom dishes at a plating density of 4.5×10^4 - 6.0×10^4 neurons per dish. Dishes were coated for 16-20 h at 4°C using 0.1% poly-D-lysine (Sigma, P0899) diluted in

borate buffer (50 mM H₃BO₃, 12.5 mM Na₂B₄O₇). Culturing medium for neurons consists of Neurobasal (GIBCO), B27 (Invitrogen, San Diego, CA), GlutaMAX (GIBCO), and 1% penicillin/streptomycin (pen/strep, HyClone). Unless otherwise stated, neuronal cultures were maintained in Neurobasal-based medium in a 37°C, 5% CO₂ humidified incubator. Half of the neuronal medium was replaced every 3rd day with fresh medium (pre-warmed). For experiments involving Hibernate-A-based medium (BrainBits, Springfield, IL), hippocampal neurons were cultured and maintained in Neurobasal-based medium until the day of treatment. On the day of treatment, neurons were switched to Hibernate-A-based medium and maintained in a 37°C ambient-air incubator. Hibernate-A-based media were prepared in a similar manner to Neurobasal-based medium (supplemented with B27 (Invitrogen), GlutaMAX (GIBCO), and 1% pen/strep (HyClone). A431 or A4.8 cells were maintained using high glucose (HG)-DMEM (GIBCO) supplemented with 10% fetal bovine serum (FBS, Atlas Biologicals) and 1% pen/strep. For imaging, A431 or HeLa cells were plated on to uncoated drilled-out glass-bottom dishes.

Drug Treatments: The following glutamate receptor antagonists were used at the following final (working) concentrations and stock solutions were prepared using the solvent indicated: (DNQX, 50 μM, H₂O, Tocris), (AP5, 100 μM, H₂O, Sigma), ((S)-MCPG, 500 μM, 0.1 M NaOH, Alexis Biochemicals), (IEM-1460, 100 μM, H₂O, Tocris). All GluR antagonists were added to cultures 15 min prior to the addition of L-glutamate (Sigma) or (S)-AMPA. The following GluR agonists were used at the following final concentrations and stock solutions were prepared using the solvent

indicated: ((S)-AMPA, 25 μ M, DMSO, Ascent Scientific), (NMDA, 100 μ M, 0.5 M NaOH, Sigma), ((RS)-DHPG, 100 μ M, 0.5 M NaOH, Tocris). The following drugs were used at the concentrations given and stock solutions were prepared using the solvent indicated: (EGTA, 6 mM, 1 N NaOH, Sigma), (Cyclosporin A, 20 μ M, DMSO, Sigma), (FK-506, 25 μ M, DMSO, LC Laboratories), (ALLN, 50 μ M, DMSO, Sigma), (E-64d, 15 μ M, MeOH:H₂O, kind gift of Dr. Donald Mykles), (Kenpaullone, 25 μ M, DMSO, Calbiochem). Typically, these drugs were added 20-30 min prior to adding (S)-AMPA.

Immunofluorescence: For cofilin-rod staining, neurons were fixed for 45 minutes at room temperature (RT) in 4% paraformaldehyde (J.T. Baker), which was prepared in the following buffer: 138 mM KCl, 10 mM EGTA pH 8.0, 10 mM MES pH 6.1, 3 mM MgCl₂, and 0.33 M sucrose. Although fixation was performed at RT for 45 min, the fixative was warmed to 37°C before use. Following several washes with PBS, neurons were permeabilized with -20°C MeOH for 3.5 min at RT. Following several more washes with PBS, neurons were blocked for 50 minutes at RT using 2% goat serum prepared in 1% bovine serum albumin (BSA, EMD Biosciences) in phosphate buffered saline (PBS: 140 mM NaCl, 8 mM NaH₂PO₄·H₂O, 2.7 mM KCl, pH 7.4). The primary antibody, 1439, which detects both ADF and cofilin, was used at a concentration of 1 ng/ μ L to stain cofilin-actin rods formed from endogenous proteins. All primary antibodies were applied overnight (12-20 h) at 4°C. All secondary antibodies (Invitrogen) were applied for 60 min at RT and were used at a dilution of 5 ng/ μ L (diluted in 1% BSA/PBS). Samples were mounted using Prolong Antifade Gold (Invitrogen). The following primary Abs were used at the concentrations given following the indicated permeabilization-method:

(mAb22: anti-cofilin, methanol, Abe *et al.*, 1989), (4317: anti-phospho-ADF and -cofilin, 0.84 ng/ μ L, methanol, Meberg *et al.*, 1998), (AP-20: anti-HMW MAP2a and MAP2b, 6 ng/ μ L, methanol, Sigma), (12E8: phospho-tau, 75 ng/ μ L, Triton X-100, Elan Pharmaceuticals). All fixed samples were imaged using either a Nikon Diaphot epi-fluorescent microscope or an Olympus IX-81 spinning-disc confocal microscope. With the Nikon, the following objectives were used: 20x air (0.4 NA), 40x air (0.75 NA), 60x oil (1.4 NA). Images were captured using a Coolsnap ES CCD camera (Roper Scientific, Tucson, AZ). With the Olympus, a 60x oil (1.4 NA) objective was used and images were captured using an EM-CCD Cascade IIB (Photometrics).

Quantification of Cofilin-Rod Formation: Because cofilin-actin rods occur idiopathically albeit at a low frequency in untreated cultures, the presence of rods alone could not be used to assess rod induction *per se*. Therefore, two indices of rod induction were quantified in order to assess whether rods formed due to a specific treatment: percent-rod index and number-rod index. Percent-rod index is defined as the percentage of neurons that *appeared* to form at least one cofilin-actin rod. The *actual* percentage of neurons that formed at least one rod could not be determined due to the unavoidable and extensive fasciculation of neurites, which made the unequivocal attribution of a rod to a single neuron impossible. Based on studies in which neurons were singly-labeled, the actual percentage of neurons that formed rods was generally less than suggested by quantifying percent-rod index, which sometimes approached 90%. For each experiment, at least 100 neurons were included in this analysis. Number-rod index is defined as the average number of rods counted in a 124 μ m² region (field) that contained many rods. In

general, only one neuronal soma was present in the field, although exceptions were sometimes made. For each experiment, approximately 10 fields were included in the analysis. Though the actual numbers of rods varied widely from field-to-field within a single experiment, the number-rod index was consistent between experiments.

Transfections: WT MAP2 and its phosphorylation-mutants were transfected into cells using Lipofectamine 2000 and by following recommended protocols. Briefly, 1 μ g of DNA was incubated with 2.5 μ l of Lipofectamine 2000 in 100 μ L of OptiMEM for 20 minutes. The DNA:Lipofectamine mix was added to each of the cultures directly.

Adenoviral Infections: Replication-deficient adenoviruses were generated as previously described (Minamide *et al.*, 2003). Briefly, FP-tagged cDNAs were cloned into pShuttleCMV using standard molecular-cloning techniques. Recombination of the cDNA into the adenoviral genome was accomplished by electroporating into a recombinase-positive BJ5183 strain carrying a modified Ad5 adenoviral genome (AdEasy). AdEasy was modified to render it replication-deficient by deleting key genes essential for replication. To produce functional adenovirus, the AdEasy-cDNA construct was transfected into HEK293 cells, which provide the deleted genes *in trans*. After several amplifications in HEK293 cells, a high titer of adenovirus was harvested by iterative freeze-thawing and aliquots were stored at -80°C until their use. The following adenoviruses were used at multiplicity-of-infections (MOI) that were empirically determined: (R21Q-mRFP (cofilin)), (APP-YFP), and (EB1-GFP).

Ca²⁺ Imaging and Analysis: Rat hippocampal neurons (6 div) were loaded with Fura2-AM (Invitrogen) for 50-60 min in a 37°C, 5% CO₂ humidified incubator. Fura2-AM was washed-out once before placing cultures back into the CO₂ incubator for 30 min to permit de-esterification of Fura2-AM to Fura2. For imaging, neurons were switched to a Hibernate-E-based medium and imaged on a heated (37°C) stage using an Olympus IX-81 equipped with a Xenon lamp, Fura2 filter sets, a 40x UV-compatible oil (1.35 NA) objective and a Coolsnap HQ² CCD camera (Photometrics). For each time-point, two images were captured using either a 340 nm or 380 nm excitation filter (340/380 images) and a 510 nm emission filter, which was used for both excitation-wavelengths. An imaging epoch consisting of 12 (340/380) images taken at 5-sec intervals was captured before treating with 25 μM (S)-AMPA to determine a baseline Fura2 ratio for the cell. Immediately after treating with (S)-AMPA, imaging epochs were captured at variable time-points spanning a total of 45 min. In experiments involving EGTA pre-treatment, imaging epochs were captured before and after adding 6 mM EGTA to determine baseline Fura2 ratios for the cell. After adding 25 μM (S)-AMPA, imaging epochs were captured at variable time-points spanning a total of 45 min. To quantify the Fura2 ratio, images were background-subtracted, a 5x5 pixel region was drawn over the soma of all cells in both the 340 and 380 images, and the average intensities calculated. The average intensity from the 340 image was divided by the average intensity from the 380 image to determine the Fura2 (340/380) ratio. The Fura2 ratio for untreated neurons was normalized to 100% (before EGTA or (S)-AMPA treatment).

APP-YFP Imaging and Analysis: Rat hippocampal neurons (3 div) were infected with adenoviruses expressing APP-YFP and R21Q-mRFP at viral concentrations that were empirically derived. On day 6, neurons were treated with 25 μ M (S)-AMPA for 45 min to induce rods. After 45 min, neuronal cultures were switched to a low-fluorescence Hibernate-E-based (BrainBits) medium, supplemented with B27, GlutaMAX, and 1% pen/strep, pre-warmed to 37°C. Dual-infected neurons were imaged on a heated (37°C) stage using an Olympus IX-81 equipped with a CSU22 Yokogawa head, a 60x oil (NA 1.42) objective, and an EM-CCD Cascade IIB camera (Photometrics). To image APP-YFP and R21Q-mRFP, 473 nm and 561 nm diode lasers were used, respectively. For each culture, 3-4 neurons, some which had formed rods and some which had not, were chosen for imaging. For each neuron, a single image of R21Q-mRFP was captured to indicate the presence and spatial-positions of rods. During the imaging period, R21Q-mRFP-labeled rods did not move and generally remained static for many minutes (data not shown). APP-YFP was imaged continuously for 50 frames using an exposure time of 0.23 sec (~average 4 frames/sec). To generate kymographs of APP-YFP trafficking, a 3-pixel-wide line at least 100-pixels long was drawn through the middle of neurites using Metamorph. A maximum-intensity kymograph was generated in Metamorph.

Results

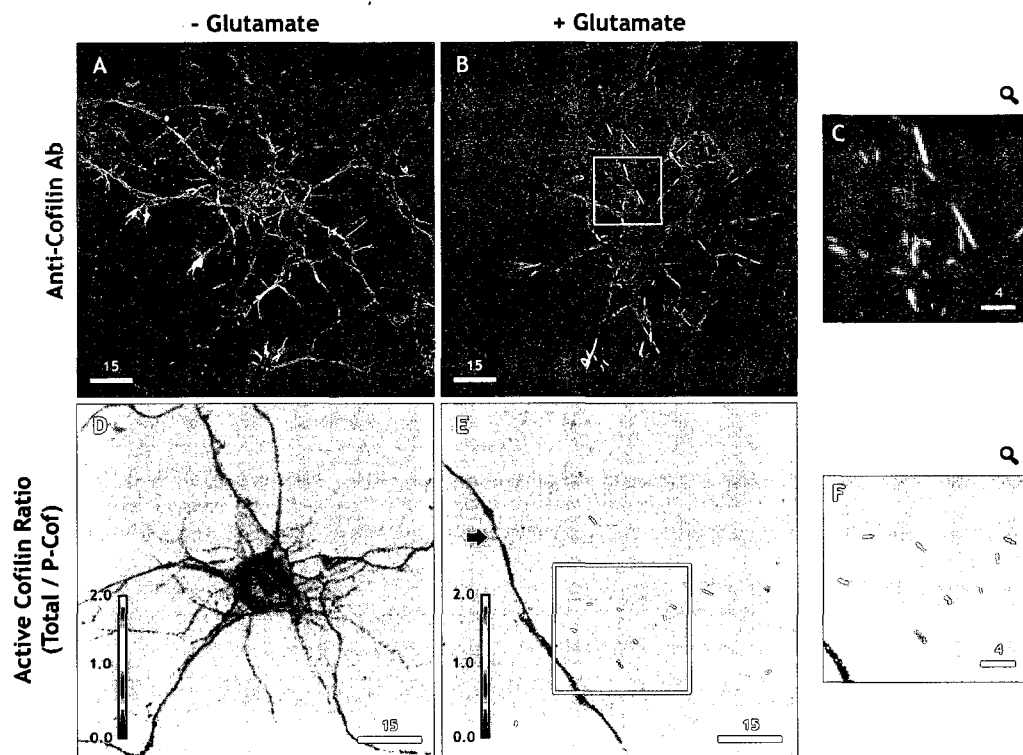
Glutamate induces cofilin-rods through cofilin dephosphorylation. Though glutamate functions as an endogenous neurotransmitter and is required for normal synaptic signaling between excitatory neurons, a high concentration of glutamate is excitotoxic (Dong *et al.*, 2009). Excitotoxic glutamate (100 μ M L-glutamate) rapidly

induced cofilin-actin rods by 30 minutes in young hippocampal neurons (6-7 *div*) (Figure 4.1B), confirming previous results (Minamide *et al.*, 2000). In general, rod formation requires dephosphorylation of cofilin at serine-3 (Minamide *et al.*, 2000; Maloney *et al.*, 2005; Huang *et al.*, 2008; Kim *et al.*, 2009). To determine whether cofilin is also dephosphorylated in response to excitotoxic glutamate, neurons were co-stained using a phospho-specific ADF/cofilin antibody, 4317, and a total cofilin antibody, mAB22. Phospho-ratio staining revealed that excitotoxic glutamate induced a global dephosphorylation of cofilin as compared to phospho-ratios observed in control neurons, and cofilin-actin rods contained dephosphorylated cofilin (Figure 4.1D).

Glutamate-induced cofilin-rod formation requires AMPA receptors. As a neurotransmitter, glutamate can bind to multiple classes of glutamate receptor types, which include AMPARs, NMDARs, and metabotropic GluRs (mGluRs) (Michaelis, 1998). Therefore, to establish the signaling requirements for glutamate-induced rod formation, we determined which glutamate receptor types were involved. For this, we used GluR-type-specific antagonists and agonists to either prevent or induce rods, respectively. AMPARs, NMDARs, and group I mGluRs were considered because of their postsynaptic localization. Both AMPARs and NMDARs are tetrameric cation-selective ionotropic receptors (Jin *et al.*, 2009), which exhibit differential selectivity for certain cations. AMPARs permit Na⁺-flux whereas NMDARs also permit Ca²⁺-flux, although exceptions to these generalizations exist (Wollmuth and Sakmann, 1998). For instance, a single amino acid in the pore region of AMPARs controls Ca²⁺-permeability (Köhler *et al.*, 1993), which is developmentally-regulated (Liu and Zukin, 2007). NMDARs are also

Figure 4.1. Glutamate excitotoxicity (100 μ M) induces cofilin-actin rods.

(A.) In untreated rat hippocampal neurons cultured for 5-7 days in vitro (div), cofilin, which is immunostained with an anti-cofilin antibody (1439), is generally distributed throughout the neuron and can be localized to the soma and neurites. Otherwise, cofilin is enriched at sites of dynamic actin structures, including growth cones and filopodia. (B.) High concentrations of glutamate (glutamate excitotoxicity, 100 μ M) induce the aggregation of cofilin-saturated actin filaments into cofilin-rods. (C.) Magnified view of region (white box) in *panel B*. (D.) In untreated neurons, the relative level of dephosphorylated cofilin (active) is lower than in neurons that have formed rods in response to excitotoxic glutamate treatment (compare to *panel E*). In the neuron in *panel D*, the average ratio of dephospho-cofilin over the soma is ~ 0.75 . The background ratio is normalized to 1.0 in both *panels D and E*. (E., F.) In cofilin-rods, the relative level of dephosphorylated (active) cofilin is high and in some areas is 2-fold greater than control ratio-levels. Note that a neurite (see arrow in *panel E*) originating from a nearby neuron, which did not form rods, maintains a dephospho-cofilin ratio similar to untreated neurons (< 1.0). Scale bar - All numbers are in μ m.

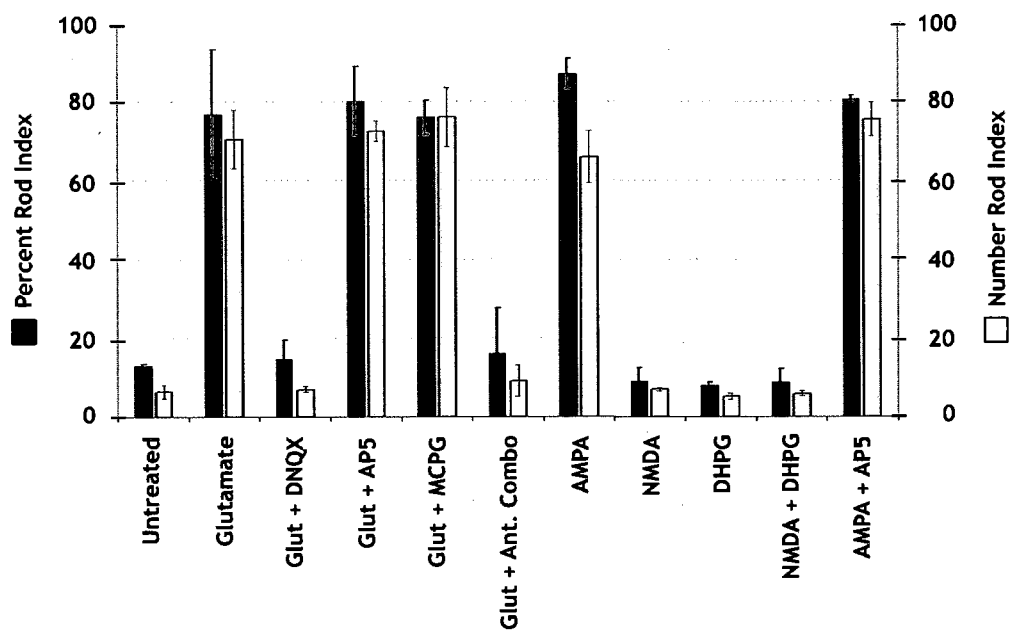


different from AMPARs in that they require coincident membrane-depolarization with ligand-binding due to a Mg^{2+} -dependent block of the channel (Sakurada *et al.*, 1993). Group I mGluRs are G-protein coupled and indirectly activate phospholipase C through G-protein signaling (Hannan *et al.*, 2001).

Because cofilin-rods occur idiopathically albeit at a low frequency in untreated cultures, the presence of rods alone could not be used to assess rod induction *per se*. As a result, two semi-quantitative measures, percent-rod index and number-rod index, were used to assess rod induction (see *Materials and Methods* for explanation). Based on the two indices of cofilin-actin rod formation, only the AMPAR antagonist, DNQX, was able to prevent glutamate-induced rod formation (Figure 4.2). The NMDAR-antagonist, AP5, or the group I mGluR-antagonist, MCPG, proved ineffectual (Figure 4.2). In addition, all three GluR antagonists in combination did not block rod formation to a greater extent than DNQX alone. Conversely, the AMPAR agonist, (S)-AMPA, was sufficient to induce rods, which neither the NMDAR agonist, NMDA, nor the group I mGluR agonist, DHPG, could (Figure 4.2). To demonstrate that AMPA-induced cofilin-actin rod formation did not depend on an indirect relief of NMDAR channel activity by membrane-depolarization, AMPA-induced rod formation was tested with the NMDAR antagonist, AP5. AP5 did not block AMPA-induced rod formation (Figure 4.2), confirming that AMPAR activity is sufficient for cofilin-rods to form. Since AMPAR-activation alone was sufficient to induce rods, (S)-AMPA, instead of glutamate, was used to induce rods hereafter.

Figure 4.2. Glutamate-induced rod formation is AMPAR-dependent.

5-7 div rat hippocampal neurons were treated with glutamate, various glutamate-receptor-specific (GluR-specific) agonists or antagonists, or combinations of them. For experiments involving GluR-specific antagonists, neurons were pre-treated with the drug-antagonists for 15 min before adding L-glutamate (100 μ M). The following concentrations were used for the GluR-specific antagonists: (DNQX, 50 μ M), (AP5, 100 μ M), and ((R,S)-MCPG, 500 μ M). Only DNQX, the AMPAR antagonist, was able to prevent glutamate-induced rod formation. For experiments involving GluR-specific agonists, only the drug-agonist was added. The following concentrations were used for the GluR-specific agonists: (AMPA, 25 μ M), (NMDA, 100 μ M), and (DHPG, 100 μ M). AMPA treatment was sufficient to induce cofilin-actin rods, although the combination of NMDA and DHPG could not induce rods nor could AMPA-induction of rods be blocked by AP5, the NMDAR antagonist.

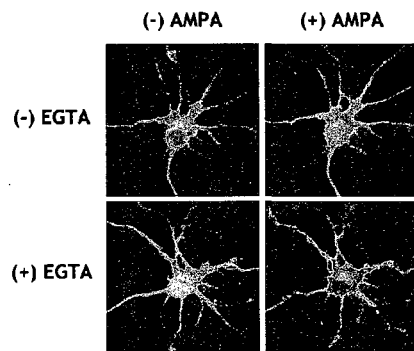


Ca²⁺ and the Ca²⁺-dependent proteins, calcineurin or calpain, are not essential for AMPA-induced cofilin-rod formation. Neurons close to amyloid plaques are unable to maintain normal cytoplasmic Ca²⁺ levels, leading to “Ca²⁺ overload” and neurite dystrophy (Kuchibhotla *et al.*, 2008). These effects can be prevented by inhibiting the Ca²⁺-dependent phosphatase, calcineurin, demonstrating the importance of Ca²⁺-dysregulation in AD pathology (Kuchibhotla *et al.*, 2008). AMPAR-activation can trigger sustained increases in cytoplasmic calcium from multiple sources, including through AMPARs themselves (Liu and Zukin, 2007), or through voltage-gated calcium channels (Ho *et al.*, 2009). Calcium-dependent pathways are also known to regulate cofilin-activation and rod formation (Wang *et al.*, 2005; Homma *et al.*, 2008). Therefore, we wanted to determine whether Ca²⁺ or Ca²⁺-dependent processes might be involved in AMPA-induced rod formation. To test whether (S)-AMPA induces Ca²⁺-responses in 6-7 div rat hippocampal neurons, we performed Fura2 imaging. Rat hippocampal neurons were loaded with Fura2-AM, which is a cell-permeable analogue of Fura2 that is converted to Fura2 by cellular esterases, and treated with 25 μM (S)-AMPA, which induced a rapid, robust and sustained increase in cytoplasmic Ca²⁺ (Figure 4.3A, B). All observable Ca²⁺ increases could be blocked with EGTA (Figure 4.3A, B). However, despite its ability to prevent all observable Ca²⁺ responses, EGTA could not prevent AMPA-induced rod formation (Figure 4.3C). A selective and reversible calcium-permeable AMPAR antagonist, IEM-1460, also could not block rod formation (data not shown). Because transient Ca²⁺ responses might escape detection with Fura2 imaging or Ca²⁺-chelation might only dampen but not eliminate Ca²⁺ influxes entirely, we further

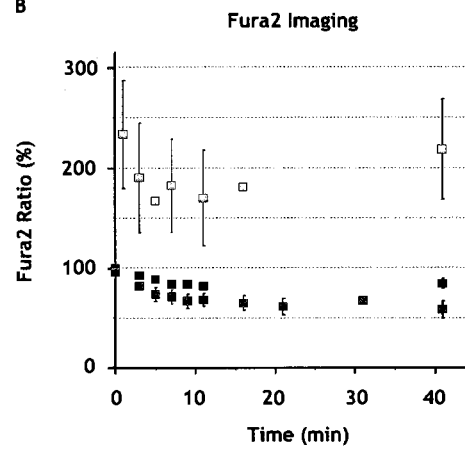
Figure 4.3. Ca^{2+} or the Ca^{2+} -dependent proteins, calcineurin or calpain, are not essential for AMPA-induced rod formation.

(A.) Rat hippocampal neurons were loaded with Fura2-AM, which is de-esterified to Fura2 by cellular esterases, for Ca^{2+} imaging. The peak excitation wavelength of Fura2 shifts to 380 nm from 340 nm upon Ca^{2+} binding; thus, a larger (380/340) ratio indicates higher Ca^{2+} concentrations. Each panel shown indicates a (380/340) ratio image. Before AMPA treatment, 380- and 340-nm images were captured for each neuron to establish a baseline (380/340) ratio, which was then normalized to 100%. (S)-AMPA treatment induces a rapid and robust Ca^{2+} response in hippocampal neurons (see *top panels [post-AMPA ratio: 155; pre-AMPA ratio: 95]*), which can be blocked by EGTA pre-treatment (see *bottom panels [post-AMPA ratio: 113; pre-AMPA ratio: 86]*). (B.) Quantification of Fura2 (380/340) ratio over over a total of 45 min at various timepoints: 2.5, 5, 7.5, 10, 15, 40 min. 25 μM (S)-AMPA (*red squares*) treatment induces a rapid increase in cytoplasmic Ca^{2+} , which is sustained over 45 min (Ca^{2+} overload). The Fura2 ratio actually decreases in untreated neurons over this same timeframe (*blue squares*). 6 mM EGTA pre-treatment (*green squares*) blocks all Ca^{2+} responses induced by (S)-AMPA treatment. The Fura2 ratio for EGTA-treated neurons is lower than that observed for untreated neurons. (C.) 5-7 div rat hippocampal neurons were pre-treated with EGTA (6 mM) or various drug-inhibitors before treating with 25 μM (S)-AMPA to test whether rod formation could be blocked. The following drug inhibitors were used at the following concentrations: (Cyclosporin A, 20 μM), (FK-506, 25 μM), (ALLN, 50 μM), (E-64d, 15 μM). Neither EGTA pre-treatment nor any of the drug-inhibitors tested prevented rod formation.

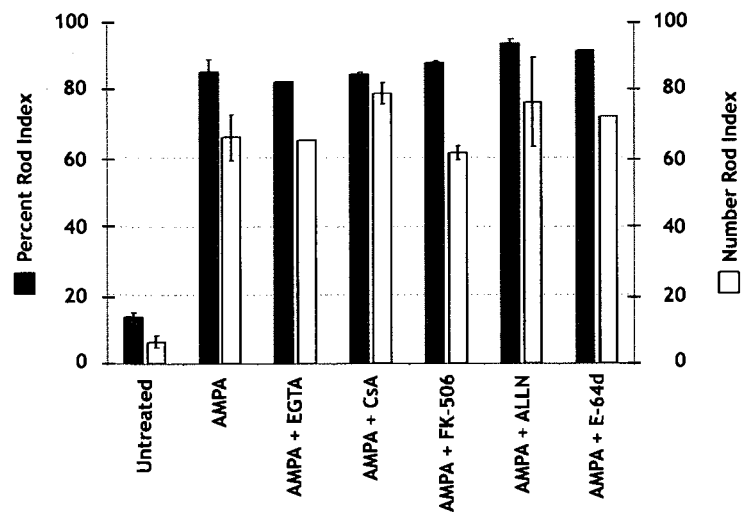
A



B



C



assayed for calcium-independence by testing the involvement of calcium-dependent proteins that have been implicated in AD and glutamate excitotoxicity as well as being able to mediate cofilin-activation. To inhibit calcineurin, a Ca^{2+} -dependent phosphatase that can activate slingshot (Wang *et al.*, 2005), two mechanistically-distinct inhibitors were tested. Cyclosporin A (CsA) inhibits calcineurin by forming an inhibitory complex with the protein cyclophilin A (Ke and Huai, 2003). FK-506 inhibits calcineurin by forming an inhibitory complex with the protein FK binding protein-12 (FKBP-12) (Ke and Huai, 2003). Neither CsA nor FK-506, used at concentrations known to inhibit calcineurin (Faure *et al.*, 2007; Misonou *et al.*, 2007), prevented AMPA-induced rod formation (Figure 4.3C). Likewise, two mechanistically-distinct inhibitors of calpains, Ca^{2+} -dependent proteases, were tested. ALLN is a cell-permeable peptide that competitively inhibits calpains (Song *et al.*, 1994). E-64d is an irreversible chemical inhibitor of calpains (Tamai *et al.*, 1986). Neither ALLN nor E-64d blocked AMPA-induced rod formation (Figure 4.3C). These results demonstrate that Ca^{2+} and the Ca^{2+} -dependent proteins tested are not essential for AMPA-induced rod induction.

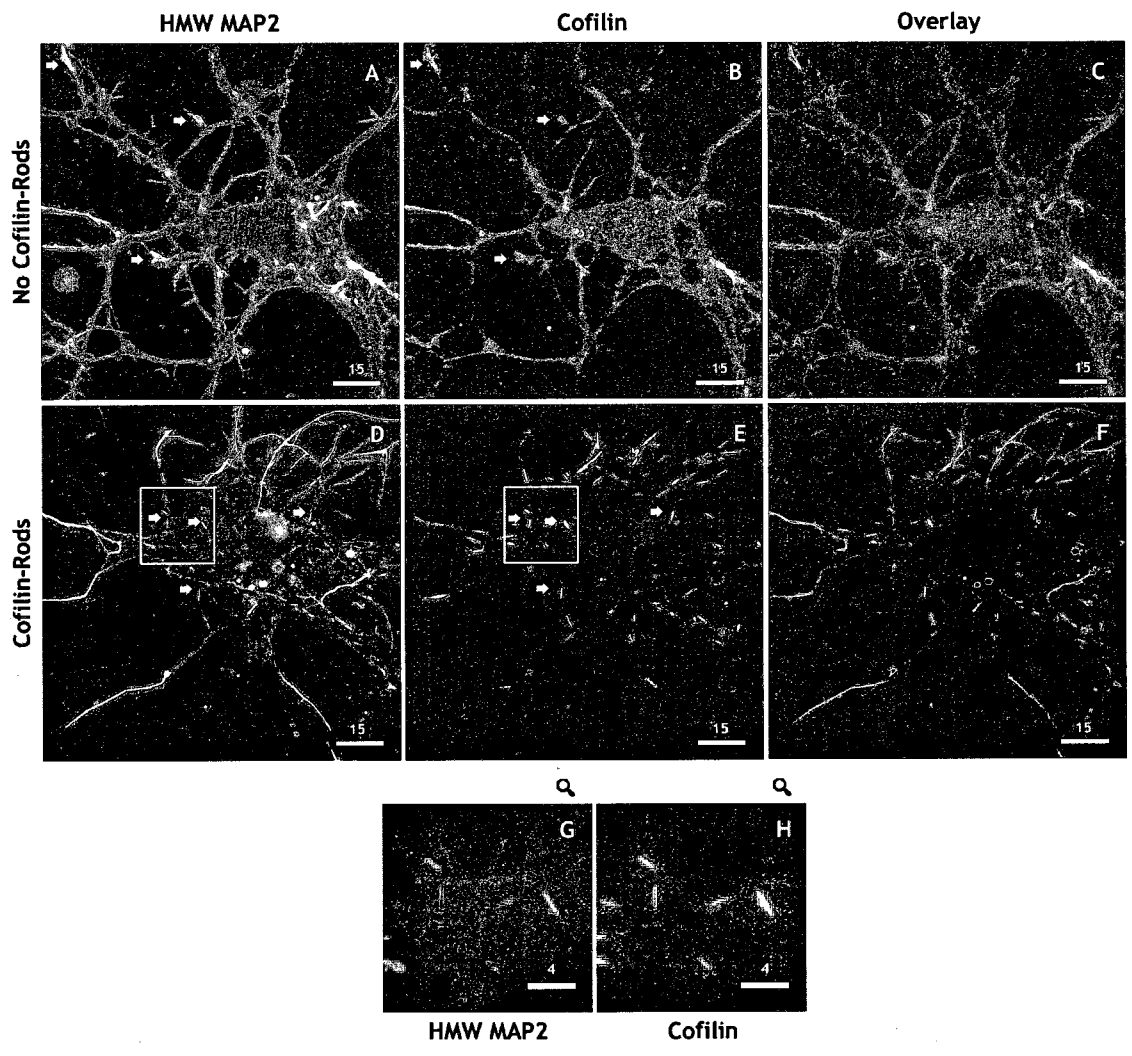
HMW MAP2s weakly co-localize with AMPA-induced rods. In chick tectal neurons treated with antimycin (energy stress) or peroxide (reactive-oxygen species), 12E8-immunopositive tau aggregates form rapidly and co-localize with cofilin-rods. 12E8 recognizes two phospho-epitopes of tau within its microtubule binding domains (Seubert *et al.*, 1995). However, considering that tau is unable to bind directly to actin (Roger *et al.*, 2004), and has not been reported to interact with cofilin, it is unclear how tau localizes to rods. Other MAPs, however, such as high molecular-weight (HMW)

MAP2 isoforms, can bind directly to actin filaments (Caceres *et al.*, 1988; Morales and Fifkova, 1989); thus their localization to rods might be expected. Therefore, we tested to see whether HMW MAP2 isoforms also co-localize with rods induced by (S)-AMPA treatment. We focused on the HMW MAP2s not only because of their known actin-binding capabilities but the HMW MAP2 isoforms also contain an N-terminal projection domain that is absent from tau and the shorter isoforms of MAP2, permitting its unequivocal discrimination from these other isoforms. Since our HMW MAP2 antibody is targeted to this unique projection domain, cross-reactivity with other MAP2 isoforms is not anticipated. After (S)-AMPA treatment, HMW MAP2 staining increased in neurites, which was generally contiguous throughout the neurite (Figure 4.4D). However, in some neurons, HMW MAP2 staining was intermittent, though this only represented a minority of the neurons that formed rods (data not shown). Because HMW MAP2 staining was increased in neurites, where rods also form, and generally contiguous, *bona fide* co-localization of HMW MAP2s with rods was difficult to assess. Nevertheless, in some cases, unequivocal co-localization could be observed, thereby suggesting an interaction between HMW MAP2s and cofilin-actin rods (Figure 4.4G, H).

R21Q cofilin mutant exhibits reduced rod formation and actin binding. The R21Q cofilin mutant was originally identified in a mutagenesis screen for cofilin mutants that did not form cofilin-actin rods when overexpressed in cells. HeLa cells do not normally form endogenous cofilin-actin rods, due to low expression levels of cofilin, but can form rods when cofilin is overexpressed. We virally expressed WT or the R21Q mutant of cofilin, which were C-terminal chimeras with mRFP, in HeLa cells and treated with

Figure 4.4. High molecular-weight (HMW) isoforms of MAP2 (isoforms a/b) weakly co-localize with rods.

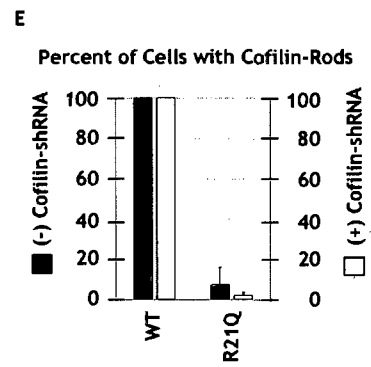
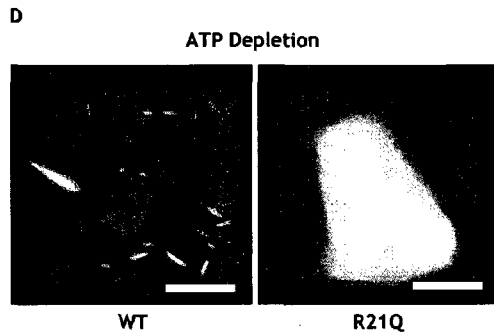
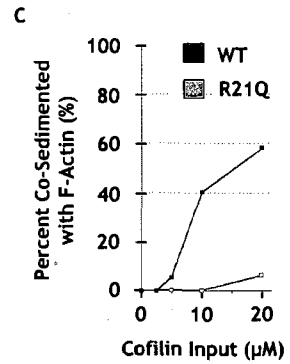
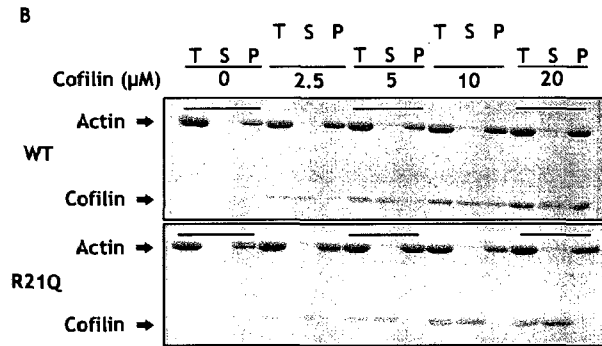
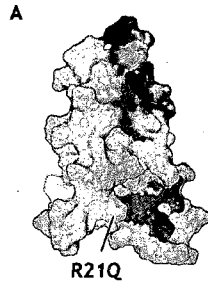
Cofilin-actin rods were induced in 5-7 div rat hippocampal neurons with 25 μ M (S)-AMPA. After AMPA-treatment for 45 min, neurons were fixed and co-immunostained for HMW MAP2 (a/b) and cofilin. (A.) In untreated neurons, HMW MAP2s are enriched at dynamic actin-rich regions (see arrows in *panel A*), especially growth cones, where cofilin is also enriched (see arrows in *panel B*). (C.) An overlay of anti-HMW MAP2 staining with anti-cofilin staining. Yellow regions indicate co-localization. (D.) In neurons treated with 25 μ M (S)-AMPA, HMW MAP2 expression and its localization to neurites is increased. Arrows (yellow) highlight regions where HMW MAP2 distinctly co-localizes with cofilin (see *panels G and H*). (G, H.) Magnified view of region in *panel D and E* better demonstrates distinct co-localization of HMW MAP2 with rods (compare *panels G, H*). Scale bars – All numbers are in μ m.



ATP-depleting solution to induce rods. With WT cofilin overexpression, virtually all cells formed rods (Figure 4.5D, E). In contrast, the R21Q cofilin mutant did not form rods except in a small fraction of cells (Figure 4.5D, E). Overexpressed R21Q did not form cofilin-rods whether endogenous cofilin was knocked down or not (Figure 4.5E). Because the residue, R21, lies near a region involved in F-actin binding (Figure 4.5A), we asked whether the mutation might perturb its interaction with F-actin, which could also explain its reduced ability to form rods. We performed a F-actin co-sedimentation assay with the R21Q cofilin mutant and wild type (WT) cofilin with varying concentrations of cofilin (Figure 4.5B). The R21Q cofilin mutant binds to F-actin less efficiently than WT cofilin does by ~9-fold (Figure 4.5C).

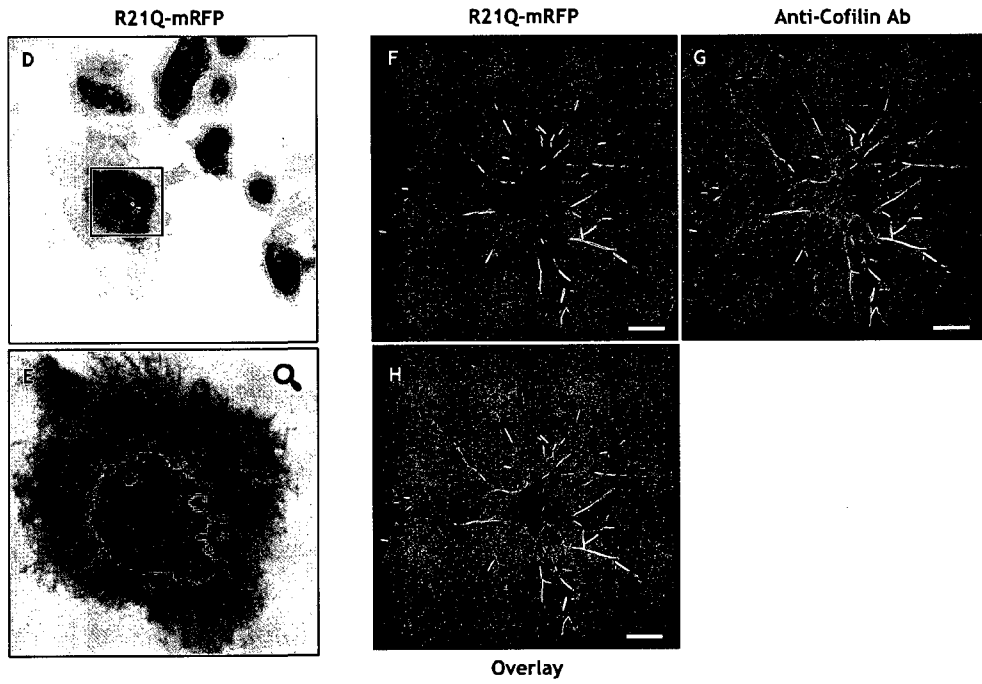
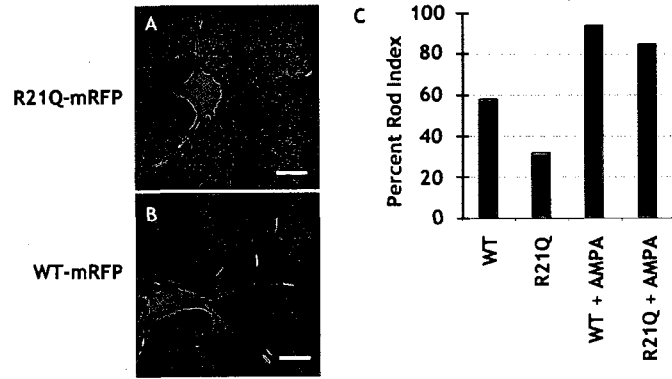
R21Q cofilin mutant incorporates into rods formed from endogenous cofilin but forms less spontaneous rods induced by overexpression than WT cofilin. The study of cofilin-actin rod formation in live neurons has been limited because overexpression of a fluorescent protein-tagged WT cofilin results in considerable spontaneous cofilin-rod formation (spontaneous rods). A fluorescent cofilin mutant that could incorporate into induced rods but not form spontaneous rods would offer a useful alternative for live-cell imaging. Therefore, we asked whether R21Q, which does not form rods by itself, could incorporate into rods made from endogenous cofilin (endogenous rods). For these studies, we used A431 cells, which when stressed can form rods due to high endogenous expression levels of cofilin. When overexpressed in A431 cells, which were induced to form rods by treating with ATP-depleting solution, cofilin R21Q-mRFP incorporated into endogenous rods (Figure 4.6D, E). To be useful as a live-cell reporter for rod formation,

Figure 4.5. The R21Q cofilin mutant exhibits reduced actin binding and rod formation. The R21Q mutant was identified in a mutagenesis screen for cofilin-mutants that did not form cofilin-actin rods when overexpressed in HeLa cells. (A.) The residue, R21, lies near a region involved in F-actin binding. The colored regions correspond to: (Green: G- and F-actin binding), (Red: F-actin binding), (Yellow: Nuclear Localization Signal, NLS), (Pink: Phospho-regulated Serine-3), (Blue: N-terminus). The 3-D structure of cofilin was generated in PyMol using NMR data of human cofilin (PDB: 1Q8G). (B.) Compared to WT cofilin, R21Q cofilin binds to F-actin less efficiently. WT and R21Q cofilin were bacterially expressed and purified as untagged proteins. For the co-sedimentation assays, various concentrations of cofilin (0, 2.5, 5, 10, 20 μ M) were incubated with 5 μ M F-actin and the samples were centrifuged at 250,000 x g for 30 minutes at 20°C. For each concentration of cofilin assayed, three samples, which represented the sample before centrifugation (T), the supernatant after centrifugation (S), and the pellet after centrifugation (P) were loaded on to a 15% SDS-PAGE gel. Both gels were stained using Coomassie Blue R. (C.) Quantification of the results from *panel B*. For each cofilin concentration assayed, the percent of the total cofilin (S + P) that co-sedimented with the pellet-fraction (P) was calculated using the formula, $P / (S+P)$. The R21Q mutant co-sediments with F-actin ~9-fold less well than WT cofilin does. Quantification was done using Metamorph. (D.) The R21Q cofilin mutant does not form rods by itself. Representative images of rods formed in A4.8 cells overexpressing either WT or mutant cofilin, which C-terminal chimeras with mRFP, and treated with ATP-depleting medium (NaN_3 + 2-deoxyglucose). A4.8 cells do not form rods unless exogenous cofilin is overexpressed. Scale bar = 10 μ m. (E.) Quantification of the percent of A4.8 cells that formed cofilin-rods when either WT or R21Q cofilins were overexpressed and endogenous cofilin was or was not knocked-down using a virally-expressed shRNA. Whether or not endogenous cofilin was knocked-down, WT cofilin formed cofilin-rods in all A4.8 cells imaged, and the R21Q cofilin mutant formed cofilin-rods in only a small fraction of cells imaged.



All data was provided courtesy of Alisa E. Shaw

Figure 4.6. The R21Q cofilin mutant incorporates into endogenous cofilin-actin rods but forms less spontaneous rods than WT-cofilin. WT and R21Q cofilin are C-terminal chimeras with monomeric RFP (mRFP). (A, B.) Both R21Q and WT cofilin form rods due to overexpression (spontaneous rods), although rods generated by overexpressing WT cofilin are generally more numerous and larger in size. (C.) Only neurons overexpressing either WT or R21Q cofilin were included in the analysis. The fraction of neurons that formed spontaneous rods is significantly lower for R21Q overexpression than WT overexpression. However, the fraction of neurons that formed rods in response to (S)-AMPA treatment (25 μ M) was similar for both R21Q and WT overexpressing neurons. (n = 1) (D.) R21Q incorporates into rods formed from endogenous cofilin and generated by energy stress (ATP-depleting medium) in A431 cells. (E.) Magnified view of region selected in *panel D*. (F, G, H.) R21Q incorporates into nearly all induced rods detected by immunostaining using the anti-cofilin Ab, 1439. Yellow regions indicate co-localization (see *panel H*). All scale bars = 15 μ m.



the R21Q-mRFP cofilin mutant must incorporate into all endogenous cofilin-actin rods formed. To determine its fidelity for detecting rods, we infected rat hippocampal neurons with R21Q-mRFP, induced endogenous rods with (S)-AMPA treatment, and also immunostained for rods using a secondary fluorophore that is spectrally well-separated from mRFP. Virtually all rods detected by immunostaining also contained R21Q-mRFP (Figure 4.6F, G, H), demonstrating its high fidelity. Very rarely was co-localization not observed, though we attribute this to the stochastic nature of cofilin incorporation. To demonstrate that R21Q overexpression does not form spontaneous rods, we quantified the percent-rod index only for neurons that were overexpressing WT-mRFP or R21Q-mRFP cofilin (Figure 4.6A, B). In untreated neurons, the percent-rod index was reduced by nearly half for R21Q-mRFP-overexpressing neurons as compared to those that overexpressed WT cofilin. Still, the percent-rod index for R21Q-overexpressing neurons was greater than uninfected controls (~14% for uninfected cultures) (Figure 4.6C). The former result was expected based on the previous observation that R21Q does not form rods by itself. However, the percent-rod index was similar between R21Q and WT cofilin in AMPA-treated neurons (Figure 4.6C), confirming its ability to incorporate weakly into rods formed from endogenous proteins.

Neither WT MAP2c nor its phosphorylation mutants co-localize with rods in ATP-depleted A431 cells. In addition to the HMW MAP2s, MAP2c is known to bind to and bundle actin filaments (Ozer and Halpain, 2000). Actin binding is promoted by phosphorylation of any of three serine residues, S319, S350, and S382, which reside in the 1st, 2nd, and 3rd microtubule binding domains (MTBD) of MAP2c respectively (Ozer

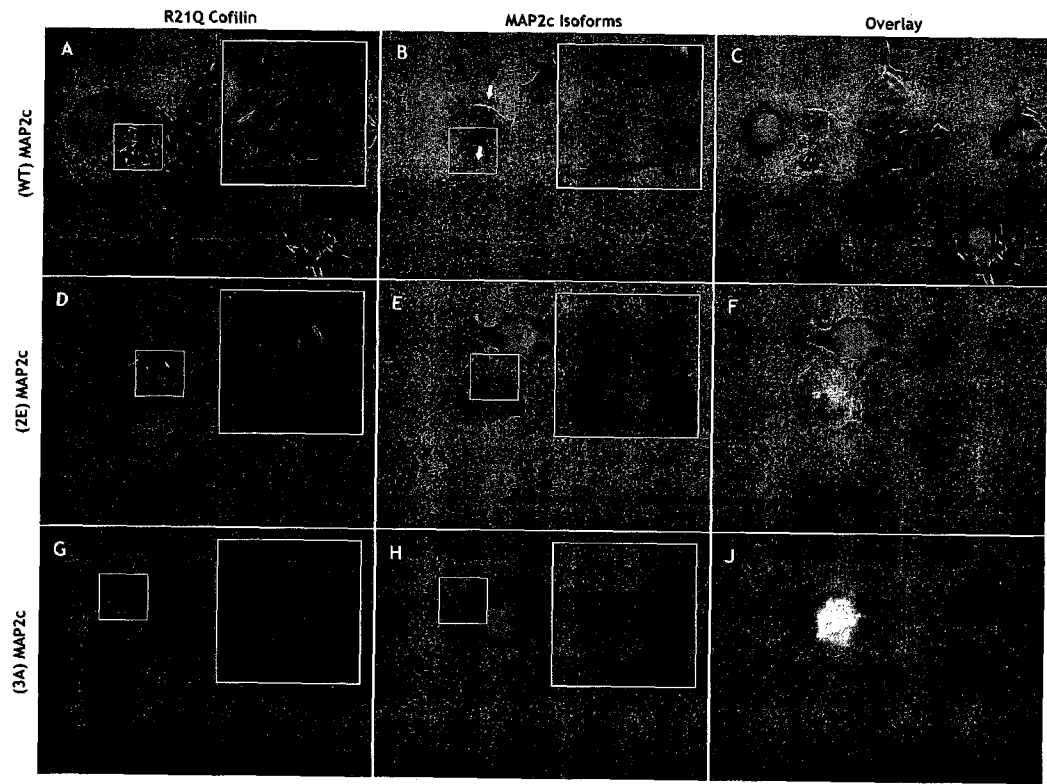
and Halpain, 2000). Reciprocally, phosphorylation of any of these residues reduces microtubule binding (Ozer and Halpain, 2000). Therefore, we wanted to determine whether WT or a phospho-mimetic mutant of MAP2c co-localized with rods through its ability to bind to actin. Overexpression of wild-type MAP2c resulted in extensive and abnormal microtubule bundling (Figure 4.7B, arrows), in agreement with previous observations (Ozer and Halpain, 2000). Also, as previously observed (Ozer and Halpain, 2000), a double phospho-mimetic mutant of MAP2c (2E), in which residues S350 and S382 were mutated to glutamate, did not induce the bundling of microtubules and appeared to be more diffusely distributed (Figure 4.7E). Nevertheless, the 2E mutant of MAP2c localized to microtubules (Figure 4.7K). Surprisingly, triple mutation of the three serine residues to alanine (3A) also did not induce extensive bundling of microtubules (Figure 4.7H, though microtubule localization was observed (Figure 4.7L). Microtubule binding appeared to be unaffected by ATP depletion for any of the MAP2c constructs investigated, at least within the timeframe of the study (2 hrs). In addition, none of the MAP2c constructs appeared to co-localize with rods (compare insets of Figure 4.7A, D, and G with 4.7B, E, and H, respectively).

The presence of cofilin-actin rods is associated with a loss of trafficking of APP-YFP-containing vesicles. The amyloid precursor protein, APP, is trafficked anterogradely from the trans-Golgi network to the plasma membrane and retrogradely within recycling endosomes for lysosomal degradation (Ehehalt *et al.*, 2003; Thinakaran and Koo, 2008). Within endosomes, APP is preferentially processed by β -secretases (Ehehalt *et al.*, 2003), generating more $A\beta_{1-42}$, whereas α -secretase cleavage, which generates a non-

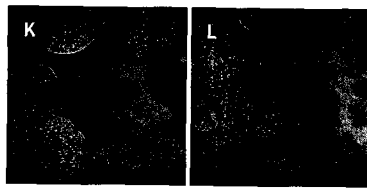
Figure 4.7. Neither WT MAP2c nor its phosphorylation-mutants co-localize with rods in ATP-depleted A431 cells.

A431 cells overexpressing EGFP-tagged wild type or phosphorylation mutants of MAP2c were treated with ATP depleting solution (10 mM NaN₃, 6 mM 2-deoxyglucose) for ~2 hours to induce rods. Rods were detected by overexpressing mRFP-tagged R21Q cofilin (see *panels A, D, G*). Overexpression of WT MAP2c alone induced the bundling of microtubules (*arrows*), which were not affected by ATP depletion (see *panel B*).

Overexpression of the double phospho-mimetic mutant of MAP2c (2E) did not induce bundling of microtubules and was more diffusely distributed throughout the cell (see *panel E*), though it still localized to microtubules (see *panel K*). Likewise, the triple-non-phosphorylatable mutant of MAP2c (3A) did not induce bundling of microtubules (see *panel H*), which was unexpected. The 3A MAP2c mutant localized to microtubules as well (see *panel L*). None of the MAP2c isoforms studied co-localized with rods, which were induced by ATP depletion. Panels A-J were collected using a 20x objective whereas panels K and L were collected using a 60x objective.



Microtubule
Localization



(2E) MAP2c

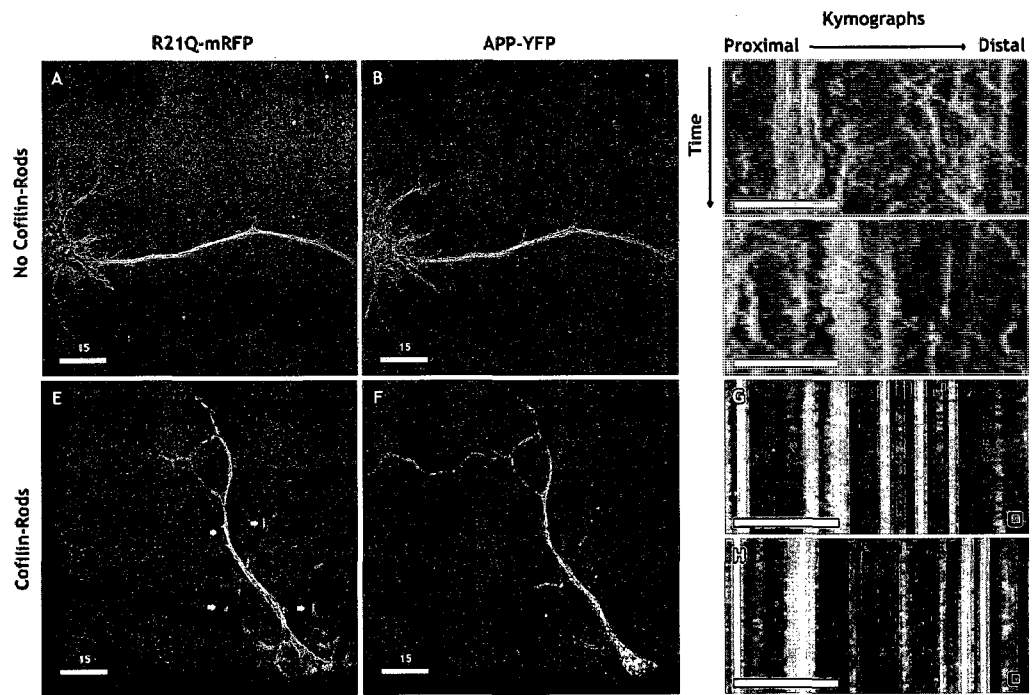
(3A) MAP2c

60x Objective

amyloidogenic peptide, is preferred when APP is expressed on the plasma membrane (Thinakaran and Koo, 2008). Because amyloidogenic processing of APP is preferred in trafficking endosomes, it has been hypothesized that localized stalling or the loss of vesicle trafficking might facilitate the increased production and secretion of A β ₁₋₄₂ (Stokin *et al.*, 2005; Pigino *et al.*, 2009). Supporting evidence for this was provided by the localization of APP and its cleavage products to the distal ends of A β ₁₋₄₂-induced rods (Maloney *et al.*, 2005); however, conspicuous vesicle stalling or loss of trafficking has not been observed in live-cell imaging to date. Therefore, we wanted to determine whether rod formation was associated with changes to the trafficking of APP-YFP-containing vesicles. Rat hippocampal neurons overexpressing both R21Q-mRFP, to image rods, and APP-YFP, which were trafficked in vesicles, were treated with 25 μ M (S)-AMPA for 45 min to induce rods before live-cell imaging. The fact that not all neurons formed rods allowed us to compare the dynamics of APP-YFP-containing vesicle trafficking in neurons that did or did not form rods. In neurons that did not form cofilin-actin rods, APP-YFP-containing vesicles were highly dynamic in nearly all neurite-processes observed, including in presumptive dendrites and axons (Figure 4.8B, C, D). In neurons that formed rods, a global loss of trafficking of APP-YFP-containing vesicles was observed (Figure 4.8F, G, H), with APP-YFP-containing vesicles also appearing to aggregate into static punctae along neurites (Figure 4.8F). The formation of rods in any one particular neurite was typically associated with the loss of trafficking throughout the entire neuron, even in neurites that did not contain a rod (Figure 4.8F).

Figure 4.8. The presence of cofilin-actin rods is associated with a loss of trafficking of APP-YFP-containing vesicles.

R21Q-mRFP and APP-YFP dual-infected cultures were treated with 25 μ M (S)-AMPA for 45 min before imaging. R21Q-mRFP and APP-YFP dual-positive neurons, which formed or did not form rods, were imaged continuously for 50 frames. A single red-channel image was taken to indicate the positions of rods before continuous imaging of the YFP-channel. Maximum-intensity kymographs were generated using a 3-pixel-wide line at least 100-pixels long drawn in the middle of a neurite. Time between frames (and therefore between rows in kymographs) is \sim 0.23 sec (duration of image-capture only). (A, B.) In AMPA-treated neurons that did not form rods, APP-YFP-containing vesicles remain dynamic, as indicated by the leftward (retrograde) and rightward (anterograde) movements of APP-YFP-containing vesicles in the kymographs (see *panels C, D*). Color of square in lower right-hand corner of kymographs corresponds to linescans of same color in *panel B*. (E, F.) In neurons that formed rods (indicated by yellow arrows), APP-YFP-containing vesicles are no longer dynamic (see *panels G, H*). Color of square in lower right-hand corner of kymographs corresponds to linescans of same color in *panel F*. Scale bar in panels C, D, G, H = 8 μ m.



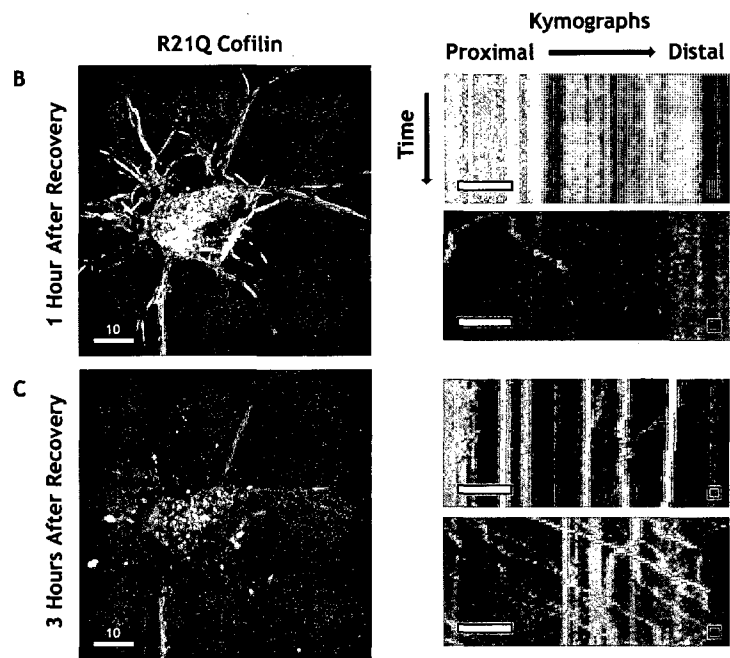
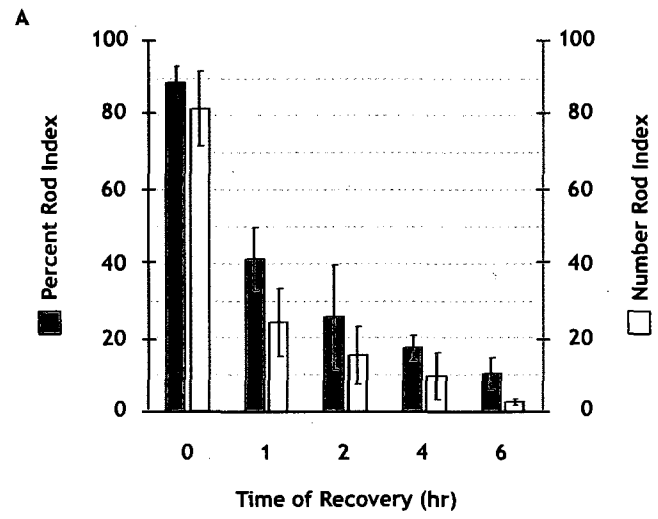
The reversal of AMPA-induced rods is associated with the recovery of trafficking of APP-YFP-containing vesicles. To establish whether AMPA-induced rods can be reversed, we blocked AMPAR-activation by adding 10 μ M DNQX to neurons, in which rods had already been induced, for variable amounts of time (0-6 hrs). Rods induced by AMPA-treatment are rapidly reversed, though only returned back to near-control levels by 6 hrs after adding DNQX (Figure 4.9A).

To determine whether the reversal of AMPA-induced rods was also associated with the resumption of trafficking of APP-YFP-containing vesicles, we imaged rods and APP-YFP in neurons that had formed rods over several hours after treating with DNQX. The reversal of rods 3 hrs after treating with DNQX was associated with the resumption of trafficking of APP-YFP-containing vesicles, although to different degrees within individual neurites (Figure 4.9C, kymographs). Conversely, the presence of rods within the same neurites only 1 hr after treating with DNQX was associated with the persistent disruption of APP-YFP-containing vesicle transport (Figure 4.9B, kymographs). In some cases, the reversal of rods was not associated with the resumption of vesicle trafficking containing APP-YFP within 3 hrs after DNQX treatment (data not shown).

AMPA induces the formation of rod-shaped cofilin aggregates in the CA3 region of organotypic hippocampal slices. Rods are induced in organotypic hippocampal slices by ATP depletion, $A\beta_{1-42}$, and glutamate treatment, though the degree of induction and regional-specificity vary for each treatment (Davis et al., 2009). Using glutamate to treat hippocampal slices, however, is confounded by the ability of glial cells to buffer the extracellular glutamate concentration through glutamate transporters. Therefore, to study

Figure 4.9. Reversal of AMPA-induced cofilin-rods is associated with the recovery of APP-YFP-containing vesicle transport.

(A.) Rat hippocampal neurons were treated with 25 μ M (S)-AMPA for 30 min to induce cofilin-actin rods. At various times before fixation, 0, 1, 2, 4, and 6 hrs, 10 μ M DNQX was added to prevent further AMPAR activation and permit recovery of rods. Though some rods reversed rapidly within the first hour, other rods persisted for up to 4 hrs after adding DNQX. (B.) Rat hippocampal neurons were treated with 25 μ M (S)-AMPA for 30 minutes to induce rods. Following AMPA treatment, neurons were washed once with fresh medium and then treated with 10 μ M DNQX to prevent further AMPAR activation (0 hr recovery). +1 hr after recovery, rods, which were detected by overexpressing the R21Q cofilin mutant, were still present (see *panel B, left*). In the same neuron (*blue and red line-scans*), APP-YFP-containing vesicles were generally not dynamic, although few exceptions were observed (see *panel B, right-upper and -lower*). (C.) +3 hrs after recovery, most rods have disappeared (see *panel C, left*). In the same approximate line-scans as shown in *panel B*, APP-YFP-containing vesicles are now more dynamic (see *panel C, right-upper and -lower*). Line-scans in *panel B and C* are not identical due to slight morphological changes that occur during recovery. The color of squares in the lower right-hand corner of kymographs corresponds to line-scans in *panels B and C*. Scale bars in kymographs = 5 μ m.

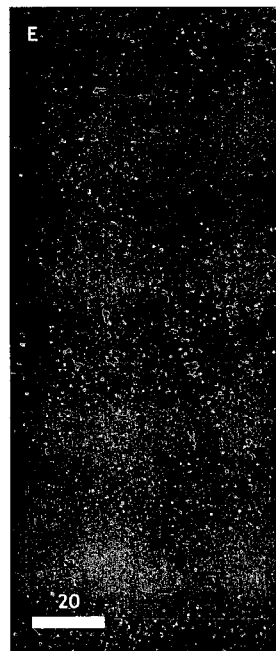
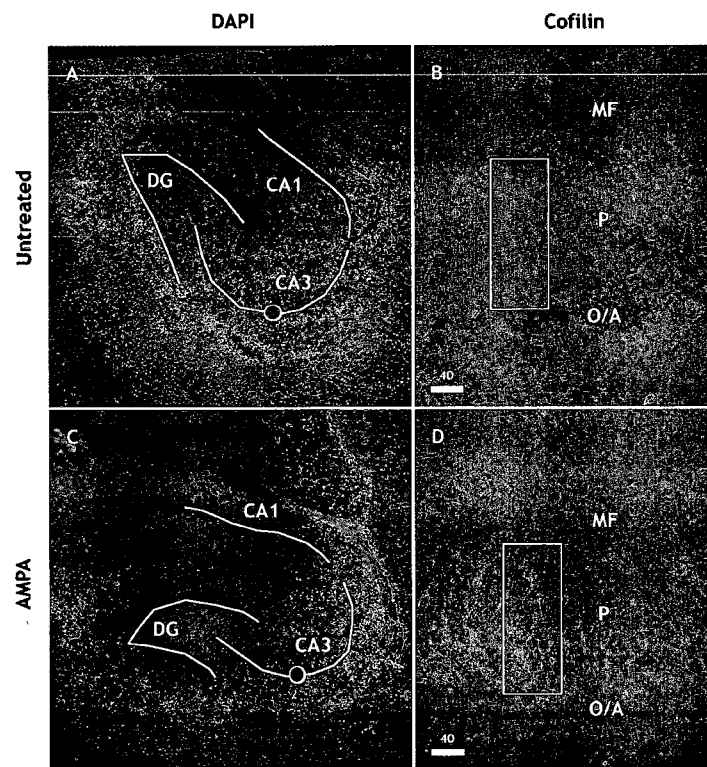


rod-induction mechanisms in hippocampal slices, treating with glutamate-specific agonists, like (S)-AMPA, is preferred because unlike glutamate, glutamate-specific agonists are not easily removed from the extracellular space through reuptake mechanisms. Treating organotypic slices with 25 μ M (S)-AMPA for 1 hr induced the formation of rod-shaped cofilin-immunoreactive aggregates in various regions throughout the hippocampus, including within the dentate gyrus, CA3, and CA1 regions (data not shown). Cofilin-immunoreactivity in untreated slices appeared as round puncta (Figure 4.10E). Though rod-shaped cofilin aggregates were observed throughout the hippocampus, we concentrated on the CA3 region because rods within this region were blocked by DNQX (data not shown); whereas, rods in other regions could not be blocked by DNQX treatment. Within the CA3 region, the formation of rod-shaped cofilin aggregates largely occurs just outside the layer of pyramidal neurons (P, Figure 4.10D), particularly in the oriens/alveus (O/A) layer.

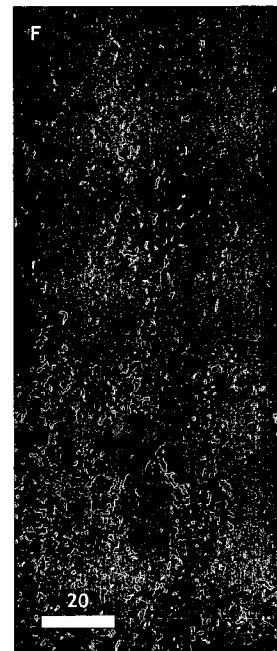
Discussion

Here we have used glutamate excitotoxicity as a model system for cofilin pathology in AD, and have determined the receptor signaling requirements of glutamate-induced cofilin-actin rod formation in young hippocampal neurons. We have demonstrated that glutamate-induced rod formation is AMPAR-dependent. Though AMPAR-activation is known to directly mediate neurotoxicity (Mahajan and Ziff, 2007), glutamate-mediated effects in AD generally depend on NMDARs or group I mGluRs (Li *et al.*, 2009). AMPARs are also unlikely to be involved in AD-related excitotoxic effects because AMPAR postsynaptic expression is reduced in AD brain (Chang *et al.*, 2006)

Figure 4.10. AMPA treatment induces rods in the CA3 region of rat hippocampal slices. Rat hippocampal slices were maintained on Transwell culture membranes for 1-3 wks until drug treatment (AMPA, 25 μ M for 1 hr). Each slice was immunostained for cofilin, using 1439 (anti-cofilin Ab), and stained with DAPI. For each slice, a low-magnification photo-montage of the entire slice was arranged from DAPI-stained images, which were taken with a 20x objective. A high-magnification photo-montage of the CA3 region was also arranged from cofilin-immunostained images, which were taken with a 60x objective. (A.) The distinct regions of the hippocampus can be differentiated by DAPI staining, which labeled the dense primary cell layers of the dentate gyrus (*DG*), CA3, and CA1 regions (see also *panel C*). (B.) A region of the CA3 region (*red dot*) was again imaged using a higher-magnification objective. The dense cell layer of CA3 pyramidal neurons (*P*) is evident by the relative absence of cofilin immunoreactivity. O/A – oriens/alveus; MF – mossy fiber. (D.) Rod-shaped aggregates of cofilin are induced in the CA3 region, particularly near the pyramidal cell layer (*P*), by AMPA treatment. (E, F.) Magnified views of comparable regions between untreated and AMPA-treated slices (see *panels B and D, white boxes*) better demonstrate the formation of rod-shaped aggregates in AMPA-treated slices. In untreated slices, cofilin immunostaining largely appears as round puncta. All numbers by scale bars are in μ m.



Untreated



AMPA

and A β ₁₋₄₂ suppresses AMPAR-dependent signaling through regulation of AMPAR surface expression (Gu *et al.*, 2009). However, the dependence of rod formation on other GluRs may change depending on neuronal maturity. For instance, NMDAR postsynaptic expression peaks later in culture, and a transition from AMPAR-dependent signaling to NMDAR-dependent signaling is also observed *in vivo*. Likewise, though we have also demonstrated that Ca²⁺ and the Ca²⁺-dependent proteins, calcineurin and calpain, are not essential for AMPA-induced rod formation, their involvement in rod-formation is not categorically ruled out. In fact, our preliminary studies in postnatal hippocampal slices suggest that rods can be induced by bath-treatment with the agonist, NMDA (data not shown). The signaling-dependence of rod-induction on neuronal maturity will be investigated in future studies.

Emerging evidence also suggests that disruptions to both actin- and microtubule-based processes are more pervasive than currently estimated. For instance, the actin-regulatory protein, WAVE, and the microtubule-regulatory protein, CRMP2, were recently identified as components of NFTs (Takata *et al.*, 2009). Thus, it is reasonable to suspect that a more general disruption of MAP proteins may also be occurring in AD than previously described. This is supported by our demonstration that HMW MAP2s can co-localize to rods. These effects have been hypothesized to underlie early pathological signatures of AD, such as vesicle trafficking defects and synaptic loss/modification, before neuronal loss or aggregate-formation occur. This was demonstrated by the overexpression of tau and its phosphorylation in *Drosophila* (Mudher *et al.*, 2004), which resulted in vesicle trafficking defects. In addition to the loss of vesicle trafficking, vesicles aggregate into punctae along the neurite (Mudher *et al.*, 2004). We have

observed similar effects in AMPA-treated neurons that formed rods but not in neurons without rods. In rod-forming neurons, APP-YFP-containing vesicles ceased moving and aggregated into discrete punctae along neurites. Though other possible explanations were not ruled out, for instance, depletion of cellular ATP could also account for the loss of vesicle trafficking, altogether, our results are consistent with a model whereby vesicle trafficking is disrupted by tau hyperphosphorylation and cofilin-actin rod formation. Indeed, overexpression of tau can inhibit kinesin-1 binding to microtubules (Goldbury *et al.*, 2006), and kinesin-1 has been reported to interact with APP although this interaction remains controversial (Kamal *et al.*, 2001; Lazarov *et al.*, 2005).

Early tau pathologies can be reversed by antibody-mediated clearance of A β ₁₋₄₂, though late tau pathologies are persistent (Oddo *et al.*, 2004). The reversal of rod formation indicates its potential as a therapeutic target in the early pathogenesis of AD, and the persistence of some rods has been observed when induced by ATP-depleting solution (Minamide *et al.*, 2000). These results argue for a 'critical window' for treatment/prevention of the progression of AD pathology.

Chapter 5

General Discussion and Future Directions

Discussion

Though actin dynamics has been studied for several decades, emerging technologies and perspectives continue to challenge our current understanding of it. In the past decade for instance, actin-nucleators were discovered and characterized (Mullins *et al.*, 1997), fluorescent-speckle microscopy emerged as a technique to study the dynamics of actin superstructures *in vivo* (Waterman-Storer *et al.*, 1998), and single-filament dynamics was imaged for the first time in real-time using total internal reflection microscopy (TIRFM) (Fujiwara *et al.*, 2002). All of these advances have contributed to a general model of actin dynamics that begins to unify, at least to some extent, results that range from *in vitro* to *in vivo* and from single filaments to complex superstructures.

Yet, as advances are made, some results demand a re-evaluation of the current paradigm at a fundamental level. For instance, using single-filament imaging and diffusional analysis, Fujiwara *et al.* described filament-dynamics during treadmilling that was 6-fold faster than expected (Fujiwara *et al.*, 2002), suggesting that actin dynamics might operate by different principles during steady-state (treadmilling) than during net-polymerization. If indeed true, this would have implications on cellular actin structures, which are generally considered to be undergoing treadmilling. The authors suggest, as one of several possible mechanisms, that the annealing and severing of short oligomers, of an average size of six subunits, might account for their observations (Fujiwara *et al.*, 2002). Therefore, using an exact stochastic simulation of actin dynamics, we tested

whether conventional rates of filament-annealing and –fragmentation might contribute to faster dynamics during treadmilling (Fass *et al.*, 2008). Our work suggested that conventional rates of annealing and fragmentation did not account for the effect, although a faster rate of fragmentation combined with a conventional rate of annealing could. We proposed that a faster rate of fragmentation might have resulted from the use of tetramethylrhodamine-labeled actin, which decreases the stability of actin filaments even when used at a low percentage to the total actin concentration (Kudryashov *et al.*, 2004).

Other advances have contributed to the paradigm by the demonstration of concepts that were merely hypothesized. Though theorized years before, the reconstitution of *Listeria monocytogenes* actin comet-tail motility demonstrated several key concepts of actin assembly (Loisel *et al.*, 1999; Cameron *et al.*, 1999): 1. actin superstructures are self-assembled by a ‘program’ of actin binding proteins, 2. dynamic superstructures can fuel their own motility by treadmilling, 3. superstructures act as a heterogeneous scaffold for actin binding proteins (transport function). The simplicity of the reconstitution assay, which involves mixing 4-5 actin binding proteins together with microspheres coated with an actin-nucleator, emphasizes the minimal requirements for generating an actin superstructure and its most fundamental characteristics.

Neuronal waves, growth cone-like structures that travel along the length of neurites, were hypothesized to contribute to neuritogenesis by transporting actin to growth cones (Ruthel and Banker, 1998), and the *Listeria* actin-comet-tail model already suggested a mechanism for how this could work. A treadmilling actin superstructure could inherently fuel its own motility as well as transport actin and actin binding proteins. Our results are entirely consistent with this conceptual model, and though not

investigated explicitly, indirect evidence suggests that many actin binding proteins, including cofilin and myosin II, are being delivered to growth cones by waves (Flynn *et al.*, 2009). For instance, upon wave arrival, growth cones retract, which depends on myosin II activity (Flynn *et al.*, 2009). Thus, waves are a unique transport mechanism in that waves inherently couple the act of delivery with the package itself.

Interactions between MAPs and cofilin-actin rods suggest that actin may be serving as a scaffold for more than just actin binding proteins. Indeed, the extent of disruption to both actin- and microtubule-binding proteins is likely underestimated, and other proteins may also localize to hyperphosphorylated-tau aggregates and/or cofilin-actin rods. If, indeed, tau hyperphosphorylation and rod formation are inter-dependent, this may offer a therapeutic equivalent to targeting ‘two birds with one stone’.

Future Directions

GSK-3 β is an important mediator of AD pathology (Takashima *et al.*, 2003; Serenó *et al.*, 2009), and we have provided evidence that its influence extends beyond tau phosphorylation. Though we have suggested that GSK-3 β may be involved in cofilin-actin rod formation through its ability to phosphorylate tau, its exact role is being investigated. Its potential ability to phosphorylate other MAPs and the co-localization of HMW MAP2s to rods suggests a pervasive disruption of MAP proteins, a hypothesis which is being investigated in conjunction by our collaborators, Ineka Whiteman and Dr. Claire Goldsbury.

We have also demonstrated that AMPA-induced rod formation is associated with the loss of trafficking of APP-YFP-containing vesicles. Effects, due to the stalling of

APP-YFP-containing vesicles, are being investigated by others in the lab. Specifically, though disruptions to APP-trafficking were hypothesized to increase amyloidogenic processing of APP (Terwel *et al.*, 2002; Stokin *et al.*, 2005), an increase in the secretion of total amyloid beta levels has not been detected (personal communication with I. Marsden). However, we have not ruled out the possibility that a shift towards amyloidogenic processing may be occurring without a change in the total amyloid beta levels. Defects of APP-YFP-containing vesicle trafficking may also indicate that vesicle trafficking in general or that kinesin-1-dependent trafficking are disrupted. APP has been reported to interact with kinesin-1 and be transported by the motor-protein; however, recent data has questioned whether this interaction actually occurs (Lazarov *et al.*, 2005). Nevertheless, vesicle trafficking defects have been observed by glutamate-treatment (Hiruma *et al.*, 2003), A β_{1-42} -treatment (Hiruma *et al.*, 2003; Stokin *et al.*, 2005), and the overexpression of tau (Goldbury *et al.*, 2006); therefore, trafficking defects represent an important and early pathological hallmark in AD.

Rods have also been implicated in synaptic dysfunction (Jang *et al.*, 2005). Whether rods affect pre- or post-synaptic function or whether their effect on synapses is localized or global would provide clues to its specific effects on learning and memory. Specifically, since A β_{1-42} -induced rods are preferentially formed in the dentate gyrus and hilar regions of organotypic hippocampal slices, rods might affect the trisynaptic pathway of the hippocampus, which involves the dentate gyrus, but not the monosynaptic pathway, which does not (Nakashiba *et al.*, 2008). Importantly, the trisynaptic and monosynaptic pathways are involved in different types of learning (Nakashiba *et al.*, 2008). Therefore, it would be of interest to determine other brain regions outside of the

hippocampus in which rods form, in particular, the entorhinal cortex. The entorhinal cortex, whose inputs to the hippocampus are important for both the tri- and mono-synaptic pathways (Nakashiba *et al.*, 2008), would be predicted to have a more profound effect on learning and memory, simply based on its involvement in both synaptic pathways. Preliminary evidence in organotypic slices in which portions of the entorhinal cortex were saved during the dissection suggest that rods can indeed form robustly in the subiculum and entorhinal cortex (data not shown). In addition, rods have been suggested to mediate synaptic loss without frank neuronal loss, especially in regions distal to the locus of rod formation (Minamide *et al.*, 2000).

In response to (S)-AMPA, extensive changes to the intracellular environment occur, including changes to the oxidation state of the neuron (Dong *et al.*, 2009), which is regulated by redox proteins such as glutathione (Vaughn and Deshmukh, 2008). These changes are likely to influence rod formation, for instance, cofilin-dimers have been identified after glutamate excitotoxicity (Bernstein *et al.*, in preparation). Also, in response to the generation of reactive oxygen species, actin can be S-nitrosylated, which influences its polymerization dynamics and intracellular distribution (Thom *et al.*, 2008). Thus, oxidative changes to cofilin and/or actin are likely to change their interaction-potential and polymerization dynamics necessary for rod formation.

Reference List

- Abe, H., Ohshima, S., and Obinata, T. 1989. A cofilin-like protein is involved in the regulation of actin assembly in developing skeletal muscle. *J Biochem.* 106:696-702.
- Abe, T., Kato, M., Miki, H., Takenawa, T., and Endo T. 2003. Small GTPase Tc10 and its homologue RhoT induce N-WASP-mediated long process formation and neurite outgrowth. *J Cell Sci.* 116:155-68.
- Aizawa, H., Wakatsuki, S., Ishii, A., Moriyama, K., Sasaki, Y., Ohashi, K., Sekine-Aizawa, Y., Sehera-Fujisawa, A., Mizuno, K., Goshima, Y., and Yahara I. 2001. Phosphorylation of cofilin by LIM-kinase is necessary for semaphorin 3A-induced growth cone collapse. *Nat Neurosci.* 4:367-373
- Alberts, P., Rudge, R., Irinopoulou, T., Danglot, L., Gauthier-Rouviere, C., and Galli T. 2006. Cdc42 and actin control polarized expression of TI-VAMP vesicles to neuronal growth cones and their fusion with the plasma membrane. *Mol Biol Cell.* 17:1194-1203.
- Andrianantoandro, E., Blanchoin, L., Sept, D., McCammon, J.A., and Pollard T.D. 2001. Kinetic mechanism of end-to-end annealing of actin filaments. *J Mol Biol.* 312:721-730.
- Andrianantoandro, E., and Pollard T.D. 2006. Mechanism of actin filament turnover by severing and nucleation at different concentrations of ADF/cofilin. *Mol Cell.* 24:13-23.
- Baas, P.W., and Buster, D.W. 2004. Slow axonal transport and the genesis of neuronal morphology. *J Neurobiol.* 58:3-17.
- Bamburg J.R. 1999. Proteins of the ADF/cofilin family: essential regulators of actin dynamics. *Annu Rev Cell Dev Biol.* 15:185-230.
- Bamburg, J.R., and Bloom G.S. 2009. Cytoskeletal pathologies of Alzheimer disease. *Cell Motil Cytoskeleton.* 66:635-649.
- Barr, F.A., and Gruneberg U. 2007. Cytokinesis: placing and making the final cut. *Cell.* 131:847-860.
- Bindschadler, M., Osborn, E.A., Dewey Jr., C.F., and McGrath J.L. 2004. A mechanistic model of the actin cycle. *Biophys J.* 86:2720-2739.
- Black, M.M., and Lasek R.J. 1979. Axonal transport of actin: slow component b is the principal source of actin for the axon. *Brain Res.* 171:401-13.

- Braak, H., and Braak E. 1995. Staging of Alzheimer's disease-related neurofibrillary changes. *Neurobiol Aging*. 16:271-278.
- Bradke, F., and Dotti C.G. 1997. Neuronal polarity: vectorial cytoplasmic flow precedes axon formation. *Neuron*. 19:1175-1186.
- Bradke, F., and Dotti C.G. 1999. The role of local actin instability in axon formation. *Science*. 283:1931-1934.
- Bretschneider, T., Anderson, K., Ecke, M., Müller-Taubenberger, A., Schroth-Diez, B., Ishikawa-Ankerhold, H.C., Gerisch G. 2009. The three-dimensional dynamics of actin waves, a model of cytoskeletal self-organization. *Biophys J*. 96:2888-2900.
- Bretteville, A., and Planel E. 2008. Tau aggregates: toxic, inert, or protective species? *J Alzheimer Dis*. 14:431-436.
- Bridgman, P.C., Dave, S., Asnes, C.F., Tullio, A.N., and Adelstein R.S. 2001. Myosin IIB is required for growth cone motility. *J Neurosci*. 21:6159-6169.
- Brown, A., Wang, L., and Jung P. 2005. Stochastic simulation of neurofilament transport in axons: the "stop-and-go" hypothesis. *Mol Biol Cell*. 16:4243-4255.
- Bray D. 2001. *Cell Movements: From Molecules to Motility*. Garland, Publishing, New York.
- Bryce, N.S., Schevzov, G., Ferguson, V., Percival, J.M., Lin, J.J., Matsumura, F., Bamburg, J.R., Jeffrey, P.L., Hardeman, E.C., Gunning, P., and Weinberger R.P. 2003. Specifications of actin filament function and molecular composition by tropomyosin isoforms. *Mol Biol Cell*. 14:1002-1016.
- Caceres, A., Payne, M.R., Binder, L.I., and Steward O. Immunocytochemical localization of actin and microtubule-associated protein MAP2 in dendritic spines. *Proc Natl Acad Sci USA*. 80:1783-1742.
- Cai, L., Makhov, A.M., and Bear J.E. 2007. F-actin binding is essential for coronin 1B function in vivo. *J Cell Sci*. 120:1179-1190.
- Cameron, L.A., Footer, M.J., van Oudenaarden, A., and Theriot J.A. 1999. Motility of ActA protein-coated microspheres driven by actin polymerization. *Proc Natl Acad Sci USA*. 96:4908-4913.
- Campbell, R.E., Tour, O., Palmer, A.E., Steinbach, P.A., Baird, G.S., Zacharias, D.A., and Tsien R.Y. 2002. A monomeric red fluorescent protein. *Proc Natl Acad Sci USA*. 99:7877-7882.

- Carlier M.F. 1990. Actin polymerization and ATP hydrolysis. *Adv Biophys.* 26:51-73.
- Carlier, M.F., Laurent, V., Santolini, J., Melki, R., Didry, D., Xia, G.X., Hong, Y., Chua, N.H., and Pantaloni D. 1997. Actin depolymerizing factor (ADF/cofilin) enhances the rate of filament turnover: implication in actin-based motility. *J Cell Biol.* 136:1307-1322.
- Carlier, M.F., and Pantaloni D. 1997. Control of actin dynamics in cell motility. *J Mol Biol.* 269:459-467.
- Carlier, M.F., Wiesner, S., Le Clainche, C., and Pantaloni D. 2003. Actin-based motility as a self-organized system: mechanism and reconstitution in vitro. *C R Biol.* 326:161-170.
- Carlsson A.E. 2005. The effect of branching on the critical concentration and average filament length of actin. *Biophys J.* 89:130-140.
- Carlsson A.E. 2006. Stimulation of actin polymerization by filament severing. *Biophys J.* 90:413-422.
- Chang, E.H., Savage, M.J., Flood, D.G., Thomas, J.M., Levy, R.B., Mahadomrongkul, V., Shirao, T., Aoki, C., and Huerta PT. 2006. AMPAR receptor downscaling at the onset of Alzheimer's disease pathology in double knockin mice. *Proc Natl Acad Sci USA.* 103:3410-3415.
- Churcher I. 2006. Tau therapeutic strategies for the treatment of Alzheimer's disease. *Curr Top Med Chem.* 6:579-595.
- Claessens, M.M., Bathe, M., Frey, E., and Bausch A.R. Actin-binding proteins sensitively mediate F-actin bundle stiffness. *Nature Mater.* 5:748-753.
- Cleveland D.W. 1982. Treadmilling of tubulin and actin. *Cell.* 28:689-691.
- Co, C., Wong, D.T., Gierke, S., Chang, V., and Taunton J. 2007. Mechanism of actin network attachment to moving membranes: barbed end capture by N-WASP WH2 domains. *Cell.* 128:901-913.
- Cooper, J.A., Buhle Jr., E.L., Walker, S.B., Tsong, T.Y., and Pollard T.D. 1983. Kinetic evidence for a monomer activation step in actin polymerization. *Biochemistry.* 22:2193-2202.
- Craig, A.M., and Banker G. 1994. Neuronal polarity. *Annu Rev Neurosci.* 17:267-310.
- Cudmore, S., Reckmann, I., and Way M. 1997. Viral manipulations of the actin cytoskeleton. *Trends Microbiol.* 5:142-148.

- da Silva, J.S., and Dotti, C.G. 2002. Breaking the neuronal sphere: regulation of the actin cytoskeleton in neurogenesis. *Nat Rev Neurosci.* 3:694-704.
- Dailey, M.E., Buchanan, J., Bergles, D.E., and Smith S.J. 1994. Mossy fiber growth and synaptogenesis in rat hippocampal slices in vitro. *J Neurosci.* 14:1060-1078.
- Davis, R.C., Maloney, M.T., Minamide, L.S., Flynn, K.C., Stonebraker, M.A., and Bamburg J.R. 2009. Mapping cofilin-actin rods in stressed hippocampal slices and the role of cdc42 in amyloid β -induced rods. *J Alz Dis.* [in press].
- Dehmelt, L., and Halpain S. 2005. The MAP2/Tau family of microtubule-associated proteins. *Genome Biol.* 6:204.
- de Hoop, M.J., Meyn, L., and Dotti C.G. 1998. Culturing Hippocampal Neurons and Astrocytes from Fetal Rodent Brain. *Academic Press, San Diego.* 154-163 pp.
- De La Cruz E.M. 2001. Actin-binding proteins: an overview. *Results Probl Cell Differ.* 32:123-134.
- De la Monte, S.M., Federoff, H.J., Ng, S.C., Grabczyk, E., and Fishman M.C. 1989. GAP-43 gene expression during development: persistence in a distinctive set of neurons in the mature central nervous system. *Brain Res Dev Brain Res.* 46:161-168.
- Delorme, V., Machacek, M., DerMardirossian, C., Anderson, K.L., Wittmann, T., Hanein, D., Waterman-Storer, C., Danuser, G., and Bokoch G.M. 2007. Cofilin activity downstream of Pak1 regulates cell protrusion efficiency by organizing lamellipodium and lamella actin networks. *Dev Cell.* 13:646-662.
- DesMarais, V., Ichetovkin, I., Condeelis, J., and Hitchcock-DeGregori S.E. 2002. Spatial regulation of actin dynamics: a tropomyosin-free, actin-rich compartment at the leading edge. *J Cell Biol.* 115:4649-4660.
- Dent, E.W., and Kalil, K. 2001. Axon branching requires interactions between dynamic microtubules and actin filaments. *J Neurosci.* 21:9757-9769.
- Dent, E.W., Kwiatkowski, A.V., Mebane, L.M., Philippar, U., Barzik, M., Rubinson, D.A., Gupton, S., Van Veen, J.E., Furman, C., Zhang, J., Alberts, A.S., Mori, S., and Gertler F.B. 2007. Filopodia are required for cortical neurite initiation. *Nat Cell Biol.* 9:1347-1359.
- Dong, X.X., Wang, Y., and Qin Z.H. 2009. Molecular mechanisms of excitotoxicity and their relevance to pathogenesis of neurodegenerative diseases. *Acta Pharmacol Sin.* 30:379-387.

- Dufort, P.A., and Lumsden C.J. 1993. High microfilament concentration results in barbed-end cap ADP caps. *Biophys J.* 65:1757-1766.
- Ehehalt, R., Keller, P., Haass, C., Thiele, C., and Simons K. 2003. Amyloidogenic processing of the Alzheimer beta-amyloid precursor protein depends on lipid rafts. *J Cell Biol.* 160:113:123.
- Einstein A. 1956. Investigations on the Theory of Brownian Movement. Dover Publications, Inc., New York.
- Engel, J., Fasold, H., Hulla, F.W., Waechter, F., and Wegner A. 1977. The polymerization reaction of muscle actin. *Mol Cell Biochem.* 18:3-13.
- Endo, M., Ohashi, K., Sasaki, Y., Goshima, Y., Niwa, R., Uemura, T., and Mizuno K. 2003. Control of growth cone motility and morphology by LIM kinase and Slingshot via phosphorylation and dephosphorylation of cofilin. *J Neurosci.* 23:2527-2537.
- Ermentrout, G.B., and Edelstein-Keshet L. 1998. Models for the length distributions of actin filaments: II. Polymerization and fragmentation by gelsolin actin together. *Bull Math Biol.* 60:477-503.
- Esch, T., Lemmon, V., Banker G. 1999. Local presentation of substrate molecules directs axon specification by cultured hippocampal neurons. *J Neurosci.* 19:6417-6426.
- Faix, J., and Grosse R. 2006. Staying in shape with formins. *Dev Cell.* 10:693-706.
- Fass, J., Pak, C., Bamburg, J., and Mogilner A. 2008. Stochastic simulation of actin dynamics reveals the role of annealing and fragmentation. *J Theor Biol.* 252:173-183.
- Faure, C., Corvol, J.C., Toutant, M., Valjent, E., Hvalby, O., Jensen, V., El Messari, S., Corsi, J.M., Kadaré, G., and Girault J.A. 2007. Calcineurin is essential for depolarization-induced nuclear translocation and tyrosine phosphorylation of PYK2 in neurons. *J Cell Sci.* 120:3034-3044.
- Federov, A.A., Lappalainen, P., Fedorov, E.V., Drubin, D.G., and Almo S.C. 1997. Structure determination of yeast cofilin. *Nat Struct Biol.* 4:366-369.
- Feng, G., Mellor, R.H., Bernstein, M., Keller-Peck, C., Nguyen, Q.T., Wallace, M., Nerbonne, J.M., Lichtman, J.W., and Sanes, J.R. 2000. Imaging neuronal subsets in transgenic mice expressing multiple spectral variants of GFP. *Neuron.* 28:41-51.

- Flynn, K.C., Pak, C.W., Shaw, A.E., Bradke, F., and Bamberg J.R. 2009. Growth cone-like waves transport actin and promote axonogenesis and neurite branching. *Dev Neurobiol.* [in press]
- Forss-Petter, S., Danielson, P.E., Catsicas, S., Battenberg, E., Price, J., Nerenberg, M., and Sutcliffe J.G.. 1990. Transgenic mice expressing beta-galactosidase in mature neurons under neuron-specific enolase promoter control. *Neuron.* 5:187-197.
- Frieden, C., and Goddette D.W. 1983. Polymerization of actin and actin-like systems: evaluation of the time course of polymerization in relation to the mechanism. *Biochemistry.* 22:5836-5843.
- Fujiwara, I., Takahashi, S., Tadakuma, H., Funatsu, T., and Ishiwata S. 2002. Microscopic analysis of polymerization dynamics with individual actin filaments. *Nat Cell Biol.* 4:666-673.
- Fulga, T.A., Elson-Schwab, I., Khurana, V., Steinhilb, M.L., Spires, T.L., Hyman, B.T., and Feany M.B. 2007. Abnormal bundling and accumulation of F-actin mediates tau-induced neuronal degeneration in vivo. *Nat Cell Biol.* 9:139-148.
- Gallo, G., and Letourneau, P.C. 2004. Regulation of growth cone actin filaments by guidance cues. *J Neurobiol.* 58:92-102.
- Gallo, G., Yee, H.F. Jr., and Letourneau, P.C. 2002. Actin turnover is required to prevent axon retraction driven by endogenous actomyosin contractility. *J Cell Biol.* 158:1219-1228.
- Galkin, V.E., Orlova, A., VanLoock, M.S., Shvetsov, A., Reisler, E., and Egelman E.H. 2003. ADF/cofilin use an intrinsic mode of F-actin instability to disrupt actin filaments. *J Cell Biol.* 163:1057-1066.
- Galvan, V., Gorostiza, O.F., Banwait, S., Ataie, M., Logvinova, A.V., Sitaraman, S., Carlson, E., Sagi, S.A., Chevallier, N., Jin, K., Greenberg, D.A., and Bredesen D.E. 2006. Reversal of Alzheimer's-like pathology and behavior in human APP transgenic mice by mutation of Asp664. *Proc Natl Acad Sci USA.* 103:7130-7135.
- Garvalov, B.K., Flynn, K.C., Neukirchen, D., Meyn, L., Teusch, N., Wu, X., Brakebusch, C., Bamberg, J.R., and Bradke F. 2007. Cdc42 regulates cofilin during the establishment of neuronal polarity. *J Neurosci.* 27:13117-13129.
- Gardel, M.L., Shin, J.H., MacKintosh, F.C., Mahadevan, L., Matsudaira, P., and Weitz D.A. 2004. Elastic behavior of cross-linked and bundled actin networks. *Science.* 304:1301-1305.
- Giannakopoulos, P., Hof, P.R., Michel, J.P., Guimon, J., and Bouras C. 1997. Cerebral

- cortex pathology in aging and Alzheimer's disease: a quantitative survey of large hospital-based geriatric and psychiatric cohorts. *Brain Res Brain Res Rev.* 25:217-245.
- Gibson, M.A., and Bruck J. 2000. Efficient exact stochastic simulation of chemical systems with many species and many channels. *J Phys Chem A.* 104:1876-1889.
- Gillespie, D.T. 1977. Exact Stochastic Simulation of Coupled Chemical-Reactions. *J Phys Chem.* 81:2340-2361.
- Girao, H., Geli, M.I., and Idrissi F.Z. 2008. Actin in the endocytic pathway: from yeast to mammals. *FEBS Lett.* 582:2112-2119.
- Goldsbury, C., Mocanu, M.M., Thies, E., Kaether, C., Haass, C., Keller, P., Biernat, J., Mandelkow, E., and Mandelkow E.M. 2006. Inhibition of APP trafficking by tau protein does not increase the generation of amyloid-beta peptides. *Traffic.* 7:873-888.
- Goldschmidt-Clermont, P.J., Furman, M.I., Wachsstock, D., Safer, D., Nachmias, V.T., and Pollard T.D. 1992. The control of actin nucleotide exchange by thymosin beta 4 and profiling. A potential regulatory mechanism for actin polymerization in cells. *Mol Biol Cell.* 3:1015-1024.
- Goley, E.D., and Welch M.D. 2006. The Arp2/3 complex: an actin nucleator comes of age. *Nature Rev Mol Cell Biol.* 7:713-726.
- Gomez-Di Cesare, C.M., Smith, K.L., Rice, F.L., and Swann J.W. 1997. Axonal remodeling during postnatal maturation of CA3 hippocampal pyramidal neurons. *J Comp Neurol.* 384:165-180.
- Gorbatyuk, V.Y., Nosworthy, N.J., Robson, S.A., Bains, N.P., Maciejewski, M.W., Dos Remedios, C.G., and King G.F. 2006. Mapping the phosphoinositide-binding site on chick cofilin explains how PIP2 regulates the cofilin-actin interaction. *Mol Cell.* 24:511-522.
- Gouin, E., Welch, M.D., and Cossart P. 2005. Actin-based motility of intracellular pathogens. *Curr Opin Microbiol.* 8:35-45.
- Gu, Z., Liu, W., and Yan Z. 2009. β -Amyloid impairs AMPA receptor trafficking and function by reducing Ca²⁺/calmodulin-dependent protein kinase II synaptic redistribution. *J Biol Chem.* 284:10639-10649.
- Gunning, P.W., Schevzov, G., Kee, A.J., and Hardeman E.C. 2005. Tropomyosin isoforms: diving rods for actin cytoskeleton function. *Trends Cell Biol.* 15:333-341.

- Gupton, S.L., Anderson, K.L., Kole, T.P., Fischer, R.S., Ponti, A., Hitchcock-DeGregori, S.E., Danuser, G., Fowler, V.M., Wirtz, D., Hanein, D., Waterman-Storer, C.M. 2005. Cell migration without a lamellipodium: translation of actin dynamics into cell movement mediated by tropomyosin. *J Cell Biol.* 168:619-631.
- Gurniak, C.B., Perlas, E., and Witke W. 2005. The actin depolymerizing factor n-cofilin is essential for neural tube morphogenesis and neural crest cell migration. *Dev Biol.* 278:231-241.
- Gurskaya, N.G., Verkhusha, V.V., Shcheglov, A.S., Staroverov, D.B., Chepurnykh, T.V., Fradkov, A.F., Lukyanov, S., and Lukyanov K.A. 2006. Engineering of a monomeric green-to-red photoactivatable fluorescent protein induced by blue light. *Nat Biotechnol.* 24: 461-465.
- Hannan, A.J., Blakemore, C., Katsnelson, A., Vitalis, T., Huber, K.M., Bear, M., Roder, J., Kim, D., Shin, H.S., and Kind P.C. 2001. PLC-beta1, activated via mGluRs, mediates activity-dependent differentiation in cerebral cortex. *Nat Neurosci.* 4:282-288.
- Heidemann, S.R., Reynolds, M., Ngo, K., and Lamoureux P. 2003. The culture of chick forebrain neurons. *Methods Cell Biol.* 71:51-65.
- Herman, M.A., and Jahr C.E. 2007. Extracellular glutamate concentration in hippocampal slice. *J Neurosci.* 27:9736-9741.
- Hertzog, M., van Heijenoort, C., Didry, D., Gaudier, M., Coutant, J., Gigant, B., Didelot, G., Pr at, T., Knossow, M., Guittet, E., and Carlier M.F. 2004. The beta-thymosin/WH2 domain; structural basis for the switch from inhibition to promotion of actin assembly. *Cell.* 117:611-623.
- Hill T.L. 1983. Length dependence of rate constants for end-to-end association and dissociation of equilibrium linear aggregates. *Biophys J.* 44:285-288.
- Hill, T.L., and Kirschner M.W. 1982. Subunit treadmilling of microtubules or actin in the presence of cellular barriers: possible conversion of chemical free energy into mechanical work. *Proc Natl Acad Sci USA.* 79:490-494.
- Ho, M.T., Pelkey, K.A., Pelletier, J.G., Hugarir, R.L., Lacaille, J.C., and McBain C.J. 2009. Burst firing induces postsynaptic LTD at developing mossy fiber-CA3 pyramid synapses. *J Physiol.*
- Hofmann W.A. 2009. Cell and molecular biology of nuclear actin. *Int Rev Cell Mol Biol.* 273:219-263.

- Homma, K., Niino, Y., Hotta, K., and Oka K. 2008. Ca(2+) influx through P2X receptors induces actin cytoskeleton reorganization by the formation of cofilin rods in neurites. *Mol Cell Neurosci.* 37:261-270.
- Horton, A.C., and Ehlers, M.D. 2003. Neuronal polarity and trafficking. *Neuron.* 40:277-295.
- Howard J. 2001. *Mechanics of Motor Proteins and the Cytoskeleton.* Sinauer Associates, Inc., Sunderland, MA.
- Hu, J., Matzavinos, A., and Othmer H.G. 2006. A Theoretical Approach to Actin Filament Dynamics. *Journal of Statistical Physics.* *online:DOI 10.1007/s10955-10006-19204-x.*
- Huang, T.Y., Minamide, L.S., Bamburg, J.R., and Bokoch G.M. 2008. Chronophin mediates an ATP-sensing mechanism for cofilin dephosphorylation and neuronal cofilin-actin rod formation. *Dev Cell.* 15:691-703.
- Hutchins, B.I., and Kalil K. 2008. Differential outgrowth of axons and their branches is regulated by localized calcium transients. *J Neurosci.* 28:143-153.
- Hyman, B.T., and Tanzi R.E. 1992. Amyloid, dementia and Alzheimer's disease. *Curr Opin Neurol Neurosurg.* 5:88-93.
- Ikeda, S., Cunningham, L.A., Boggess, D., Hawes, N., Hobson, C.D., Sundberg, J.P., Naggert, J.K., Smith, R.S., and Nishina P.M. 2003. Aberrant actin cytoskeleton leads to accelerated proliferation of corneal epithelial cells in mice deficient for destrin (actin depolymerizing factor). *Hum Mol Genet.* 12:1029-1037.
- Inagaki, N., Chihara, K., Arimura, N., Menager, C., Kawano, Y., Matsuo, N., Nishimura, T., Amano, M., and Kaibuchi K. 2001. CRMP-2 induces axons in cultured hippocampal neurons. *Nat Neurosci.* 4:781-782.
- Isambert, H., Venier, P., Maggs, A.C., Fattoum, A., Kassab, R., Pantaloni, D., and Carlier M.F. 1995. Flexibility of actin filaments derived from thermal fluctuations. Effect of bound nucleotide, phalloidin, and muscle regulatory proteins. *J Biol Chem.* 270:11437-11444.
- Iwasa, J.H., and Mullins R.D. 2007. Spatial and temporal relationships between actin-filament nucleation, capping, and disassembly. *Curr Biol.* 17:395-406.
- Jacobson, C., Schnapp, B., and Banker G.A. 2006. A change in the selective translocation of the Kinesin-1 motor domain marks the initial specification of the axon. *Neuron.* 49:797-804.
- Jang, D.H., Han, J.H., Lee, S.H., Lee, Y.S., Park, H., Lee, S.H., Kim, H., and Kaang B.K.

2005. Cofilin expression induces cofilin-actin rod formation and disrupts synaptic structure and function in *Aplysia* synapses. *Proc Natl Acad Sci USA*. 102:16072-16077.
- Jiang, H., Guo, W., Liang, X., and Rao Y. 2005. Both the establishment and the maintenance of neuronal polarity require active mechanisms: critical roles of GSK-3 β and its upstream regulators. *Cell*. 120:123-135.
- Jin, R., Singh, S.K., Gu, S., Furukawa, H., Sobolevsky, A.I., Zhou, J., Jin, Y., and Gouaux E. 2009. Crystal structure and association behaviour of the GluR2 amino-terminal domain. *EMBO J*. 28:1812-1823.
- Johnson, G.V., and Stoothoff W.H. 2004. Tau phosphorylation in neuronal cell function and dysfunction. *J Cell Sci*. 117: 5721-5729.
- Kamal, A., Almenar-Queralt, A., LeBlanc, J.F., Roberts, E.A., and Goldstein L.S. 2001. Kinesin-mediated axonal transport of a membrane compartment containing beta-secretase and presenilin-1 requires APP. *Nature*. 414:643-648.
- Kas, J., Strey, H., Tang, J.X., Finger, D., Ezzell, R., Sackmann, E., and Janmey P.A. 1996. F-actin, a model polymer for semiflexible chains in dilute, semidilute, and liquid crystalline solutions. *Biophys J*. 70:609-625.
- Ke, H., and Huai Q. 2003. Structures of calcineurin and its complexes with immunophilins-immunosuppressants. *Biochem Biophys Res Commun*. 311:1095-1102.
- Kerkhoff E. 2006. Cellular functions of the Spir actin-nucleation factors. *Trends Cell Biol*. 16:477-483.
- Kertesz, A. 2009. Clinical features and diagnosis of frontotemporal dementia. *Front Neurol Neurosci*. 24:140-148.
- Kim, Y., and Chang S. 2004. Modulation of actomyosin contractility by myosin light chain phosphorylation/dephosphorylation through Rho GTPases signaling specifies axon formation in neurons. *Biochem Biophys Res Commun*. 318:579-587.
- Kim, J.S., Huang, T.Y., and Bokoch G.M. 2009. Reactive oxygen species regulate a slingshot-cofilin activation pathway. *Mol Biol Cell*. 20:2650-2660.
- Knoll, B., Kretz, O., Fiedler, C., Alberti, S., Schutz, G., Frotscher, M., and Nordheim A. 2006. Serum response factor controls neuronal circuit assembly in the hippocampus. *Nat Neurosci*. 9:195-204.
- Köhler, M., Burnashev, N., Sakmann, B., and Seeburg P.H. 1993. Determinants of Ca²⁺

- permeability in both TM1 and TM2 of high affinity kainate receptor channels: diversity by RNA editing. *Neuron*. 10:491-500.
- Kovar, D.R., Harris, E.S., Mahaffy, R., Higgs, H.N., and Pollard T.D. 2006. Control of the assembly of ATP- and ADP-actin by formins and profilin. *Cell*. 124:423-435.
- Kuchibhotla, K.V., Goldman, S.T., Lattarulo, C.R., Wu, H.Y., Hyman, B.T., Bacskai, B.J. 2008. Abeta plaques lead to aberrant regulation of calcium homeostasis in vivo resulting in structural and functional disruption of neuronal networks. *Neuron*. 59:214-225.
- Kudryashov, D.S., Phillips, M., and Reisler E. 2004. Formation and destabilization of actin filaments with tetramethylrhodamine-modified actin. *Biophys J*. 87:1136-1145.
- Kuhn, J.R., and Pollard T.D. 2005. Real-time measurements of actin filament polymerization by total internal reflection fluorescence microscopy. *Biophys J*. 88:1387-1402.
- Kuhn, T.B., Meberg, P.J., Brown, M.D., Bernstein, B.W., Minamide, L.S., Jensen, J.R., Okada, K., Soda, E.A., and Bamberg J.R. 2000. Regulating actin dynamics in neuronal growth cones by ADF/cofilin and rho family GTPases. *J Neurobiol*. 44:126-144.
- Kunda, P., Paglini, G., Quiroga, S., Kosik, K., and Caceres A. 2001. Evidence for the involvement of Tiam1 in axon formation. *J Neurosci*. 21:2361-2372.
- Lanzetti L. 2007. Actin in membrane trafficking. *Curr Opin Cell Biol*. 19:453-458.
- Laurén, J., Gimbel, D.A., Nygaard, H.B., Gilbert, J.W., and Strittmatter S.M. Cellular prion protein mediates impairment of synaptic plasticity by amyloid-beta oligomers. *Nature*. 457:1128-1132.
- Lazarov, O., Morfini, G.A., Lee, E.B., Farah, M.H., Szodorai, A., DeBoer, S.R., Koliatsos, V.E., Kins, S., Lee, V.M., Wong, P.C., Price, D.L., Brady, S.T., and Sisodia S.S. 2005. Axonal transport, amyloid precursor protein, kinesin-1, and the processing apparatus: revisited. *J Neurosci*. 25:2386-2395.
- Le Clainche, C., and Carlier M.F. 2008. Regulation of actin assembly associated with protrusion and adhesion in cell migration. *Physiol Rev*. 88:489-513.
- Letourneau, P.C., Shattuck, T.A., and Ressler A.H. 1987. "Pull" and "push" in neurite elongation: observations on the effects of different concentrations of cytochalasin B and taxol. *Cell Motil Cytoskeleton*. 8:193-209.
- Li, S., Hong, S., Shepardson, N.E., Walsh, D.M., Shankar, G.M., and Selkoe D. 2009.

- Soluble oligomers of amyloid beta protein facilitate hippocampal long-term depression by disrupting neuronal glutamate uptake. *Neuron*. 62:788-801.
- Limozin, L., Barmann, M., and Sackmann E. 2003. On the organization of self-assembled actin networks in giant vesicles. *Eur Phys J E Soft Matter*. 10:319-330.
- Litersky, J.M., Johnson, G.V., Jakes, R., Goedert, M., Lee, M., and Seubert P. Tau protein is phosphorylated by cyclic AMP-dependent protein kinase and calcium/calmodulin-dependent protein kinase II within its microtubule-binding domains at Ser-262 and Ser-356. *Biochem J*. 316:655-660.
- Liu, S.J., and Zukin R.S. 2007. Ca^{2+} -permeable AMPA receptors in synaptic plasticity and neuronal death. *Trends Neurosci*. 30:126-134.
- Loisel, T.P., Boujemaa, R., Pantaloni, D., and Carlier M.F. 1999. Reconstitution of actin-based motility of *Listeria* and *Shigella* using pure proteins. *Nature*. 401:542-543.
- Loureiro, J.J., Rubinson, D.A., Bear, J.E., Baltus, G.A., Kwiatkowski, A.V., and Gertler F.B. 2002. Critical roles of phosphorylation and actin binding motifs, but not the central proline-rich region, for Ena/vasodilator-stimulated phosphoprotein (VASP) function during cell migration. *Mol Biol Cell*. 13:2533-2546.
- Luo, L., and O'Leary D.D. 2005. Axon retraction and degeneration in development and disease. *Annu Rev Neurosci*. 28:127-156.
- Ma, Y., Shakiryanova, D., Vardya, I., and Popov S.V. Quantitative analysis of microtubule transport in growing nerve processes. *Curr Biol*. 14:725-730.
- Mahajan, S.S., and Ziff E.B. 2007. Novel toxicity of the unedited GluR2 AMPA receptor subunit dependent on surface trafficking and increased Ca^{2+} -permeability. *Mol Cell Neurosci*. 35:470-481.
- Maloney, M.T., Minamide, L.S., Kinley, A.W., Boyle, J.A., and Bamberg J.R. 2005. Beta-secretase-cleaved amyloid precursor protein accumulates at actin inclusions induced in neurons by stress or amyloid beta: a feedforward mechanism for Alzheimer's disease. *J Neurosci*. 25:11313-11321.
- Marques, C., Turner, M., and Cates M. 1994. Relaxation Mechanisms in Worm-Like Micelles. *J Non-Crystalline Solids*. 172:1168-1172.
- Marsh, L., and Letourneau P.C. 1984. Growth of neurites without filopodial or lamellipodial activity in the presence of cytochalasin B. *J Cell Biol*. 99:2041-2047.

- Mattson, M.P., Kater S.B. 1988. Isolated hippocampal neurons in cryopreserved long-term cultures: development of neuroarchitecture and sensitivity to NMDA. *Int J Dev Neurosci.* 6:439-452.
- McQuarrie, I.G., and Jacob J.M. 1991. Conditioning nerve crush accelerates cytoskeletal protein transport in sprouts that form after a subsequent crush. *J Comp Neurol.* 305:139-147.
- Meberg, P.J., and Bamberg J.R. 2000. Increase in neurite outgrowth mediated by overexpression of actin depolymerizing factor. *J Neurosci.* 20:2459-2469.
- Meberg, P.J., Ono, S., Minamide, L.S., Takahashi, M., and Bamberg J.R. 1998. Actin depolymerizing factor and cofilin phosphorylation dynamics: response to signals that regulate neurite extension. *Cell Motil Cytoskeleton.* 39:172-190.
- Michaelis, E.K. 1998. Molecular biology of glutamate receptors in the central nervous system and their role in excitotoxicity, oxidative stress and aging. *Prog Neurobiol.* 54:369-415.
- Mills, R.G., Minamide, L.S., Yuan, A., Bamberg, J.R., and Bray J.J. 1996. Slow axonal transport of soluble actin with actin depolymerizing factor, cofilin, and profilin suggests actin moves in an unassembled form. *J Neurochem.* 67:1225-1234.
- Minamide, L.S., Striegl, A.M., Boyle, J.A., Meberg, P.J., and Bamberg J.R. 2000. Neurodegenerative stimuli induce persistent ADF/cofilin-actin rods that disrupt distal neurite function. *Nat Cell Biol.* 2:628-636.
- Minamide, L.S., Shaw, A.E., Sarmiere, P.D., Wiggan, O., Maloney, M.T., Bernstein, B.W., Sneider, J.M., Gonzalez, J.A., and Bamberg J.R. 2003. Production and use of replication-deficient adenovirus for transgene expression in neurons. *Methods Cell Biol.* 71:387-416.
- Misonou, H., Mohapatra, D.P., Park, E.W., Leung, V., Zhen, D., Misonou, K., Anderson, A.E., and Trimmer J.S. 2004. Regulation of ion channel localization and phosphorylation by neuronal activity. *Nat Neurosci.* 7:711-718.
- Monien B.H., Apostolova, L.G., and Bitan G. 2006. Early diagnostics and therapeutics for Alzheimer's disease – how early can we get there? *Expert Rev Neurother.* 6:1293-1306.
- Morales, M., and Fifkova E. 1989. Distribution of MAP2 in dendritic spines and its colocalization with actin. An immunogold electron-microscope study. *Cell Tissue Res.* 256:447-456.
- Mullins, R.D., Heuser, J.A., and Pollard T.D. 1998. The interaction of Arp2/3 complex

- with actin: nucleation, high affinity pointed end capping, and formation of branching networks of filaments. *Proc Natl Acad Sci USA*. 95:6181-6186.
- Nakashiba, T., Young, J.Z., McHugh, T.J., Buhl, D.L., and Tonegawa S. 2008. Transgenic inhibition of synaptic transmission reveals role of CA3 output in hippocampal learning. *Science*. 319:1260-1264.
- Neuhaus, J.M., Wanger, M., Keiser, T., and Wegner, A. 1983. Treadmilling of actin. *J Muscle Res Cell Motil*. 4:507-527.
- Neve, R.L., McPhie, D.L., and Chen Y. 2000. Alzheimer's disease: a dysfunction of the amyloid precursor protein(1). *Brain Res*. 886:54-66.
- Oddo, S., Billings, L., Kesslak, J.P., Cribbs, D.H., and LaFerla F.M. 2004. Abeta immunotherapy leads to clearance of early, but not late, hyperphosphorylated tau aggregates via the proteasome. *Neuron*. 43:321-332.
- O'Leary, D.D., and Terashima T. 1988. Cortical axons branch to multiple subcortical targets by interstitial axon budding: implications for target recognition and "waiting periods". *Neuron*. 1:901-910.
- Olson, M.F., and Sahai E. 2009. The actin cytoskeleton in cancer cell motility. *Clin Exp Metastasis*. 26:273-287.
- Oosawa, F., and Asakura S. 1975. Thermodynamics of the Polymerization of Protein. Academic Press, Inc., New York, NY.
- Orlova, A., Shvetsov, A., Galkin, V.E., Kudryashov, D.S., Rubenstein, P.A., Egelman, E.H., and Reisler E. 2004. Actin-destabilizing factors disrupt filaments by means of a time reversal of polymerization. *Proc Natl Acad Sci USA*. 101:17664-17668.
- Ozer, R.S., and Halpain S. 2000. Phosphorylation-dependent localization of microtubule-associated protein MAP2c to the actin cytoskeleton. *Mol Biol Cell*. 11:3573-3587.
- Paavilainen, V.O., Bertling, E., Falck, S., and Lappalainen P. 2004. Regulation of cytoskeletal dynamics by actin-monomer-binding proteins. *Trends Cell Biol*. 14:386-394.
- Pak, C.W., Flynn, K.C., and Bamberg J.R. 2008. Actin-binding proteins take the reins in growth cones. *Nat Rev Neurosci*. 9:136-147.
- Paunola, E., Mattila, P.K., and Lappalainen P. 2002. WH2 domain: a small, versatile adapter for actin monomers. *FEBS Lett*. 315: 92-97.
- Pepeu, G., and Giovannini M.G. 2009. Cholinesterase inhibitors and beyond. *Curr Alzheimer Res*. 6:86-96.

- Peskind, E.R. 1996. Neurobiology of Alzheimer's disease. *J Clin Psychiatry*. 57 Suppl 14:5-8.
- Pieper, U., and Wegner A. 1996. The end of a polymerizing actin filament contains numerous ATP-subunit segments that are disconnected by ADP-subunits resulting from ATP hydrolysis. *Biochemistry*. 35:4396-4402.
- Pigino, G., Morfini, G., Atagi, Y., Deshpande, A., Yu, C., Jungbauer, L., LaDu, M., Busciglio, J., and Brady S. 2009. Disruption of fast axonal transport is a pathogenic mechanism for intraneuronal amyloid beta. *Proc Natl Acad Sci USA*. 106:5907-5912.
- Pollard T.D. 1986a. Mechanism of actin filament self-assembly and regulation of the process by actin-binding proteins. *Biophys J*. 49:149-151.
- Pollard T.D. 1986b. Rate constants for the reactions of ATP- and ADP-actin with the ends of actin filaments. *J Cell Biol*. 103:2747-2754.
- Pollard, T.D., Blanchoin, L., and Mullins R.D. 2000. Molecular mechanisms controlling actin filament dynamics in nonmuscle cells. *Annu Rev Biophys Biomol Struct*. 29:545-576.
- Pollard, T.D., and Borisy G.G. 2003. Cellular motility driven by assembly and disassembly of actin filaments. *Cell*. 112:453-465.
- Pollard, T.D., and Mooseker M.S. 1981. Direct measurement of actin polymerization rate constants by electron microscopy of actin filaments nucleated by isolated microvillus cores. *J Cell Biol*. 88:654-659.
- Polesello, C., and Payre F. 2004. Small is beautiful: what flies tell us about ERM protein function in development. *Trends Cell Biol*. 14:294-302.
- Ponti, A., Machacek, M., Gupton, S.L., Waterman-Storer, C.M., and Danuser G. 2004. Two distinct actin networks drive the protrusion of migrating cells. *Science*. 305:1782-1786.
- Popov, S., and Poo, M.M. 1992. Diffusional transport of macromolecules in developing nerve processes. *J Neurosci*. 12:77-85.
- Pruyne, D., Evangelista, M., Yang, C., Bi, E., Zigmond, S., Bretscher, A., and Boone C. 2002. Role of formins in actin assembly: nucleation and barbed-end association. *Science*. 297:612-615.
- Quinlan, M.E., Heuser, J.E., Kerkhoff, E., and Mullins R.D. 2005. Drosophila Spire is an actin nucleation factor. *Nature*. 433:382-388.

- Roger, B., Al-Bassam, J., Dehmelt, L., Milligan, R.A., and Halpain S. MAP2c, but not tau, binds and bundles F-actin via its microtubule binding domain. *Curr Biol.* 14:363-371.
- Rosso, S., Bollati, F., Bisbal, M., Peretti, D., Sumi, T., Nakamura, T., Quiroga, S., Ferreira, A., and Caceres A. 2004. LIMK1 regulates Golgi dynamics, traffic of Golgi-derived vesicles, and process extension in primary cultured neurons. *Mol Biol Cell.* 15:3433-3449.
- Ruthel, G., and Banker G. 1998. Actin-dependent anterograde movement of growth-cone-like structures along growing hippocampal axons: a novel form of axonal transport? *Cell Motil Cytoskeleton.* 40:160-173.
- Ruthel, G., and Banker G. 1999. Role of moving growth cone-like “wave” structures in the outgrowth of cultured hippocampal axons and dendrites. *J Neurobiol.* 39:97-106.
- Ruthel, G., and Hollenbeck P.J. 2000. Growth cones are not required for initial establishment of polarity or differential axon branch growth in cultured hippocampal neurons. *J Neurosci.* 20:2266-2274.
- Sakurada, K., Masu, M., and Nakanishi S. 1993. Alteration of Ca²⁺ permeability and sensitivity to Mg²⁺ and channel blockers by a single amino acid substitution in the N-methyl-D-aspartate receptor. *J Biol Chem.* 268:410-415.
- Sato, M., Schwarz, W.H., and Pollard T.D. 1987. Dependence of the mechanical properties of actin/ α -actinin gels on deformation rate. *Nature.* 325:828-830.
- Schevzov, G., Gunning, P., Jeffrey, P.L., Temm-Grove, C., Helfman, D.M., Lin, J.J., and Weinberger R.P. 1997. Tropomyosin localization reveals distinct populations of microfilaments in neurites and growth cones. *Mol Cell Neurosci.* 8:439-454.
- Schwamborn, J.C., Muller, M., Becker, A.H., Puschel A.W. 2007. Ubiquitination of the GTPase Rap1B by the ubiquitin ligase Smurf2 is required for the establishment of neuronal polarity. *EMBO J.* 26:1410-1422.
- Schwamborn, J.C., and Puschel A.W. 2004. The sequential activity of the GTPases Rap1B and Cdc42 determines neuronal polarity. *Nat Neurosci.* 7:923-929.
- Sept, D., and McCammon J.A. 2001. Thermodynamics and kinetics of actin filament nucleation. *Biophys J.* 81:667-674.
- Sept, D., Xu, J., Pollard, T.D., and McCammon J.A. 1999. Annealing accounts for the length of actin filaments formed by spontaneous polymerization. *Biophys J.* 77:2911-2919.

- Seubert, P., Mawal-Dewan, M., Barbour, R., Jakes, R., Goedert, M., Johnson, G.V., Litsky, J.M., Schenk, D., Lieberburg, I., Trojanowski, J.Q., et al. 1995. Detection of phosphorylated Ser262 in fetal tau, adult tau, and paired helical filament tau. *J Biol Chem.* 270:18917-18922.
- Shankar, G.M., Li, S., Mehta, T.H., Garcia-Munoz, A., Shepardson, N.E., Smith, I., Brett, F.M., Farrell, M.A., Rowan, M.J., Lemere, C.A., Regan, C.M., Walsh, D.M., Sabatini, B.L., and Selkoe D.J. 2008. *Nat Med.* 14:837-842.
- Shi, S.H., Jan, L.Y., and Jan Y.N. 2003. Hippocampal neuronal polarity specified by spatially localized mPar3/mPar6 and PI 3-kinase activity. *Cell.* 112:63-75.
- Silacci, P., Mazzolai, L., Gauci, C., Stergiopoulos, N., Yin, H.L., and Hayoz D. 2004. Gelsolin superfamily proteins: key regulators of cellular functions. *Cell Mol Life Sci.* 61:2614-2623.
- Song, D.K., Malmstrom, T., Kater, S.B., and Mykles D.L. Calpain inhibitors block Ca(2+)-induced suppression of neurite outgrowth in isolated hippocampal pyramidal neurons. *J Neurosci Res.* 39:474-481.
- Southwick, F.S., and DiNubile M.J. 1986. Rabbit alveolar macrophages contain a Ca²⁺-sensitive, 41,000-dalton protein which reversibly blocks the 'barbed' ends of actin filaments but does not sever them. *J Biol Chem.* 261:14191-14195.
- Strasser, G.A., Rahim, N.A., VanderWaal, K.E., Gertler, F.B., and Lanier L.M. 2004. Arp2/3 is a negative regulator of growth cone translocation. *Neuron.* 43:81-94.
- Stokin, G.B., Lillo, C., Falzone, T.L., Bruschi, R.G., Rockenstein, E., Mount, S.L., Raman, R., Davies, P., Masliah, E., Williams, D.S., and Goldstein L.S. 2005. Axonopathy and transport deficits early in the pathogenesis of Alzheimer's disease. *Science.* 307:1282-1288.
- Stukalin, E.B., and Kolomeisky A.B. 2006. ATP hydrolysis stimulate large length fluctuations in single actin filaments. *Biophys J.* 90:2673-2685.
- Takata, K., Kitamura, Y., Nakata, Y., Matsuoka, Y., Tomimoto, H., Taniguchi, T., and Shimohama S. Involvement of WAVE accumulation in Abeta/APP pathology-dependent tangle modification in Alzheimer's disease. *Am J Pathol.* 175:17-24.
- Tamai, M., Matsumoto, K., Omura, S., Koyama, I., Ozawa, Y., and Hanada K. 1986. In vitro and in vivo inhibition of cysteine proteinases by EST, a new analog of E-64. *J Pharmacobiodyn.* 9:672-677.
- Takenawa, T., and Suetsugu S. 2007. The WASP-WAVE protein network: connecting the membrane to the cytoskeleton. *Nature Rev Mol Cell Biol.* 8:37-48.

- Tang, F., and Kalil K. 2005. Netrin-1 induces axon branching in developing cortical neurons by frequency-dependent calcium signaling pathways. *J Neurosci.* 25:6702-6715.
- Terwel, D., Dewachter, I., Van Leuven F. 2002. Axonal transport, tau protein, and neurodegeneration in Alzheimer's disease. *Neuromolecular Med.* 2:151-165.
- Theriot J.A. 1995. The cell biology of infection by intracellular bacterial pathogens. *Annu Rev Cell Dev Biol.* 11:213-239.
- Thinakaran, G., and Koo E.H. 2008. Amyloid precursor protein trafficking, processing, and function. *J Biol Chem.* 283:29615-29619.
- Thom, S.R., Bhopale, V.M., Mancini, D.J., and Milovanova T.N. 2008. Actin S-nitrosylation inhibits neutrophil beta2 integrin function. *J Biol Chem.* 283:10822-10834.
- Tobacman, L.S., and Korn E.D. 1983. The kinetics of actin nucleation and polymerization. *J Biol Chem.* 258:3207-3214.
- Toriyama, M., Shimada, T., Kim, K.B., Mitsuba, M., Nomura, E., Katsuta, K., Sakumura, Y., Roepstorff, P., and Inagaki N. 2006. Shootin1: A protein involved in the organization of an asymmetric signal for neuronal polarization. *J Cell Biol.* 175:147-157.
- Tursun, B., Schluter, A., Peters, M.A., Viehweger, B., Ostendorff, H.P., Soosairajah, J., Drung, A., Bossenz, M., Johnsen, S.A., Schweizer, M., Bernard, O., and Bach I. 2005. The ubiquitin ligase Rnf6 regulates local LIM kinase 1 levels in axonal growth cones. *Genes Dev.* 19:2307-2319.
- VanDongen, P., and Ernst M. 1984. Kinetics of Reversible Polymerization. *J Stat Phys.* 37:301-324.
- van Oudenaarden, A., and Theriot J.A. 1999. Cooperative symmetry-breaking by actin polymerization in a model for cell motility. *Nat Cell Biol.* 1:493-499.
- Vaughn, A.E., and Deshmukh M. 2008. Glucose metabolism inhibits apoptosis in neurons and cancer cells by redox inactivation of cytochrome c. *Nat Cell Biol.* 10:1477-1483.
- Vavylonis, D., Yang, Q., and O'Shaughnessy B. 2005. Actin polymerization kinetics, cap structure, and fluctuations. *Proc Natl Acad Sci USA.* 102:8543-8548.
- Wachsstock, D.H., Schwarz, W.H., and Pollard T.D. 1994. Cross-linker dynamics determine the mechanical properties of actin gels. *Biophys J.* 66:801-809.

- Wang, L., and Brown A. 2001. Rapid intermittent movement of axonal neurofilaments observed by fluorescence photobleaching. *Mol Biol Cell*. 12:3257-3267.
- Wang, L., and Brown A. 2002. Rapid movement of microtubules in axons. *Curr Biol*. 12:1496-1501.
- Wang, Y., Shibasaki, F., and Mizuno K. 2005. Calcium signal-induced cofilin dephosphorylation is mediated by Slingshot via calcineurin. *J Biol Chem*. 280:12683-12689.
- Waterman-Storer, C.M., Desai, A., Bulinski, J.C., and Salmon E.D. 1998. Fluorescent speckle microscopy, a method to visualize the dynamics of protein assemblies in living cells. *Curr Biol*. 8:1227-1230.
- Wegner A. 1982. Treadmilling of actin at physiological salt concentrations. An analysis of the critical concentrations of actin filaments. *J Mol Biol*. 161:607-615.
- Wegner, A., and Savko P. 1982. Fragmentation of actin filaments. *Biochemistry*. 21:1909-1913.
- Wen, Z., Han, L., Bamberg, J.R., Shim, S., Ming, G.L., and Zheng J.Q. 2007. BMP gradients steer nerve growth cones by a balancing act of LIM kinase and Slingshot phosphatase on ADF/cofilin. *J Cell Biol*. 178:107-119.
- Whiteman, I.T., Gervasio, O.L., Cullen, K.M., Guillemin, G.J., Jeong, E.V., Witting, P.K., Antao, S.T., Minamide, L.S., Bamberg, J.R., and Goldsbury C. 2009. Activated ADF/cofilin sequesters phosphorylated microtubule-associated-protein during assembly of Alzheimer-like neuritic cytoskeletal striations. *J Neurosci*. [in press]
- Williamson, J., Goldman, J., and Marder K.S. 2009. Genetic aspects of Alzheimer disease. *Neurologist*. 15:80-86.
- Witte, H., and Bradke F. 2008. The role of the cytoskeleton during neuronal polarization. *Curr Opin Neurobiol*. 18:479-487.
- Wollmuth, L.P., and Sakmann B. 1998. Different mechanisms of Ca²⁺ transport in NMDA and Ca²⁺-permeable AMPA glutamate receptor channels. *J Gen Physiol*. 112:623-636.
- Wujek, J.R., and Lasek R.J. 1983. Correlation of axonal regeneration and slow component B in two branches of a single axon. *J Neurosci*. 3:243-251.
- Yao P.J. 2004. Synaptic frailty and clathrin-mediated synaptic vesicle trafficking in Alzheimer's disease. *Trends Neurosci*. 27:24-29.

Yuen, E.Y., Gu, Z., and Yan Z. 2007. Calpain regulation of AMPAR receptor channels in cortical pyramidal neurons. *J Physiol.* 580:241-254.

Zuchero, J.B., Coutts, A.S., Quinlan, M.E., Thangue, N.B., and Mullins R.D. 2009. p53-cofactor JMY is a multifunctional actin nucleation factor. *Nat Cell Biol.* 11:451-459.